Prepared for submission to JHEP

Precision Higgs Physics at the CEPC

F. Irst,[a,b,1] **Jin Wang**[c] **T. Hird**[a,2] **and Fourth**[a,2]

[a] *One University, some-street, Country*
[b] *Another University, different-address, Country*
[c] *A School for Advanced Studies, some-location, Country*

E-mail: first@one.univ, second@asas.edu, third@one.univ, fourth@one.univ

Abstract: Version 0.4, Date: June 8, 2018
The discovery of a Higgs boson with its mass around 125 GeV by the ATLAS and CMS Collaborations has provided the first insight into the scalar sector of the Standard Model and beyond. The particle will be the subject of extensive studies of the ongoing LHC program. A lepton collider Higgs factory has been proposed as a logical next step beyond the LHC to measure the properties and study potential new physics associated with the Higgs boson. The Circular Electron Positron Collider (CEPC) is one of such proposed Higgs factories. The CEPC is an e^+e^- circular collider with a center-of-mass energy of $\sim 240-250$ GeV in a tunnel of approximately 100 km in circumference proposed by China. It will be followed by a Super Proton-Proton Collider (SPPC) in the same tunnel with an energy $70-100$ TeV. In this paper, we present the first estimates on the precision of Higgs property measurements achievable at the CEPC.

---

[1] Corresponding author.
[2] Also at Some University.

Contents

---

1 Introduction

The historic discovery of a Higgs boson in 2012 by the ATLAS and CMS collaborations [1, 2] at the Large Hadron Collider (LHC) has opened a new era in particle physics. Subsequent measurements of the properties of the new particle have indicated compatibility with the Standard Model (SM) Higgs boson [3–7] [need updates]. While the SM has been remarkably successful in describing experimental phenomena, it is important to recognize that the SM is not a complete theory. In particular, the SM does not *predict* the parameters in the Higgs potential, such as the Higgs mass. The vast difference between the Planck scale and the weak scale remains a major mystery. There is not a complete understanding of the nature of electroweak phase transition. The discovery of a spin zero Higgs boson, the first elementary particle of its kind, only sharpens these questions. It is clear that any attempt of addressing these questions will involve new physics beyond the SM. Therefore, the Higgs boson discovery marks the beginning of a new era of theoretical and experimental explorations.

A physics program of precision measurement of Higgs properties will be a critical component of any roadmap for high energy physics in the coming decades. Potential new physics beyond the SM could lead to observable deviations in the Higgs boson couplings from the SM expectations. Typically, such deviations can be parametrized as

$$\delta = c \frac{v^2}{M_{\rm NP}^2}, \tag{1.1}$$

where v and $M_{\rm NP}$ are the vacuum expectation value of the Higgs field and the typical mass scale of new physics, respectively. The size of the proportionality constant c depends on model, but it should not be much larger than $\mathcal{O}(1)$. The current and upcoming LHC runs will measure the Higgs couplings to about 5% Ref [8]. At the same time, LHC will directly search for new physics from a few hundreds of GeV to at least a TeV. Eq. (1.1) implies that probing new physics significantly beyond the LHC reach would require the measurement of the Higgs boson couplings at least at percent level accuracy. To achieve such sub-percent level of precision will need new facilities, a lepton collider operating as a Higgs factory is a natural next step.

The Circular Electron-Positron Collider (CEPC), proposed by the Chinese particle physics community, is one of such possible facilities. The CEPC will be housed in a tunnel with a circumference about 100 km and will operate at a center-of-mass energy of $\sqrt{s} \sim 240$ GeV, which maximizes the Higgs boson production cross section through the $e^+e^- \to ZH$ process. At the CEPC, in contrast to the LHC, Higgs boson candidate events can be identified through a technique known as the recoil mass method without tagging its decays. Therefore, Higgs boson production can be disentangled from its decay in a model independent way. Moreover, the cleaner environment at a lepton collider allows much better exclusive measurement of Higgs boson decay channels. All of these give the CEPC impressive reach in probing Higgs boson properties. For example, with an integrated luminosity of 5 ab^{-1}, over one million Higgs bosons will be produced. With this sample, the CEPC will be able to measure the Higgs boson coupling to the Z boson with an accuracy of 0.25%

[update], more than a factor of 10 better than the High Luminosity (HL)-LHC. Such a precise measurement gives the CEPC unprecedented reach into interesting new physics scenarios which are very difficult to probe at the LHC. The CEPC also has strong capability in detecting Higgs boson invisible decay. For example, with 5 ab^{-1}, it can improve the accuracy of the measurement of invisible decay branching ratio to 0.14% [update here, do we really mean invisible decay?]. In addition, it is expected to have good sensitivities to exotic decay channels which are swamped by backgrounds at the LHC. It is also important to stress that an e^+e^- Higgs factory can perform *model independent* measurement of the Higgs boson width. This unique feature in turn allows for model independent determination of the Higgs boson couplings.

This paper documents the first studies of a precision Higgs boson physics program at the CEPC. It is organized as follows: Section 2 briefly summarizes the collider and detector performance parameters assumed for the studies. Section 5 describes individual Higgs boson measurements including the methodology and results from simulation studies. Section 6 discusses the combination of individual measurements and the extraction of Higgs boson coupling parameters. Finally the implications of these measurements are discussed in Section. 9.

2 The CEPC Conceptual Detector

2.1 The CEPC operation scenarios

The CEPC is designed to operate as a Higgs factory at $\sqrt{s} = 240$ GeV and as a Z factory at $\sqrt{s} = 91.2$ GeV. It can also perform WW threshold scans around $\sqrt{s} = 161$ GeV. Table 1 shows potential CEPC operation scenarios and the expected numbers of H, W and Z bosons produced in these scenarios.

Operation mode	Z factory	WW threshold	Higgs factory
$\sqrt{s}$ (GeV)	91.2	161	240
Instantaneous luminosity ($10^{34}\,\mathrm{cm}^{-2}\mathrm{s}^{-1}$)	16–32	11	3
Run time (year)	1–2	1	10
Integrated luminosity (ab^{-1})	??	??	5
Higgs boson yield	-	-	10^6
W boson yield	-	10^8	10^8
Z boson yield	10^{10-11}	10^9	10^9

Table 1. CEPC operation scenarios and the yields Higgs, W and Z bosons. The integrated luminosity and the yields assume two interaction points.

The CEPC operation as a Higgs factory will last for a decade and produce a total of 1 million Higgs bosons with two interaction points. Meanwhile, approximately 100 million W bosons and 1 billion Z bosons will also be produced in this operation. These W and Z bosons will allow for in-situ detector characterization as well as for precise measurements of electroweak parameters. Benefiting from the clean e^+e^- collision environment and the large number of Higgs bosons, the CEPC is expected to improve the precision of most of the Higgs boson property measurements by a factor of ten over those achievable at the high luminosity LHC.

Running at the WW threshold around $\sqrt{s} = 161$ GeV, 10^9 W bosons (differ from the table) will be produced in one year. Similarly as a Z factory at $\sqrt{s} = 91.2$ GeV, CEPC will produce 10^{10-11} Z bosons per year. These large samples will enable high precision measurements of the electroweak observables such as A^b_{FB}, R_b, the Z boson line-shape parameters, the mass and width of the W boson. An order of magnitude or more improvement in the precision of these observables are foreseen.

2.2 Conceptual detector design

The primary physics objective of the CEPC is the precise determination of the Higgs boson properties. Therefore CEPC detectors must be able to reconstruct and identify all key physics objects that the Higgs bosons are produced with or decay into with high efficiency, purity and accuracy. These objects include charged leptons, photons, jets, missing energy and missing momentum. Moreover, the flavor tagging of jets, such as those from b, c and light quarks or gluons, are crucial for identifying the hadronic decays of the Higgs bosons. The detector requirements for the electroweak and heavy flavor physics are similar. One notable additional requirement is the identification of charged particles such as $\pi^\pm$ and $K^\pm$ for the heavy flavor physics program.

Using the International Large Detector (ILD) [9, 10] as a reference, a Particle Flow oriented conceptual detector, CEPC-v1, has been developed for the CEPC, see Fig 1. A detailed description of the CEPC-v1 detector can be found in Ref. [11]. Originally developed for LEP experiments [12, 13], Particle Flow is a well validated principle for event reconstructions [14–17] and is based on the premise of reconstructing all visible final state particles in the most sensitive subdetector system. Specifically, a particle-flow algorithm reconstructs charged particles in the tracking system, measures photons in the electromagnetic calorimeter and neutral hadrons in both electromagnetic and hadronic calorimeters. Physics objects are then identified or reconstructed from the unique list of final state particles. Particle Flow reconstruction provides a coherent interpretation of an entire physics event and, therefore, is particularly well suited for the identification of composite physics objects such as the τ leptons and jets.

Particle Flow algorithm requires good spatial separations of calorimeter showers induced by different final state particles for their reconstruction. It is imperative to minimize the amount of material before the calorimeter to reduce the uncertainty induced by the nuclear interactions and Bremsstrahlung radiations. Therefore, a high granularity calorimeter system and low material tracking system are implemented in the CEPC-v1 detector concept. The tracking system consists of silicon vertexing and tracking detectors as well as a Time Projection Chamber (TPC). The calorimetry system is based on the sampling technology with absorber/active-medium combination of W/Si for the electromagnetic calorimeter (ECAL) and Fe/Scintillator for the hadronic calorimeter (HCAL). The calorimeters are segmented at about 1 channel/cm^3, three orders of magnitude finer than those of the LHC

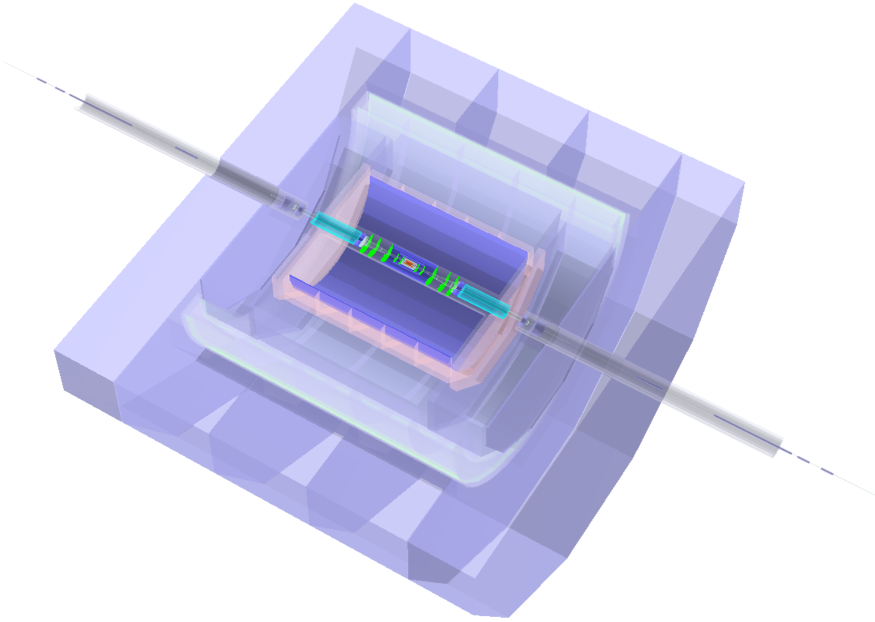

Figure 1. Conceptual CEPC detector, CEPC-v1, implemented in MOKKA [18] and GEANT 4 [19]. It is comprised of a silicon vertexing and tracking system of both pixel and strips geometry, a TPC tracker, a high granularity calorimeter system, a solenoid of 3.5 Tesla magnetic field, and a muon detector embedded in a magnetic field return yoke.

detectors. Both the tracking and the calorimeter system are housed inside a solenoid of 3.5 Tesla magnetic field. The CEPC-v1 detector has a sophisticated machine-detector interface with an 1.5 meter L* (the distance between the interaction point and the final focusing quadrupole magnet) to accommodate the high design luminosity. Table 2 shows the geometric parameters and the benchmark subdetector performances of the CEPC-v1 detector. A quartic view of the detector is shown in Fig. 2.

Silicon detectors	
Time Projection Chamber	Radii: 300–1808 mm; length: 4700 mm; 220 radial readouts
Electromagnetic calorimeter	W/Si, XXX_0, 30 active layers
Hadron calorimeter	Fe/Scintillator, $XX\lambda$, 48 active layers
Detector acceptance	TPC (97%), ECAL, HCAL (99.5%)
Track momentum resolution	$\Delta(1/p_T) \sim 2 \times 10^{-5}$ (1/GeV)
Impact parameter resolution	5 μm the usual $a \oplus b$ parametrization?
ECAL energy resolution	$\Delta E/E \sim 16\%/\sqrt{E\,(\mathrm{GeV})} \oplus 1\%$
HCAL energy resolution	$\Delta E/E \sim 60\%/\sqrt{E\,(\mathrm{GeV})} \oplus 1\%$

Table 2. Basic parameters and performances of the CEPC-v1 detector. The radiation and interaction lengths are measured for normal incidences.

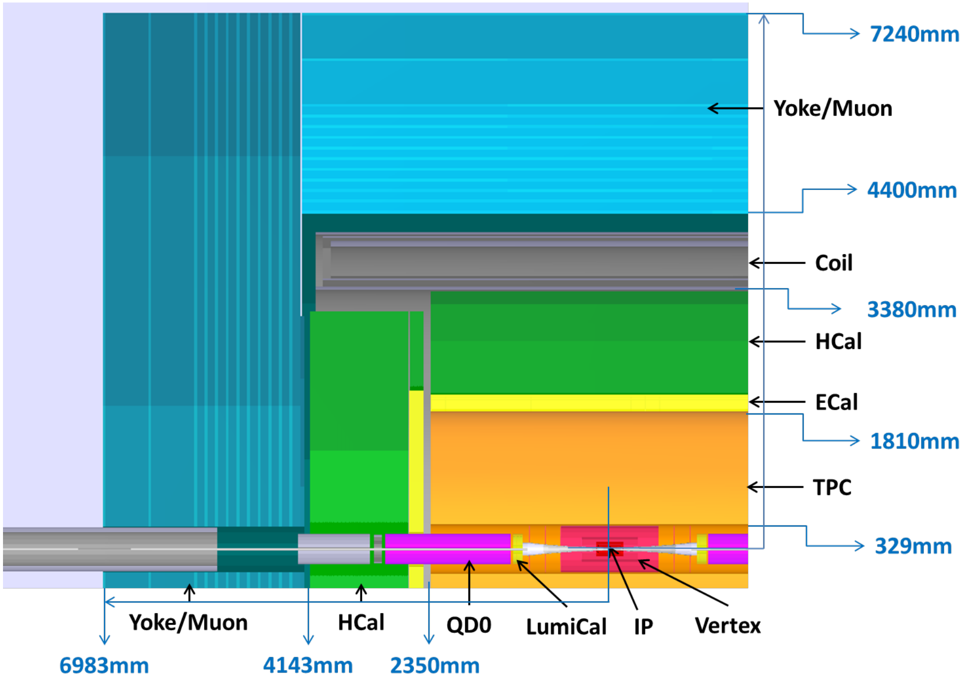

Figure 2. A schematic quartic view of the CEPC-v1 detector.

2.3 Object reconstruction and identification

A dedicated Particle Flow reconstruction toolkit, Arbor [15], has been developed for the CEPC-v1 detector. Inspired by the tree structure of particle showers, Arbor attempts to reconstruct every visible final state particle. Figure 3 illustrates a simulated $e^+e^- \to ZH \to q\bar{q}\,b\bar{b}$ event as reconstructed by the Arbor algorithm. The algorithm's performance for leptons, photons and jets are briefly summarized here. More details can be found in Ref. [20].

2.3.1 Leptons and Photons

Leptons (ℓ)[1] are fundamental for the measurements of the Higgs boson properties at the CEPC. About 7% of the Higgs bosons are produced in association with a pair of leptons through the $e^+e^- \to ZH \to \ell\ell\,H$ process. These events allow for the identifications of the Higgs bosons using the recoil mass information and therefore enable the measurement of the ZH production cross section and the Higgs boson mass. Moreover, a significant fraction of the Higgs bosons decay into final states with leptons indirectly through the W or Z bosons as well as the τ leptons. These leptons serve as signatures for identifying different Higgs boson decay modes.

A lepton identification algorithm, LICH [21], has been developed and integrated into Arbor. Efficiencies close to 99.9% for identifying electrons and muons with energies above 2 GeV have been achieved while limiting the mis-identification rates from hadrons to be less

[1] Unless otherwise noted, leptons refer to electrons and muons thereafter, i.e. $\ell = e,\ \mu$.

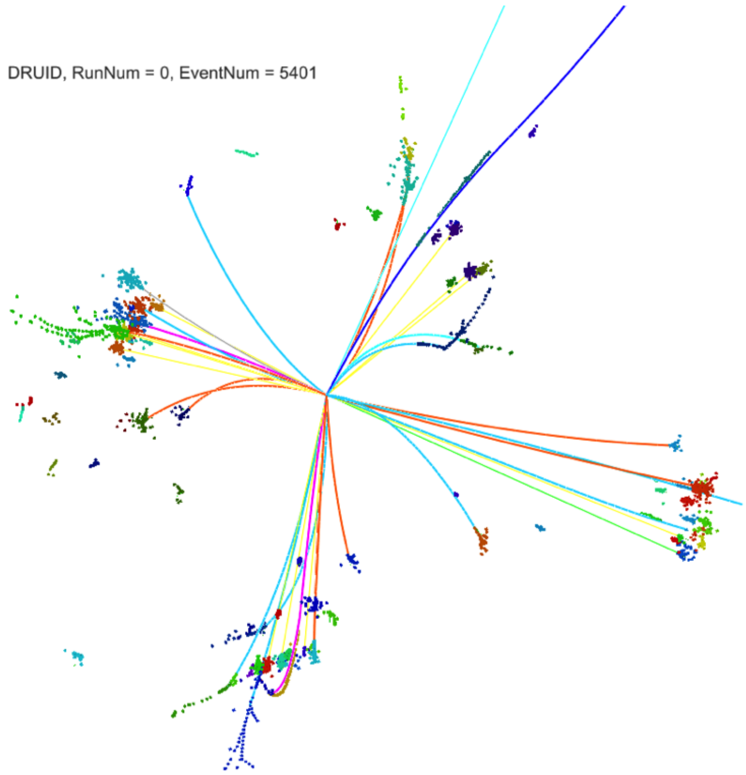

Figure 3. A simulated $e^+e^- \rightarrow ZH \rightarrow q\bar{q}\ b\bar{b}$ event reconstructed with the ARBOR algorithm. Different types of reconstructed final state particles are represented in different colors.

than 1%. The CEPC-v1 tracking system provides an excellent momentum resolution that is about ten times better than those of the LEP and LHC detectors. The good resolution is illustrated in the narrow invariant mass distribution of muon pairs from the $H \rightarrow \mu^+\mu^-$ decays as shown in Fig. 4 (a). A relative mass resolution of 0.16% for $H \rightarrow \mu^+\mu^-$ is expected.

Photons are essential for the studies of $H \rightarrow \gamma\gamma$ and $H \rightarrow Z\gamma$ decays. They are also important for the reconstructions and measurements of τ leptons and jets. The $H \rightarrow \gamma\gamma$ decay is an ideal process to characterize the photon performance of the CEPC-v1. Figure 4 (b) shows the invariant mass distribution of photon pairs from the $H \rightarrow \gamma\gamma$ decays. The distribution is well described by two Gaussians with the core Gaussian having a width of 2.4 GeV, or equivalently, a relative mass resolution of 1.9%.

2.3.2 Jets

About 70% of the Higgs bosons decay directly into jets ($b\bar{b}, c\bar{c}, gg$) and an additional 22% decay indirectly into final states with jets through the $H \rightarrow WW^*, ZZ^*$ cascades. Therefore, efficient jet reconstruction and precise measurements of their momenta are pre-requisite for a precision Higgs physics program. In ARBOR, jets are reconstructed using the Durham algorithm [22]. As a demonstration of the CEPC-v1 jet performance, Fig. 5 shows the

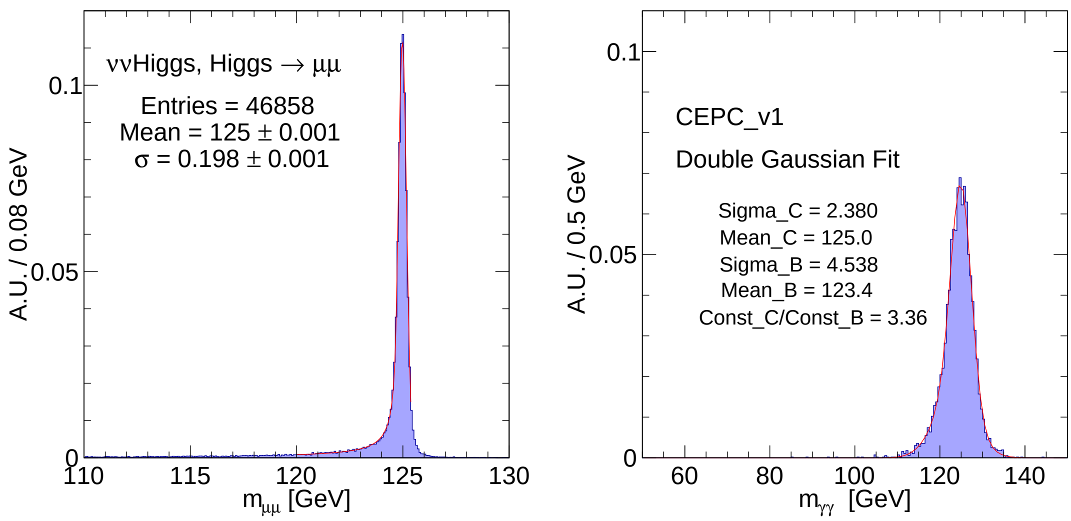

(a) (b)

Figure 4. Simulated invariant mass distributions of (a) muon pairs from $H \to \mu^+\mu^-$ and (b) photon pair from $H \to \gamma\gamma$ of $e^+e^- \to ZH$ events. The $m_{\mu^+\mu^-}$ distribution is fit with a Gaussian core plus a small low-mass tail from the Bremsstrahlung radiation. The Gaussian has a width of 0.2 GeV, representing a relative mass resolution of 0.16%. The $m_{\gamma\gamma}$ distribution is fit with two Gaussians with the dominant one accounts for about 80% of the weight and having a width of 2.4 GeV, corresponding to a relative mass resolution of 1.9%.

reconstructed dijet invariant mass distributions of the $W \to q\bar{q}$, $Z \to q\bar{q}$ and $H \to b\bar{b}/c\bar{c}/gg$ decays from the $ZZ \to \nu\bar{\nu}\, q\bar{q}$, $WW \to \ell\nu\, q\bar{q}$ and $ZH \to \nu\bar{\nu}\, b\bar{b}/c\bar{c}/gg$ processes respectively. The CEPC-v1 detector has sufficiently good mass resolutions to separate W, Z and H bosons in their hadronic decays. The jet energy resolution is expected to be between 3–6% depending on the jet energy. This resolution is approximately 2–4 times better than those of the LHC experiments.

Jets originating from heavy flavors (b- or c-quarks) are tagged using the LCFIPlus algorithm [23]. The algorithm combines information from the secondary vertex, jet mass, number of leptons etc. to construct b-jet and c-jet discriminating variables. The tagging performance characterized using the $Z \to q\bar{q}$ decays from the Z pole running is shown in Fig. 6. For an inclusive $Z \to q\bar{q}$ sample, b-jets can be tagged with an efficiency of 80% and a purity of 90% while the corresponding efficiency and purity for tagging c-jets are 60% and 60%, respectively.

2.4 Ongoing optimization

The CEPC-v1 detector concept is used as the reference for the Higgs boson studies summarized in this paper. A series of optimizations have been performed meanwhile. These optimizations are intended to reduce the power consumption and the construction cost and to improve the machine-detector interface while minimizing negative impacts on the Higgs

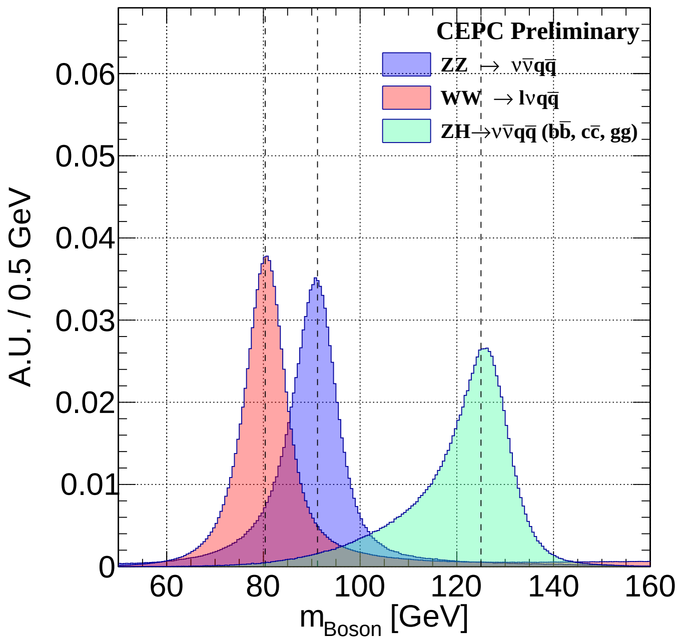

Figure 5. Distributions of the reconstructed dijet invariant mass for the $W \to q\bar{q}$, $Z \to q\bar{q}$ and $H \to b\bar{b}/c\bar{c}/gg$ decays from respectively the $WW \to \ell\nu q\bar{q}$, $ZZ \to \nu\bar{\nu}q\bar{q}$ and $ZH \to \nu\bar{\nu}\, b\bar{b}/c\bar{c}/gg$ processes.

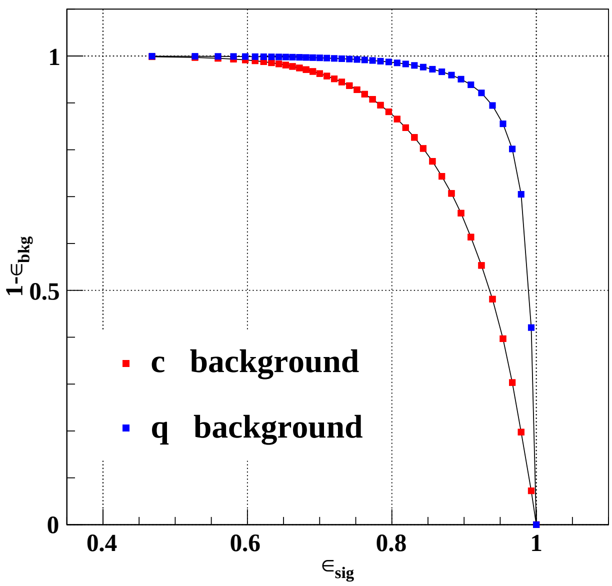

Figure 6. Efficiency for tagging b-jets vs rejection for light-jet background (blue) and c-jet background (red), determined from an inclusive $Z \to q\bar{q}$ sample at the Z pole running.

boson physics. An updated detector concept, CEPC-v4, has thus been developed. The

CEPC-v4 has a smaller solenoidal field of 3 Tesla and a reduced calorimeter dimensions along with fewer readout channels. A new Time-of-Flight measurement capability is added to improve the heavy flavor physics potential.

The weaker magnetic field degrades the track momentum resolution by 14% which translates directly into a degraded muon momentum resolution. However the impact on other physics objects such as electrons, photons and jets are estimated to be small as the track momentum resolution is not a dominant factor for the performances of these objects. For Higgs boson physics, distributions most affected by the change are the $H \to \mu^+\mu^-$ dimuon invariant mass and $Z \to \mu^+\mu^-$ recoil mass. Figure XX compares these distributions from CEPC-v1 and CEPC-v4. some text on the differences.

Suggest to add a figure comparing distributions of $H \to \mu^+\mu^-$ mass and $Z \to \mu^+\mu^-$ recoil mass between CEPC-v1 and CEPC-v4.

3 Production cross sections of signal and background processes

Production processes for a 125 GeV SM Higgs boson at the CEPC operating at $\sqrt{s} \sim$ 240 − 250 GeV are $e^+e^- \to ZH$ (ZH associate production or Higgsstrahlung), $e^+e^- \to \nu\bar{\nu}H$ (W fusion) and $e^+e^- \to e^+e^-H$ (Z fusion) as illustrated in Fig. 7. The W and Z fusion processes are collectively referred to as vector-boson fusion (VBF) production.

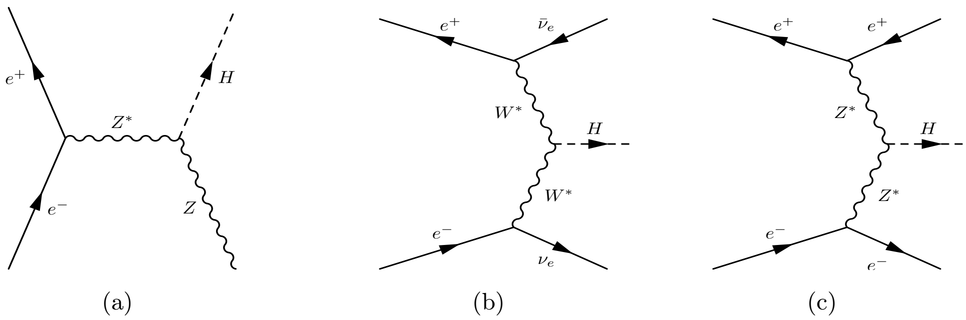

Figure 7. Feynman diagrams of the Higgs boson production processes at the CEPC: (a) $e^+e^- \to ZH$, (b) $e^+e^- \to \nu\bar{\nu}H$ and (c) $e^+e^- \to e^+e^-H$.

The total and individual cross sections for the production of a SM Higgs boson with a mass of 125 GeV as functions of center-of-mass energy are plotted in Fig. 8 while its decay branching ratios and total width are shown in Table 3. As an s-channel process, the cross section of the $e^+e^- \to ZH$ process reaches its maximum at $\sqrt{s} \sim 250$ GeV, and then decreases asymptotically as $1/s$. The VBF production processes are through $t-$channel exchanges of vector bosons. Their cross sections increase logarithmically as $\ln^2(s/M_V^2)$. Because of the accidental small neutral-current Zee coupling, the VBF cross section is dominated by the W fusion process. Numerical values of these cross sections at $\sqrt{s} = 250$ GeV are listed in Table 4.

The CEPC is designed to deliver a total of 5 ab^{-1} integrated luminosity to two detectors in 10 years. Over 10^6 Higgs boson events will be produced during this period. The large statistics, well-defined event kinematics and clean collision environment will enable the CEPC to measure Higgs boson production cross sections as well as its properties (mass, decay width and branching ratios, etc.) with precision far beyond those achievable at the LHC. Compared with hadron collisions, e^+e^- collisions are unaffected by underlying event and pile-up effects. Theoretical calculations are less dependent on higher order QCD radiative corrections. Therefore, more precise tests of theoretical predictions can be performed at the CEPC. The tagging of $e^+e^- \to ZH$ events using recoil mass, independent of the Higgs boson decay, is unique to lepton colliders. It provides a powerful tool for the model-independent measurements of the inclusive $e^+e^- \to ZH$ production cross section, $\sigma(ZH)$, and of Higgs boson decay branching ratios. Combinations of these measurements will enable to determine the total Higgs boson decay width and to extract the Higgs boson couplings to fermions and vector bosons, providing sensitive probes to potential new physics beyond the SM.

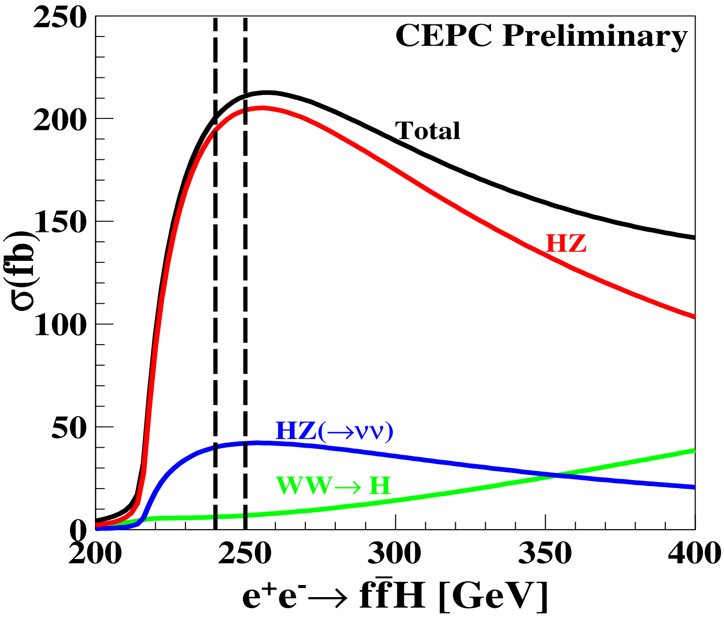

Figure 8. Production cross sections of $e^+e^- \to ZH$ and $e^+e^- \to (e^+e^-/\nu\bar{\nu})H$ as functions of $\sqrt{s}$ for a 125 GeV SM Higgs boson.

Table 3. Standard model predictions of the decay branching ratios and total width of a 125 GeV Higgs boson. These numbers are obtained from Refs. [24, 25].

Decay mode	Branching ratio	Relative uncertainties
$H \to b\bar{b}$	57.7%	+3.2%, −3.3%
$H \to c\bar{c}$	2.91%	+12%, −12%
$H \to \tau^+\tau^-$	6.32%	+5.7%, −5.7%
$H \to \mu^+\mu^-$	2.19×10^{-4}	+6.0%, −5.9%
$H \to WW^*$	21.5%	+4.3%, −4.2%
$H \to ZZ^*$	2.64%	+4.3%, −4.2%
$H \to \gamma\gamma$	2.28×10^{-3}	+5.0%, −4.9%
$H \to Z\gamma$	1.53×10^{-3}	+9.0%, −8.8%
$H \to gg$	8.57%	+10%, −10%
Γ_H	4.07 MeV	+4.0%, −4.0%

Apart from Higgs boson production, other SM processes include $e^+e^- \to e^+e^-$ (Bhabha scattering), $e^+e^- \to Z\gamma$ (ISR return), $e^+e^- \to WW/ZZ$ (diboson) as well as the single boson production of $e^+e^- \to e^+e^-Z$ and $e^+e^- \to e^+\nu W^-/e^-\bar{\nu}W^+$. Their cross sections and expected numbers of events for an integrated luminosity of 5 ab^{-1} at $\sqrt{s} = 250$ GeV are shown in Table 4 as well. The energy dependence of the cross sections for these and the Higgs

Table 4. Cross sections of Higgs boson production and other SM processes at $\sqrt{s} = 250$ GeV and numbers of events expected in 5 ab^{-1}. The cross sections are calculated using the Whizard program [26]. Note that cross sections do not include potential interference effects between the same final states from different processes after W and Z boson decays (see text).

Process	Cross section	Events in 5 ab^{-1}
Higgs boson production, cross section in fb		
$e^+e^- \to ZH$	212	1.06×10^6
$e^+e^- \to \nu\bar{\nu}H$	6.72	3.36×10^4
$e^+e^- \to e^+e^-H$	0.63	3.15×10^3
Total	219	1.10×10^6
Background processes, cross section in pb		
$e^+e^- \to e^+e^-$ (Bhabha)	25.1	1.3×10^8
$e^+e^- \to q\bar{q}\,(\gamma)$	50.2	2.5×10^8
$e^+e^- \to \mu^+\mu^-\,(\gamma)$ [or $\tau^+\tau^-\,(\gamma)$]	4.40	2.2×10^7
$e^+e^- \to WW$	15.4	7.7×10^7
$e^+e^- \to ZZ$	1.03	5.2×10^6
$e^+e^- \to e^+e^-Z$	4.73	2.4×10^7
$e^+e^- \to e^+\nu W^-/e^-\bar{\nu}W^+$	5.14	2.6×10^7

boson production processes are shown Fig. 9. Note that many of these processes can lead to identical final states and thus can interfere. For example, $e^+e^- \to e^+\nu_e W^- \to e^+\nu_e e^-\bar{\nu}_e$ and $e^+e^- \to e^+e^-Z \to e^+e^-\nu_e\bar{\nu}_e$ have the same final state. Unless otherwise noted, these processes are simulated together to take into account interference effects for the studies presented in this paper.

Along with 10^6 Higgs boson events, 5×10^6 ZZ, 8×10^7 WW and 2.5×10^8 $q\bar{q}(\gamma)$ events will be produced. Though these events are backgrounds to Higgs boson events, they are important for the calibration and characterization of the detector performances and for the measurements of electroweak parameters.

The following software tools have been used to obtain the results reported in this paper. GuineaPig program [27, 28] is used to study beam backgrounds and its energy spectrum. A full set of SM samples, including both the Higgs boson signal and SM background events, are generated with Whizard [26]. In addition, Madgraph [29] and Pythia [30] event generators are used to produce samples for the studies of Higgs boson exotic decays. The CEPC detector simulation is based on the software framework used for ILC studies [31]. However, changes have been made to both the simulation (Mokka [18]) and reconstruction software to adapt to the CEPC detector geometry.

All Higgs boson signal samples and part of the leading background samples are processed with Geant 4 [19] based full detector simulation and reconstruction. The rest of backgrounds are simulated with a dedicated fast simulation tool, where the detector acceptances, efficiencies, intrinsic resolutions for different physics objects are parametrized.

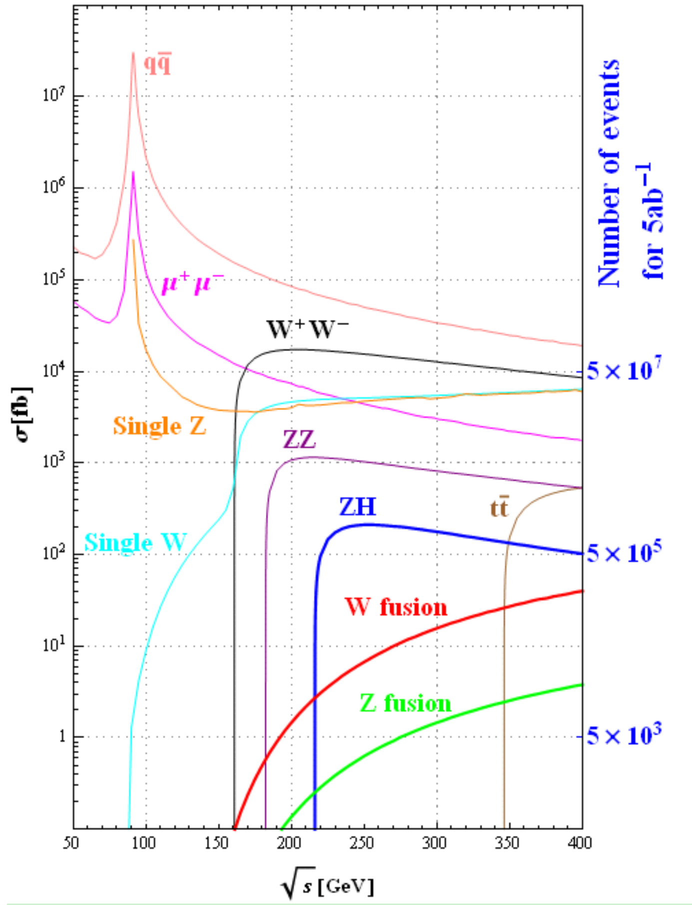

Figure 9. Cross sections of main Standard Model processes of e^+e^- collisions as functions of center-of-mass energy $\sqrt{s}$ obtained from the Whizard program [26]. The calculations include initial-state radiations (ISR). The single W and Z processes refer to $e^+e^- \to e^+\nu W^-/e^-\bar{\nu}W^+$ and $e^+e^- \to e^+e^-Z$ production, respectively. The W and Z fusion processes refer to $e^+e^- \to \nu\bar{\nu}H$ and $e^+e^- \to e^+e^-H$ production, respectively. Their numerical values at $\sqrt{s} = 250$ GeV can be found in Table 4.

Samples simulated for ILC studies [32] are used for cross checks of some studies.

The center-of-mass energy of the CEPC Higgs run has not been finalized. While the studies of the CEPC machine have assumed an operating energy of $\sqrt{s} = 240$ GeV, an energy 250 GeV is chosen for the physics studies presented in this paper to be directly comparable to the studies for the ILC and TLEP [33, 34]. However, the results expected from these two energies are expected to be very similar.

4 Higgs boson tagging using recoil mass

Unlike hadron collisions, the initial-state energy of e^+e^- collisions is controllable and measurable. For a Higgsstrahlung event where the Z boson decays to a pair of visible fermions (ff), the mass of the system recoiling against the Z boson, commonly known as the recoil mass, can be calculated assuming the event has a total energy $\sqrt{s}$ and zero total momentum:

$$M_{\mathrm{recoil}}^2 = (\sqrt{s} - E_{ff})^2 - p_{ff}^2 = s - 2E_{ff}\sqrt{s} + m_{ff}^2. \tag{4.1}$$

Here E_{ff}, p_{ff} and m_{ff} are, respectively, the total energy, momentum and invariant mass of the fermion pair. The M_{recoil} distribution should show a peak at the Higgs boson mass m_H for $e^+e^- \to ZH$ and $e^+e^- \to eeH$ processes, and is expected to be smooth without a resonance structure for other processes in the mass region around 125 GeV.

Two important measurements of the Higgs boson can be performed from the M_{recoil} mass spectrum. The Higgs boson mass can be measured from the peak position of the resonance. The width of the resonance is dominated by the beam energy spread (including ISR effects) and energy/momentum resolution of the detector as the natural Higgs boson width is only 4.07 MeV. The best precision of the mass measurement can be achieved from the leptonic $Z \to \ell^+\ell^-$ ($\ell = e, \mu$) decays. The height of the resonance is a measure of the Higgs boson production cross section $\sigma(ZH)$[2]. By fitting the M_{recoil} spectrum, the $e^+e^- \to ZH$ event yield, and therefore $\sigma(ZH)$, can be extracted, independent of Higgs boson decays. The partial Higgs boson decay width $\Gamma(H \to ZZ)$, or equivalently the Higgs-Z boson coupling $g(HZZ)$, can be derived in a model-independent manner. The latter is an essential input to the determination of the total Higgs boson decay width. Furthermore, Higgs boson branching ratios can then be measured by studying Higgs boson decays in selected $e^+e^- \to ZH$ candidates. The recoil mass spectrum has been investigated for both leptonic and hadronic Z boson decays as presented below.

4.1 $Z \to \ell^+\ell^-$

Events with leptonic Z decays are ideal for studying the recoil mass spectrum of the $e^+e^- \to ZX$ events. $Z \to \ell^+\ell^-$ decays are easily identifiable and the lepton momenta can be precisely measured. Figure 10 shows the reconstructed recoil mass spectra of $e^+e^- \to ZX$ candidates in the $Z \to \mu^+\mu^-$ and $Z \to e^+e^-$ decays. The analyses are based on the full detector simulation for the signal events and on the fast detector simulation for background events. They are performed with event selections entirely based on the information of the two leptons, independent of the final states of Higgs boson decays. This approach is essential for the measurement of the inclusive $e^+e^- \to ZH$ production cross section and the model-independent determination of the Higgs boson branching ratios. SM processes with at least 2 leptons in their final states are considered as backgrounds.

The event selection of the $Z \to \mu^+\mu^-$ analysis starts with the requirement of a pair of identified muons. Events must have the dimuon invariant mass in the range $80 - 100$ GeV and the recoil mass between 120 GeV and 140 GeV. The muon pair is required to have its transverse momentum larger than 20 GeV, and its acolinear angle smaller than 175°. A Boost Decision Tree (BDT) technique is employed to enhance the separation between signal and background events. The BDT is trained using the invariant mass, transverse momentum, polar angle and acollinearity of the dimuon system. For an integrated luminosity of 5 ab^{-1}, about 22 k of $e^+e^- \to ZH \to \mu^+\mu^- H$ signal events (corresponding to a selection

[2] For the $Z \to e^+e^-$ decay, there will be a small contribution from $e^+e^- \to e^+e^-H$ production.

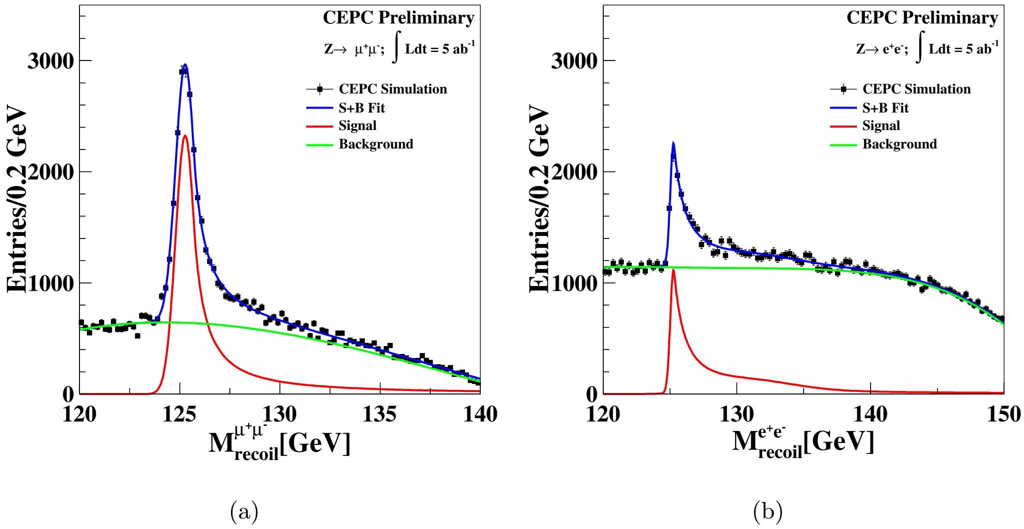

Figure 10. The recoil mass spectra of $e^+e^- \to ZX$ candidates for (a) $Z \to \mu^+\mu^-$ and (b) $Z \to e^+e^-$ with an integrated luminosity of 5 ab^{-1}.

efficiency of $\sim 62\%$) and 48 k background events pass the selection. Leading background contributions after the selection are from ZZ, WW and $Z\gamma$ events. As shown in Fig. 10(a), the analysis has a good signal-to-background ratio. The long high-mass tail is largely due to the initial-state radiation.

Compared to the analysis of the $Z \to \mu^+\mu^-$ decay, the analysis of the $Z \to e^+e^-$ decay suffers from additional and large background contributions from Bhabha and single boson production. A cut based event selection is performed for the $Z \to e^+e^-$ decay. The electron-positron pair is required to have its invariant mass in the range $86.2-96.2$ GeV and its recoil mass between 120 GeV and 150 GeV. Additional selections based on the kinematic variables of the electron-positron pair system, the polar angles and the energies of the selected electron and positron, are applied. Events from $e^+e^- \to e^+e^-(\gamma)$, $e^+\nu W^-$ ($e^-\bar{\nu}W^+$), e^+e^-Z production are the dominant backgrounds after the selection. This simple cut-based event selection results in 10k signal events (27% selection efficiency) and 147k background events for an integrated luminosity of 5 ab^{-1}. Their recoil mass distributions are shown in Fig. 10 (b).

Event selections independent of Higgs boson decays are essential for the model-independent measurement of $\sigma(ZH)$. Additional selections using the Higgs boson decay information can, however, be applied to improve the Higgs boson mass measurement. This will be particularly effective in suppressing the large backgrounds from Bhabha scattering and single W or Z boson production for the analysis of the $Z \to e^+e^-$ decay. This improvement is not implemented in the current study.

4.2 $Z \to q\bar{q}$

The recoil mass technique can also be applied to the hadronic Z boson decays ($Z \to q\bar{q}$) of the $e^+e^- \to ZX$ candidates. This analysis benefits from a larger $Z \to q\bar{q}$ decay branching ratio, but suffers from the fact that jet energy resolution is worse than the track momentum and electromagnetic energy resolutions. In addition, ambiguity in selecting jets from the $Z \to q\bar{q}$ decay, particularly in events with hadronic decays of the Higgs boson, can degrade the analysis performance and also introduce model-dependence to the analysis. Therefore, the measurement is highly dependent on the performance of the PFA and the jet clustering algorithm.

Following the same approach as the ILC study [35], an analysis based on the fast simulation has been performed [35]. After the event selection, main backgrounds arise from WW and $Z\gamma$ production. Figure 11 shows the reconstructed recoil mass distribution. Compared with the leptonic decays, the signal-to-background ratio is considerably worse and the recoil mass resolution is significantly poorer.

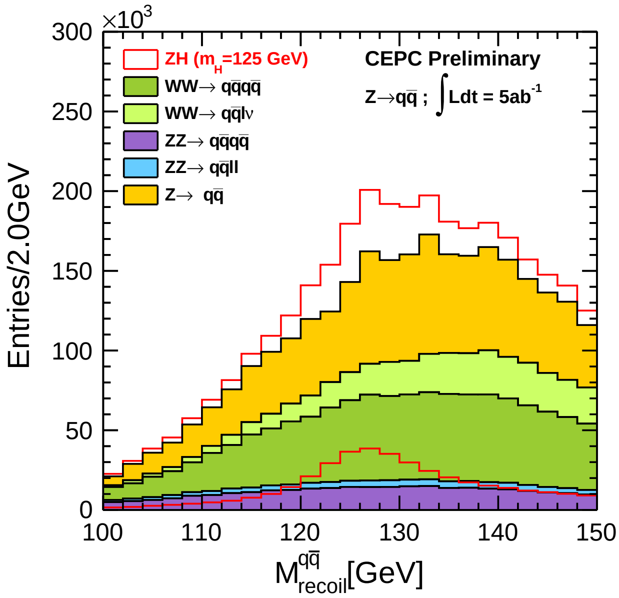

Figure 11. The recoil mass spectrum of the $e^+e^- \to ZX$ candidates in the $Z \to q\bar{q}$ decay channel for 5 ab^{-1} integrated luminosity.

4.3 Measurements of $\sigma(ZH)$ and m_H

The inclusive $e^+e^- \to ZH$ production cross section $\sigma(ZH)$ and Higgs boson mass m_H can be extracted from fits to the recoil mass distributions of the $e^+e^- \to Z+X \to \ell^+\ell^-/q\bar{q}+X$ candidates (Figs. 10, 11). For the leptonic $Z \to \ell^+\ell^-$ decays, the recoil mass distribution of the signal process $e^+e^- \to ZH$ (and $e^+e^- \to e^+e^-H$ for the $Z \to e^+e^-$ decay) is modeled with a Crystal Ball function whereas the total background is modeled with a polynomial function in the fit. As noted above, the recoil mass distribution is insensitive to the intrinsic Higgs boson width if it were as small as predicted by the SM. The Higgs boson mass can be determined with precision of 6.5 MeV and 14 MeV from the $Z \to \mu^+\mu^-$ and $Z \to e^+e^-$ decay modes, respectively. In combination, an uncertainty of 5.9 MeV can be achieved. Is beam energy spread taking into account? $e^+e^- \to Z + X \to q\bar{q} + X$ events contribute little to the precision of the Higgs boson mass measurement due to the poor $Z \to q\bar{q}$ mass resolution, but dominates the precision of the $e^+e^- \to ZH$ cross section measurement benefiting from its large statistics. A relative precision of 0.65% of $\sigma(ZH)$ is predicted from a simple event counting analysis. In comparison, the corresponding precision from the $Z \to e^+e^-$ and $Z \to \mu^+\mu^-$ decays is estimated to be 2.1% and 0.9%, respectively. The combined precision of the three measurements is 0.5%. Table 5 summarizes the expected precisions on m_H and $\sigma(ZH)$ from a CEPC dataset of 5 ab^{-1}.

Table 5. Estimated measurement precision for the Higgs boson mass m_H and the $e^+e^- \to ZH$ production cross section $\sigma(ZH)$ from a CEPC dataset of 5 ab^{-1}.

Z decay mode	Δm_H (MeV)	$\Delta\sigma(ZH)/\sigma(ZH)$
e^+e^-	14	2.1%
$\mu^+\mu^-$	6.5	0.9%
$q\bar{q}$	−	0.65%
$e^+e^- + \mu^+\mu^- + q\bar{q}$	5.9	0.5%

5 Analyses of Individual Decay Modes

Different decay modes of the Higgs boson can be identified through their unique signatures, leading to the measurements of production rates for these decays. For the $e^+e^- \to ZH$ production process in particular, the candidate events can be tagged from the visible decays of the Z bosons, the Higgs boson decays can then be probed by studying the rest of the events. These measurements combined with the inclusive $\sigma(ZH)$ measurement discussed above will permit the extraction of the Higgs boson decay branching ratios in a model-independent way.

In this section, the results of the current CEPC simulation studies of many different Higgs boson decay modes are summarized. The expected relative precision from a CEPC dataset of 5 ab^{-1} on the product of the ZH cross section and the Higgs boson decay branching ratio, $\sigma(ZH) \times \text{BR}$, are presented. Detailed discussions of individual analyses are beyond the scope of this paper and therefore only their main features are presented. For the study of a specific Higgs boson decay mode, the other decay modes of the Higgs boson often contribute as well. These contributions are fixed to their SM expectations unless otherwise noted. However for the combination of all decay modes studied, they are allowed to vary within the constraints of the measurements of those decays.

In addition to the invariant and recoil mass, two other mass observables, visible mass and missing mass, are often used in analyses described below. They are defined, respectively, as the invariant mass and recoil mass of all visible particles such as charged leptons, photons and jets, *i.e.* practically all particles other than neutrinos.

Though the current study covers a large number of final states of the ZH production, there are many remain to be studied. The sensitivities of some important missing final states are obtained by extrapolating from the ILC and FCC-ee studies [32, 34] whenever possible. The extrapolation assumes the same signal and background selection efficiencies, but takes into account differences such as beam polarization conditions. The expected yields for the signal and background processes are scaled to an integrated luminosity of 5 ab^{-1}.

5.1 $H \to b\bar{b}$, $c\bar{c}$, gg

For a SM Higgs boson with a mass of 125 GeV, nearly 70% of all Higgs bosons decay into a pair of jets: b-quarks (57.7%), c-quarks (2.9%) and gluons (8.6%). Deviations in branching ratios from the SM values are predicted in many beyond SM scenarios. New physics models, e.g. SUSY, 2HDM and others [36], predict different Higgs boson coupling to b-quarks, leading to potentially large deviations in BR($H \to b\bar{b}$) from its SM value. The Higgs boson couples to gluons through mainly the top-quark loop in the SM. Thus BR($H \to gg$) is sensitive to new colored and massive particles such as a top-quark partner. The Higgs boson coupling to c-quarks is likely to be the only coupling to the second generation quarks that can be probed at collider experiments. It's comparison with the Higgs boson couplings to the third-generation quarks will provide sensitive tests of fermion mass generation mechanism in the SM.

Experimentally, these measurements pose critical challenges to the CEPC detector performance, particularly its ability to tag b- and c-quark jets from light-flavored jets (u, d, s, g). Thus they are good benchmarks for the design and optimization of the jet flavor tagging performance of the CEPC detector.

Studies are performed in details for $e^+e^- \to ZH$ production with the leptonic decays of the Z bosons. The contribution from the Z-fusion process of $e^+e^- \to e^+e^-H$ is included in the $e^+e^- \to ZH \to e^+e^-H$ study. The analysis is based on full simulation for the Higgs boson signal samples and fast simulation for the $\ell^+\ell^-q\bar{q}$ background samples. After selecting the two leading leptons with opposite charge, the rest of the reconstructed particles are clustered into two jets to form a hadronically decaying Higgs boson candidate, whose invariant mass is required to be between 75 GeV and 150 GeV. The dilepton invariant mass is required to be within $70-110$ GeV for the e^+e^- channel and $81-101$ GeV for the $\mu^+\mu^-$ channel. Moreover, the dilepton system must have its transverse momentum in the range $10-90$ GeV and its recoil mass between 120 GeV and 150 GeV. In addition, a requirement on the polar angle of the Higgs boson candidate, $|\cos\theta_H| < 0.8$, is applied.

In order to identify the flavors of the two jets of the Higgs boson candidate, variables L_B and L_C are constructed from information such as the secondary decay vertex etc. The values of L_B (L_C) are close to one if both jets are originated from $b\,(c)$ quarks and are close to zero if both have light-quark or gluon origins. An unbinned maximum likelihood fit to the M_{recoil}, L_B and L_C distributions of candidate events is used to extract the individual signal yields of the $H \to b\bar{b}$, $H \to c\bar{c}$ and $H \to gg$ decay modes. The total probability density function (PDF) is the sum of signal and background components. For signals, their M_{recoil} PDFs are modeled by Crystal Ball functions with small exponential tails. The background PDF is taken as a sum of two components: a background from Higgs decays to other final states such as WW and ZZ, and a combinatorial background from other sources, dominated by the $e^+e^- \to ZZ \to \ell\ell q\bar{q}$ production. The background from other Higgs

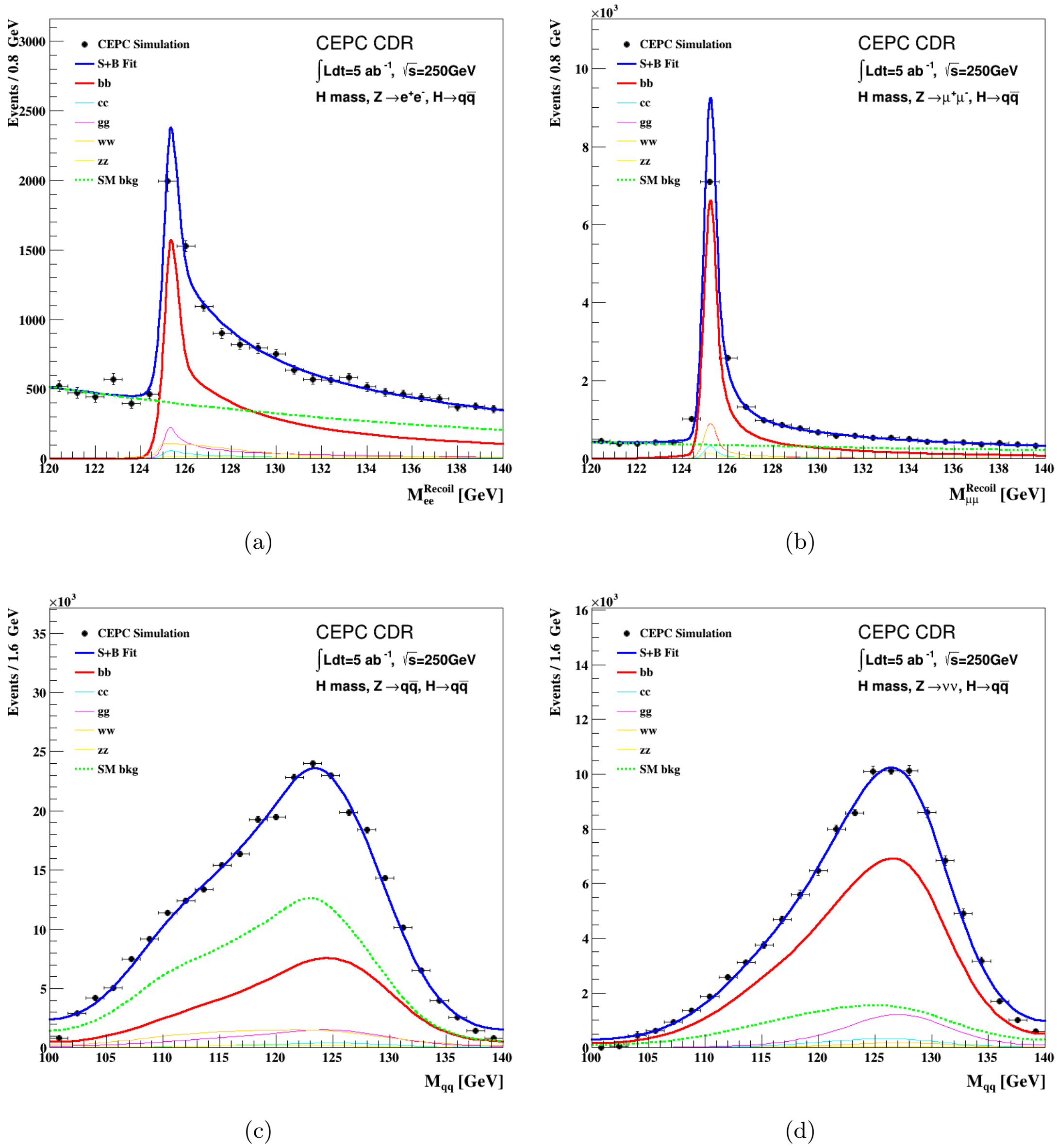

Figure 12. ZH production with $H \to b\bar{b}$, $c\bar{c}$ and gg decays: the recoil mass distributions of (a) $Z \to e^+e^-$ and (b) $Z \to \mu^+\mu^-$; the dijet mass distributions of Higgs boson candidates for (c) $Z \to q\bar{q}$ and (d) $Z \to \nu\bar{\nu}$.

boson decay channels has the same M_{recoil} PDF as the signals. The M_{recoil} distribution of the combinatorial background is modeled by a second order polynomial. The PDFs of the signal L_B and L_C distributions are described by two dimensional histograms, taken from the MC simulated events. The L_B and L_C distributions of both background components are modeled by 2-dimensional histogram PDFs based on the MC simulation. The simulated data and the fit results in the $Z \to \ell^+\ell^-$ channel are shown in Fig. 12 (a,b). All of the fit parameters are extracted from the fit to the data sample except that the normalization of the background due to other Higgs boson decays is fixed to the value predicted by the MC simulation. The estimated relative statistical precision of the measurements of $\sigma(ZH) \times \mathrm{BR}(H \to b\bar{b},\, c\bar{c},\, gg)$ are listed in Table 6.

Table 6 also includes the results of the $Z \to \nu\bar{\nu}$ and $Z \to q\bar{q}$ decays. For the $Z \to q\bar{q}$ final state, events are clustered into four jets and the mass information of jet pairs are used to select the Higgs and Z boson candidates. In addition to ZZ, WW is also a major background for this analysis, particularly for the $H \to c\bar{c}$ and $H \to gg$ decays. As for the $Z \to \nu\bar{\nu}$ final state, events are clustered into two jets are to form the Higgs boson candidate, the invisibly decaying Z boson is inferred from the missing mass of the event. Fits similar to the one used in the analysis of the $Z \to \ell\ell$ channel is subsequently performed to statistically separate the $H \to b\bar{b}$, $c\bar{c}$ and gg decay components. The simulated data and the fitted dijet mass distributions of the Higgs boson candidates are shown in Fig. 12 (c,d) for $Z \to q\bar{q}$ and $Z \to \nu\bar{\nu}$.

Combining all Z boson decay channels, a relative statistical precision for $\sigma(ZH) \times \mathrm{BR}$ of 0.3%, 3.2% and 1.5% can be achieved for the $H \to b\bar{b}$, $c\bar{c}$ and gg decays, respectively.

Table 6. Expected relative precision on $\sigma(ZH) \times \mathrm{BR}$ for the $H \to b\bar{b}$, $c\bar{c}$ and gg decays from a CEPC dataset of 5 ab^{-1}.

Z decay mode	$H \to b\bar{b}$	$H \to c\bar{c}$	$H \to gg$	Comments
$Z \to e^+e^-$	1.3%	14.1%	7.9%	CEPC study
$Z \to \mu^+\mu^-$	1.0%	10.5%	5.4%	CEPC study
$Z \to q\bar{q}$	0.4%	8.1%	5.4%	CEPC study
$Z \to \nu\bar{\nu}$	0.4%	3.8%	1.6%	CEPC study
Combined	0.3%	3.2%	1.5%	

5.2 $H \to WW^*$

For a 125 GeV SM Higgs boson, the $H \to WW^*$ decay has the second largest branching ratio at 21.5% [37]. The measurement of $\sigma(ZH) \times \mathrm{BR}(H \to WW^*)$ provides insight into the nature of the electroweak symmetry breaking mechanism. Moreover, this measurement is a necessary input to the Higgs boson width measurement discussed in Section 6.2. The sensitivity of the measurement is estimated by combining results from different final states of the $H \to WW^*$ decay of ZH production with detailed studies for the $Z \to \ell^+\ell^-$ and $Z \to \nu\bar{\nu}$ decays. The main background process is the SM ZZ production in all cases.

For $Z \to \ell^+\ell^-$, the $H \to WW^*$ decay final states studied are $\ell\nu\ell'\nu$ and $\ell\nu q\bar{q}$. The ZH candidate events are selected by requiring the dilepton invariant mass in the range of 80–100 GeV and their recoil mass in the range of 120–150 GeV. For $Z \to \nu\bar{\nu}$, the $\ell\nu q\bar{q}$ and $q\bar{q}q\bar{q}$ final states are considered for the $H \to WW^*$ decay. The presence of neutrinos results in events with large missing mass, which is required to be in the range of 75–140 (75–150) GeV for the $\ell\nu q\bar{q}$ ($q\bar{q}q\bar{q}$) final state. The total visible mass of the event must be in the range $100 - 150$ GeV for both $\ell\nu q\bar{q}$ and $q\bar{q}q\bar{q}$ final state. In addition, the total transverse momentum of the visible particles must be in the range 20–80 GeV. Additional requirements are applied to improve the signal-background separations. Figure 13 shows the visible and missing mass distributions after the selection of the $Z \to \nu\bar{\nu}$ and $H \to WW^* \to q\bar{q}q\bar{q}$ final state.

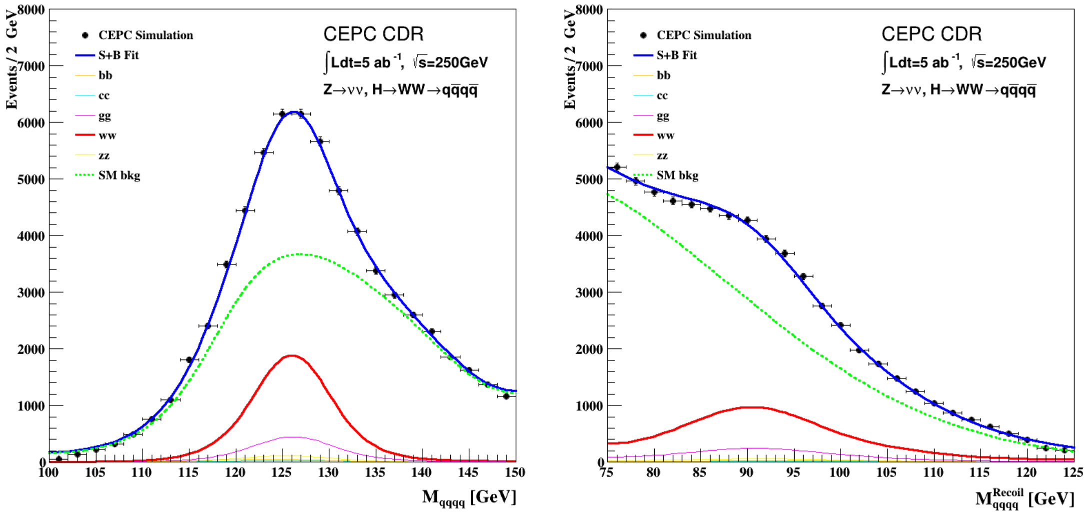

(a) (b)

Figure 13. ZH production with $Z \to \nu\bar{\nu}$ and $H \to WW^* \to q\bar{q}q\bar{q}$: distributions of (a) the visible mass and (b) the missing mass of selected events.

The relative precision on $\sigma(ZH) \times \mathrm{BR}(H \to WW^*)$ from the decay final states studied are summarized in Table 7 assuming an integrated luminosity of 5 ab^{-1}. Also included is the estimated result for $Z \to q\bar{q}$ and $H \to WW^* \to \ell\nu q\bar{q}$, extrapolated from the ILC studies [Ref]. The combination of these decay final states leads to a precision of 1.2%. This is likely a conservative estimate of the precision as many of the final states of the $H \to WW^*$ decay remain to be explored. Including these missing final states will no doubt improve the precision.

Table 7. Expected relative precision on the $\sigma(ZH) \times \mathrm{BR}(H \to WW^*)$ measurement from a CEPC dataset of 5 ab^{-1}. Add $ZH \to 6q$, drop ILC extrapolation?

Decay final state		Precision	Comment
$Z \to e^+e^-$	$H \to WW^* \to \ell\nu\ell'\nu$, $\ell\nu q\bar{q}$	2.83%	CEPC study
$Z \to \mu^+\mu^-$	$H \to WW^* \to \ell\nu\ell'\nu$, $\ell\nu q\bar{q}$	2.63%	CEPC study
$Z \to \nu\bar{\nu}$	$H \to WW^* \to \ell\nu q\bar{q}, q\bar{q}q\bar{q}$	1.9%	CEPC study
$Z \to q\bar{q}$	$H \to WW^* \to \ell\nu q\bar{q}$	2.2%	Extrapolated from ILC
Combined		1.2%	

5.3 $H \to ZZ^*$

The $H \to ZZ^*$ decay has a branching ratio 2.64% [37] for a 125 GeV Higgs boson in the SM. Events from $e^+e^- \to ZH$ production with the $H \to ZZ^*$ decay have three Z bosons in their final states with one of them being off-shell. Z bosons can decay to all lepton and quark flavors, with the exception of the top quark. Consequently, the $e^+e^- \to ZH \to ZZZ^*$ process has a very rich variety of topologies.

Studies are performed for a few selected ZH final states: $Z \to e^+e^-$ and $H \to ZZ^* \to \ell^+\ell^- q\bar{q}$; $Z \to \mu^+\mu^-$ and $H \to ZZ^* \to \nu\bar{\nu}q\bar{q}$; $Z \to \nu\bar{\nu}$ and $H \to ZZ^* \to \ell^+\ell^- q\bar{q}$. The W and Z boson fusion processes, $e^+e^- \to e^+e^-H$ and $e^+e^- \to \nu\bar{\nu}H$, are included in the $Z(e^+e^-)H$ and $Z(\nu\bar{\nu})H$ studies assuming their SM values for the rates. For all the final states, the SM ZZ production is the main background.

For $Z \to e^+e^-$ and $H \to ZZ^* \to \ell^+\ell^- q\bar{q}$, electron pairs must have their invariant masses between 75–105 GeV, recoil masses between 115–165 GeV, and transverse momenta larger than 10 GeV. The invariant masses of the additional lepton pairs must be smaller than 100 GeV and the recoil masses of the jet pairs smaller than 220 GeV. The background is large in this final state, several times of the expected signal after the selection.

For $Z \to \mu^+\mu^-$ and $H \to ZZ^* \to \nu\bar{\nu}q\bar{q}$, the muon pairs must have their invariant masses between 80–100 GeV, recoil masses between 120–160 GeV and transverse momenta larger than 10 GeV. The jet pairs are required to have their invariant masses in the range of 10–38 GeV. Figure 14 (a) shows the recoil mass distribution of $Z \to \mu^+\mu^-$ after the selection. The background is negligible in this final state.

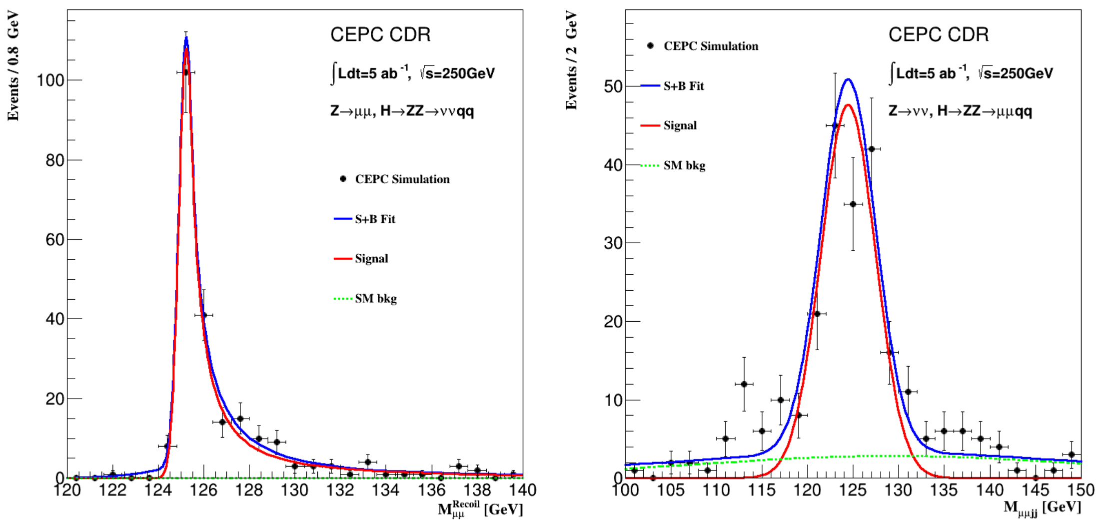

(a) (b)

Figure 14. ZH production with $H \to ZZ^*$: a) the recoil mass distribution of the $\mu^+\mu^-$ system for $Z \to \mu^+\mu^-, H \to ZZ^* \to \nu\bar{\nu}q\bar{q}$; b) the invariant mass distribution of the $\mu^+\mu^- q\bar{q}$ system for $Z \to \nu\bar{\nu}$, $H \to ZZ^* \to \mu^+\mu^- q\bar{q}$.

The candidates of $Z \to \nu\bar{\nu}$ and $H \to ZZ^* \to \ell^+\ell^- q\bar{q}$ are selected by requiring a same-flavor lepton pair and two jets. The total visible energy must be smaller than 180 GeV and the missing mass in the range 58–138 GeV. Additional requirements are applied on the mass and transverse momenta of the lepton and jet pairs. After the selection, the background is about an order of magnitude smaller than the signal.

Table 8 summarizes the expected precision on $\sigma(ZH) \times \mathrm{BR}(H \to ZZ^*)$ from the final states considered for an integrated luminosity of 5 ab^{-1}. The combination of these final states results in a precision of about 5.2%. The sensitivity can be significantly improved considering that many final states are not included in the current study. In particular, the final state of $Z \to q\bar{q}$ and $H \to ZZ^* \to q\bar{q}q\bar{q}$ which represents a third of all $ZH \to ZZZ^*$ decay is not studied. Moreover, gain can also be made using multivariate techniques.

Table 8. Expected relative precision for the $\sigma(ZH) \times \mathrm{BR}(H \to ZZ^*)$ measurement with an integrated luminosity 5 ab^{-1}.

Decay final state		Precision	Comment
$Z \to e^+e^-$	$H \to ZZ^* \to \ell^+\ell^- q\bar{q}$	19.3%	CEPC study
$Z \to \mu^+\mu^-$	$H \to ZZ^* \to \nu\bar{\nu} q\bar{q}$	7.3%	CEPC study
$Z \to \nu\bar{\nu}$	$H \to ZZ^* \to \ell^+\ell^- q\bar{q}$	8.2%	CEPC study
Combined		5.2%	

5.4 $H \to \gamma\gamma$

The diphoton decay of a 125 GeV Higgs boson has a small branching ratio of 0.23% in the SM due to its origin involving massive W boson and top quark in loops. However photons can be identified and measured well, the decay can be fully reconstructed with a good precision. The decay also serves as a good benchmark for the performance of the electromagnetic calorimeter.

Studies are performed for the ZH production with $H \to \gamma\gamma$ and four different Z boson decay modes: $Z \to \mu^+\mu^-$, $\tau^+\tau^-$, $\nu\bar{\nu}$ and $q\bar{q}$. The $Z \to e^+e^-$ decay is not considered because of the expected large background from the Bhabha process. The studies are based on the full detector simulation for the $Z \to q\bar{q}$ decay channel and the fast simulation for the rest. Photon candidates are required to have energies greater than 25 GeV and polar angles of $|\cos\theta| < 0.9$. The photon pair with the highest invariant mass is retained as the $H \to \gamma\gamma$ candidate and its recoil mass of must be consistent with the Z boson mass. For the $Z \to \mu^+\mu^-$ and $Z \to \tau^+\tau^-$ decays, a minimal angle of 8° between any selected photon and lepton is required to suppress backgrounds from the final state radiations. A τ identification efficiency of 90% is assumed for the $Z \to \tau^+\tau^-$ decays. After the selection, the main SM background is the $e^+e^- \to (Z/\gamma^*)\gamma\gamma$ process where the γ's arise from the initial or final state radiations.

The diphoton mass is used as the final discriminant for the final separation of signal and backgrounds. Figure 15 shows... With an energy resolution of $16\%/\sqrt{E} \oplus 1\%$ for the electromagnetic calorimeter and an integrated luminosity of 5 ab^{-1}, a relative precision of 8.1% on $\sigma(ZH) \times \mathrm{BR}(H \to \gamma\gamma)$ can be achieved. The robustness of this projection is examined for different assumptions of the electromagnetic energy resolution. An approximate 2% improvement (degradation) of the relative precision is expected for an optimistic (pessimistic) resolution of $\frac{10\%}{\sqrt{E}} \oplus 1\%$ ($\frac{20\%}{\sqrt{E}} \oplus 1\%$).

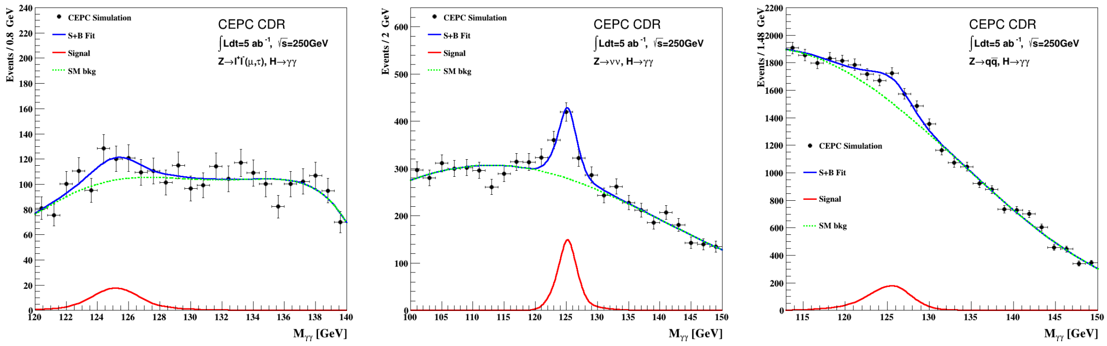

Figure 15. Post-fit Mass spectrum of $Z \to ll$ (a) , $Z \to \nu\nu$ (b) and $Z \to qq$ (c) channel,expected for 5 ab^{-1} of CEPC ZH data. Ideally we want to show the diphoton invariant and recoil mass distributions.

5.5 $H \to Z\gamma$

Similar to the $H \to \gamma\gamma$ decay, the $H \to Z\gamma$ decay in the SM is mediated by W boson and top quark in loops and has a branching ratio of 0.154%. The $H \to Z\gamma$ analysis targets the signal process of $ZH \to ZZ\gamma \to \nu\bar{\nu}q\bar{q}\gamma$, in which one of the Z bosons decays into a pair of quarks and the other decays into a pair of neutrinos.

The candidate events are selected by requiring exactly one photon with transverse energy between 20–50 GeV and at least two hadronic jets, each with transverse energy greater than 10 GeV. The dijet invariant mass and the event missing mass must be within 12 GeV and 15 GeV of the Z boson mass, respectively. Additional requirements are applied on the numbers of tracks and calorimeter clusters as well as on the transverse and longitudinal momenta of the Z boson candidates. The backgrounds are dominated by the processes of single boson, diboson, $q\bar{q}$, and BhaBha production.

After the event selection, the photon is paired with each of the two Z boson candidates to form Higgs boson candidates and the mass differences, dMass $= M_{q\bar{q}\gamma} - M_{q\bar{q}}$ and dMass $= M_{\nu\bar{\nu}\gamma} - M_{\nu\bar{\nu}}$, are calculated. Here the energy and momentum of the $\nu\bar{\nu}$ system are taken to be the missing energy and momentum of the event. For signal events, one of the mass differences is expected to populate around $M_H - M_Z \sim 35$ GeV whereas the other should be part of the continuum background. Figure 16 shows the dMass distribution expected from an integrated luminosity of 5 ab^{-1}. Modeling the signal distribution of the correct pairing with a Gaussian and the background (including wrong-pairing contribution of signal events) with a polynomial, a likelihood fit results a statistical significance of 4σ for the signal, corresponding to a relative precision of 21% on $\sigma(ZH) \times \mathrm{BR}(H \to Z\gamma)$.

This analysis can be improved with additional optimizations and using multivariate techniques. Other decay modes such as $ZH \to ZZ\gamma \to q\bar{q}q\bar{q}\gamma$ should further improve the

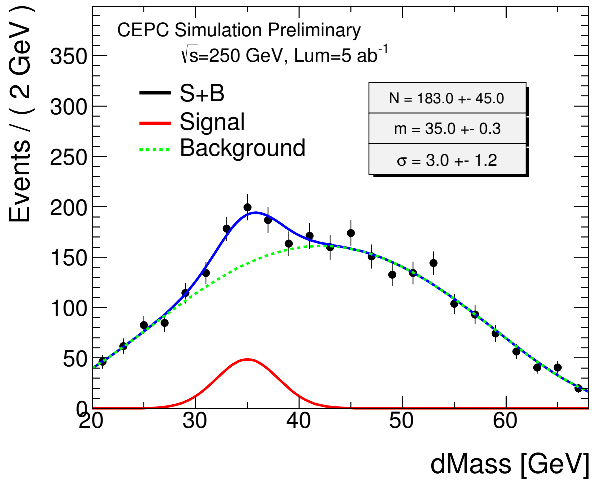

Figure 16. The distribution of the mass differences of $M_{q\bar{q}\gamma} - M_{q\bar{q}}$ and $M_{\nu\bar{\nu}\gamma} - M_{\nu\bar{\nu}}$ of the selected $H \to Z\gamma \to \nu\bar{\nu}q\bar{q}\gamma$ candidates expected from an integrated luminosity of 5 ab^{-1}. The signal distribution shown is for the correct pairings of the Higgs boson decays.

precision on the $\sigma(ZH) \times \mathrm{BR}(H \to Z\gamma)$ measurement.

5.6 $H \to \tau^+\tau^-$

Taus are intriguing physics objects as its Yukawa coupling to the Higgs boson is relatively large, leading to a $H \to \tau^+\tau^-$ decay branching ratio of 6.32% at $m_H = 125$ GeV in the SM. Due to the rich tau decay products, properties such as the Higgs boson CP can be precisely measured. The decay products of tau consist one or three tracks, and a number of neutral pions. The tracks and neutral pions, as well as the two photons from the decay of the latter, can be well resolved and measured by the CEPC detector.

Simulation studies are performed for the $e^+e^- \to ZH$ production with $H \to \tau^+\tau^-$ and $Z \to \mu^+\mu^-, \nu\bar{\nu}$ and $q\bar{q}$ decays. For $Z \to \mu^+\mu^-$, candidates are first required to have a pair of oppositely charged muons with their invariant mass between 40–180 GeV and their recoil mass between 110–180 GeV. For $Z \to \nu\bar{\nu}$, candidates are preselected by requiring a missing mass in the range of 65–225 GeV, a visible mass greater than 50 GeV and an event visible transverse momentum between 10–100 GeV. For both decays, a BDT selection is applied after the preselection to identify di-tau candidates. The BDT utilizes information such as numbers of tracks and photons and the angles between them. After these selections, the ZH production with the non-tau decays of the Higgs boson is the dominant (>95%) background for $Z \to \mu^+\mu^-$ and contributes to approximately 40% of the total background for $Z \to \nu\bar{\nu}$. The rest of the background in the $Z \to \nu\bar{\nu}$ channel comes from the diboson production. For $Z \to q\bar{q}$, candidates are required to have a pair of tau candidates with their invariant mass between 20–120 GeV, a pair of jets with their mass between 70–110 GeV and their recoil mass between 100–170 GeV. The main background is again from the ZH production originating from the decay modes other than the intended $ZH \to q\bar{q}\tau^+\tau^-$

decay. The rest of the background is primarily from the ZZ production.

The final signal yields are extracted from fits to the distributions of variables based on the impact parameters of the leading tracks of the two tau candidates as shown in Fig. 17. Table 9 summarizes the estimated precision on $\sigma(ZH) \times \mathrm{BR}(H \to \tau^+\tau^-)$ expected from a CEPC dataset of 5 fb^{-1} for the three Z boson decay modes studied. The precision from the $Z \to e^+e^-$ decay mode extrapolated from the $Z \to \mu^+\mu^-$ study is also included. The $e^+e^- \to e^+e^-H$ contribution from the Z fusion process is fixed to its SM value in the extrapolation. In combination, the relative precision of 0.89% is expected for $\sigma(ZH) \times \mathrm{BR}(H \to \tau^+\tau^-)$.

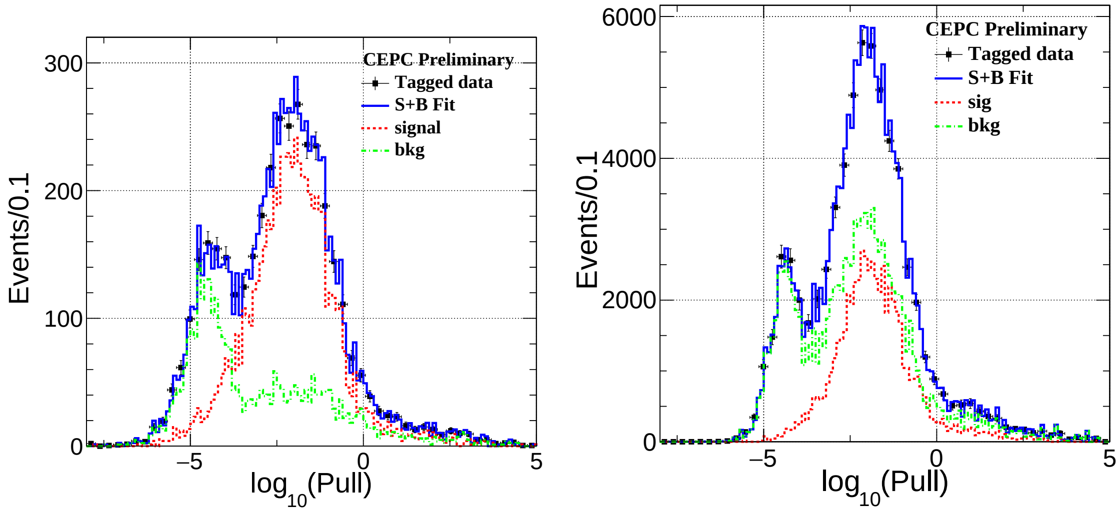

(a) (b)

Figure 17. Distributions of the impact parameter variable based on the leading tracks from the two taus in the $Z \to \ell^+\ell^-$ (a) and $Z \to q\bar{q}$ (b) channel, expected for 5 ab^{-1} of the CEPC data. Here the "Pull" is defined as $(d_0/\sigma_{d_0})^2 + (z_0/\sigma_{z_0})^2$ with d_0 and z_0 being the transverse and longitudinal impact parameters, σ_{d_0} and σ_{z_0} being their uncertainties.

Table 9. Expected relative precision for the $\sigma(ZH) \times \mathrm{BR}(H \to \tau^+\tau^-)$ measurement from a CEPC dataset of 5 ab^{-1}.

Decay final state		Precision	Comment
$Z \to \mu^+\mu^-$	$H \to \tau^+\tau^-$	2.8%	CEPC study
$Z \to e^+e^-$	$H \to \tau^+\tau^-$	3.0%	CEPC extrapolation
$Z \to \nu\bar{\nu}$	$H \to \tau^+\tau^-$	3.1%	CEPC study
$Z \to q\bar{q}$	$H \to \tau^+\tau^-$	1.0%	CEPC study
Combined		0.89%	

The ZH production with $Z \to \ell^+\ell^-, q\bar{q}$ and $H \to \tau^+\tau^-$ can also be used to extract the CP property of the Higgs boson [38]. Using the three tau decay modes with the largest branching ratios ($\pi^{\pm}\nu$, $\pi^{\pm}\pi^{0}\nu$ and $\ell\nu\nu$), the neutrinos from the tau decay are reconstructed from the mass, energy and impact parameter constraints. A matrix element based method is employed to extract the value of the CP mixing angle between the even and odd components of the $H\tau\tau$ coupling. It is estimated that with 5 ab^{-1} of the CEPC data, a precision of 2.9° can be achieved for this angle, which can shed light on the potential BSM physics.

5.7 $H \to \mu^+\mu^-$

The dimuon decay of the Higgs boson, $H \to \mu^+\mu^-$, is sensitive to the Higgs boson coupling to the second-generation fermions with a clean final-state signature. In the SM, the branching ratio of the decay is 2.18×10^{-4} [37] for $m_H = 125$ GeV. Any deviation from the SM prediction could be a sign of new physics. The $H \to \mu^+\mu^-$ decay has been searched for by the ATLAS and CMS Collaborations [39, 40] at the LHC, but has yet to be observed.

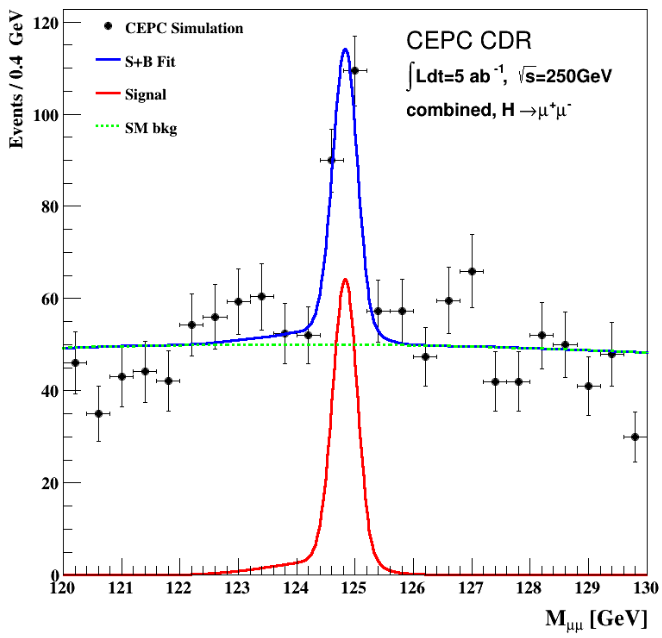

Figure 18. ZH production with the $H \to \mu^+\mu^-$ decay: dimuon invariant mass distribution of the selected $H \to \mu^+\mu^-$ candidates expected from an integrated luminosity of 5 ab^{-1} at the CEPC. The distribution combines contributions from $Z \to \ell^+\ell^-$, $Z \to \nu\bar{\nu}$, and $Z \to q\bar{q}$ decays.

To estimate CEPC's sensitivity for the $H \to \mu^+\mu^-$ decay, studies are performed for the ZH production with the Z decay modes: $Z \to \ell^+\ell^-$, $Z \to \nu\bar{\nu}$, and $Z \to q\bar{q}$. In all cases, the SM production of ZZ is the dominant background source. Candidate events are selected by requiring a pair of muons with its mass between $120 - 130$ GeV and their recoiling mass consistent with the Z boson mass (in the approximate range of $90 - 93$ GeV, depending on the decay mode). Additional requirements are applied to identify specific Z boson decay modes. For $Z \to \ell^+\ell^-$, candidate events must have another lepton pair with its mass consistent with m_Z. In the case of $Z \to \mu^+\mu^-$, the muon pairs of the $Z \to \mu^+\mu^-$ and $H \to \mu^+\mu^-$ decays are selected by minimizing a χ^2 based on their mass differences with m_Z and m_H. For the $Z \to \nu\bar{\nu}$ decay, a requirement on the missing energy is applied. For the $Z \to q\bar{q}$ decay, candidate events must have two jets with their mass consistent with m_Z. To further reduce the ZZ background, differences between the signal and background in kinematic variables, such as the polar angle, transverse momentum and energy of the candidate $H \to \mu^+\mu^-$ muon pair, are exploited. Simple criteria on these variables are applied for the $Z \to \ell^+\ell^-$ and $Z \to \nu\bar{\nu}$ decay mode whereas a BDT is used for the $Z \to q\bar{q}$ decay.

In all analyses, the signal is extracted through unbinned likelihood fits to the $m_{\mu\mu}$ distributions in the range of $120 - 130$ GeV with a signal-plus-background model. Analytical functions are used model both the signal and background distributions. The signal model is a Crystal Ball function while the background model is described by a second-order Chebyshev polynomial. The dimuon mass distribution combining all Z boson decay modes studied is shown in Fig. 18 with the result of the signal-plus-background fit overlaid. The combined relative precision on the $\sigma(ZH) \times \mathrm{BR}(H \to \mu^+\mu^-)$ measurement is estimated to be about 15.9% for 5 ab^{-1} integrated luminosity.

5.8 $H \to \mathrm{inv}$

In the SM, the Higgs boson can decay invisibly via $H \to ZZ^* \to \nu\bar{\nu}\nu\bar{\nu}$, as shown in Fig. 19. For a Higgs boson mass of 125 GeV, this decay has a branching ratio of 1.06×10^{-3}. In many extensions to the SM, the Higgs boson can decay directly to invisible particles Ref.[X]. In this case, the branching ratio can be significantly enhanced.

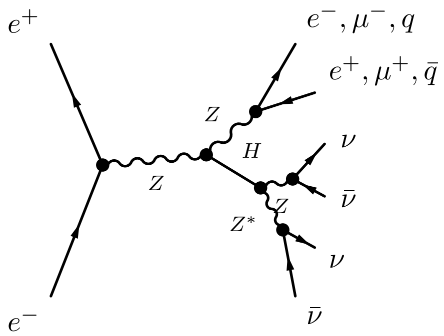

Figure 19. ZH production with the invisible $H \to ZZ^* \to \nu\bar{\nu}\nu\bar{\nu}$ decay in the SM.

The sensitivity of the $\mathrm{BR}(H \to \mathrm{inv})$ measurement is studied for the $Z \to \ell^+\ell^-$ and $Z \to q\bar{q}$ decay modes. The $H \to ZZ^* \to \nu\bar{\nu}\nu\bar{\nu}$ decay is used to model the $H \to \mathrm{inv}$ decay in both the SM and its extensions. This is made possible by the fact that the Higgs boson is narrow scalar so that the production and the decay are fractorized. The main background is the SM ZZ production with one of the Z bosons decay invisibly and the other decays visibly. Candidate events in the $Z \to \ell^+\ell^-$ decay mode are selected by requiring a pair of lepton with its mass between 70–100 GeV and event visible energy in the range 90–120 GeV. Similarly, candidate events in $Z \to q\bar{q}$ are selected by requiring two jets with its mass between 80–105 GeV and event visible energy in the range 90–130 GeV. Additional selections including using a BDT to exploit the kinematic differences between signal and background events are applied.

Table 10 summarizes the expected precision and 95% CL upper limit on BR($H \to$ inv) from a CEPC dataset of 5 ab^{-1} assuming the uncertainty of $\sigma(ZH)$ is negligle compared with the statistical uncertainty of the analysis.

Table 10. Precision and 95% CL upper limit on BR($H \to$ inv) expected from a CEPC dataset of 5 ab^{-1}.

Decay final state		Precision	Upper limit	Comment
$Z \to e^+e^-$	$H \to$ inv	$(0.11 \pm 0.36)\%$	0.84%	CEPC study
$Z \to \mu^+\mu^-$	$H \to$ inv	$(0.11 \pm 0.26)\%$	0.62%	CEPC study
$Z \to q\bar{q}$	$H \to$ inv	$(0.11 \pm 0.24)\%$	0.59%	CEPC study
Combined		$(0.11 \pm 0.16)\%$	0.42%	

5.9 $\sigma(e^+e^- \to \nu\bar{\nu}H) \times \mathrm{BR}(H \to b\bar{b})$

The W-fusion process, $e^+e^- \to \nu\bar{\nu}H$ ($\nu\bar{\nu}H$), has a cross section of 3.2% of that of the ZH process at $\sqrt{s} = 250$ GeV. The product of its cross section and BR($H \to b\bar{b}$), $\sigma(\nu\bar{\nu}H) \times$ BR($H \to b\bar{b}$), is a key input quantity to one of the two model-independent methods for determining the Higgs boson width at the CEPC. The $e^+e^- \to \nu\bar{\nu}H \to \nu\bar{\nu}b\bar{b}$ process has the same final state as the $ZH \to \nu\bar{\nu}b\bar{b}$ process, but has a rate that is approximately one sixth of $ZH \to \nu\bar{\nu}b\bar{b}$ at $\sqrt{s} = 250$ GeV. The main non-Higgs boson background is the SM ZZ production.

The $Z(\nu\bar{\nu})H$ background is irreducible and can also interfere with $\nu\bar{\nu}H$ in the case of $Z \to \nu_e\bar{\nu}_e$. However the interference effect is expected to be small and is therefore not taken into account in the current study. The $\nu\bar{\nu}H$ and $Z(\nu\bar{\nu})H$ contributions can be separated through the exploration of their kinematic differences. While the invariant mass distributions of the two b-quark jets are expected to be indistinguishable, the recoil mass distribution should exhibit a resonance structure at the Z boson mass for $Z(\nu\bar{\nu})H$ and show a continuum spectrum for $\nu\bar{\nu}H$. Furthermore, the H bosons are produced with different polar angular distributions, see Fig. 20 (a).

Candidate events are selected by requiring their visible energies between 105 GeV and 155 GeV, visible masses within 100–135 GeV, and missing masses in the range 65–135 GeV. The two b-quark jets are identified using the B-likeness variable L_B as discussed in Section 5.1. To separate $\nu\bar{\nu}H$ and $Z(\nu\bar{\nu})H$ contributions, a 2-dimensional fit in the plane of the recoil mass and polar angle of the $b\bar{b}$ system is performed. The recoil mass resolution is improved through a kinematic fit by constraining the invariant mass of the two b-jets within its resolution to that of the Higgs boson mass. Figure 20 (b) shows the recoil mass distribution of the $b\bar{b}$ system after the kinematic fit. A fit to the $m_{b\bar{b}} - \cos\theta$ distribution with both rates of $\nu\bar{\nu}H$ and $Z(\nu\bar{\nu})H$ processes as free parameters leads to relative precision of 3.1% for $\sigma(\nu\bar{\nu}H) \times$ BR($H \to b\bar{b}$) and 0.47% for $\sigma(ZH) \times$ BR($H \to b\bar{b}$). The latter

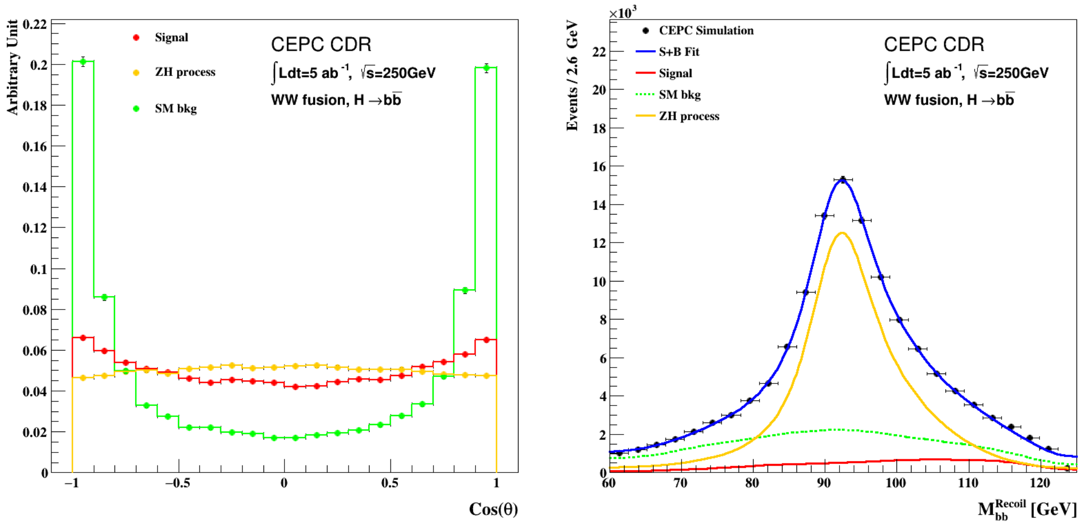

(a) (b)

Figure 20. Distributions of the $b\bar{b}$ system of the $e^+e^- \to \nu\bar{\nu}b\bar{b}$ candidates: (a) cosine of the polar angle θ and (b) the recoil mass. Contributions from $e^+e^- \to \nu\bar{\nu}H$, ZH and other SM processes are shown. The $\cos\theta$ distributions are normalized to unity and therefore only shapes are compared.

is consistent with the study of the $H \to b\bar{b}/c\bar{c}/gg$ decay described in Section 5.1. Fixing the $Z(\nu\bar{\nu})H(b\bar{b})$ contribution to its SM expectation yields a relative precision of 2.8% on $\sigma(\nu\bar{\nu}H) \times \mathrm{BR}(H \to b\bar{b})$.

6 Combinations of Individual Measurements

6.1 Combined Measurements of $\sigma \times \mathrm{BR}$ and BR

With the measurements of inclusive cross section $\sigma(ZH)$ and the cross sections of individual Higgs boson decay mode $\sigma(ZH) \times \mathrm{BR}$, the Higgs boson decay branching ratio BR can be extracted. Most of the systematic uncertainties associated with the measurement of $\sigma(ZH)$ cancels in this procedure. A maximum likelihood fit is used to estimate the precision on BRs. For a given Higgs boson decay mode, the likelihood has the form:

$$L(\mathrm{BR}, \theta) = \mathrm{Poisson}\left[N^{\mathrm{obs}} \middle| N^{\mathrm{exp}}(\mathrm{BR}, \theta)\right] \cdot G(\theta), \tag{6.1}$$

where BR is the parameter of interest and θ represent nuisance parameters associated with systematic uncertainties. N^{obs} is the number of the observed events, $N^{\mathrm{exp}}(\mathrm{BR}, \theta)$ is the expected number of events, and $G(\theta)$ is a set of constraints on the nuisance parameters within their estimated uncertainties. The number of expected events is the sum of signal and background events. The number of signal events is calculated from the integrated luminosity, the $e^+e^- \to ZH$ cross section $\sigma(ZH)$ measured from the recoil method, Higgs boson branching ratio BR, the event selection efficiency ϵ. The number of the expected background events, N^b, is estimated from Monte Carlo samples. Thus

$$N^{\mathrm{exp}}(\mathrm{BR},\theta) = \mathrm{Lumi}(\theta^{\mathrm{lumi}}) \times \sigma_{ZH}(\theta^{\sigma}) \times \mathrm{BR} \times \epsilon(\theta^{\epsilon}) + N^{b}(\theta^{b}), \tag{6.2}$$

where θ^X ($X = \mathrm{lumi}, \sigma$ and ϵ) are the nuisance parameters of their corresponding parameters or measurements. However, systematic uncertainties are not taken into account in the current analyses since statistical uncertainties are expected to be dominant for all measurements. Thus the nuisance parameters are fixed to their nominal values.

For the individual analyses discussed in Section 5, contaminations from Higgs boson production or decays other than the one under study are fixed to their SM values for simplicity. In the combination, however, these constraints are removed and the contaminations are constrained only by the analyses targeted for their measurements. For example, the $H \to b\bar{b}$, $c\bar{c}$, gg analysis suffers from contaminations from the $H \to WW^*, ZZ^* \to q\bar{q}q\bar{q}$ decays. For the analysis discussed in Section 5.1, these contaminations are estimated from SM. In the combination fit, they are constrained by the $H \to WW^*$ and $H \to ZZ^*$ analyses described in Sections 5.2 and 5.3, respectively. Taking into account these across-channel contaminations properly generally leads to small improvements in precision. For example, the precision on $\sigma(ZH)\times\mathrm{BR}(H \to WW^*)$ is improved from 1.2% of the standalone analysis to 1.0% from the combination.

Table 11. Estimated precision of Higgs boson property measurements at the CEPC. All the numbers refer to relative precision except for m_H and $\mathrm{BR}(H \to \mathrm{inv})$ for which Δm_H and 95% CL upper limit are quoted respectively.

Δm_H	Γ_H	$\sigma(ZH)$	$\sigma(\nu\bar{\nu}H) \times \mathrm{BR}(H \to b\bar{b})$
5.9 MeV	3.3%	0.50%	3.1%

Decay mode	$\sigma(ZH) \times \mathrm{BR}$	BR
$H \to b\bar{b}$	0.29%	0.42%
$H \to c\bar{c}$	3.5%	3.5%
$H \to gg$	1.4%	1.5%
$H \to \tau^+\tau^-$	0.8%	0.9%
$H \to WW^*$	1.0%	1.1%
$H \to ZZ^*$	5.0%	5.0%
$H \to \gamma\gamma$	8.2%	8.3%
$H \to \mu^+\mu^-$	16%	16%
$H \to \mathrm{inv}$	–	$< 0.42\%$

Table 11 summarizes the estimated precision of Higgs boson property measurements. For the leading Higgs boson decay modes, namely $b\bar{b}$, $c\bar{c}$, gg, WW^*, ZZ^* and $\tau^+\tau^-$, percent level precision are expected. As it has been discussed in the introduction, this level of precision is required to attain sensitivity to many beyond SM physics scenarios.

The best achievable statistical uncertainties for 5 ab^{-1} are 0.29% for $\sigma(e^+e^- \to ZH) \times \mathrm{BR}(H \to b\bar{b})$ and 0.5% for $\sigma(e^+e^- \to ZH)$. Even for these measurements, statistics is likely the dominant source of uncertainties. Systematic uncertainties from the efficiency/acceptance of the detector, the luminosity and the beam energy determination are expected to be small. The integrated luminosity can be measured with a 0.1% precision, a benchmark already achieved at the LEP [41], and can be potentially improved in the future. The center-of-mass energy will be known better than 1 MeV, resulting negligible uncertainties on the theoretical cross section predictions and experimental recoil mass measurements. In summary, all aforementioned measurements will have uncertainties that are statistically dominated at the CEPC.

6.2 Measurement of Higgs boson width

The Higgs boson width (Γ_H) is of special interest as it is sensitive to BSM physics in Higgs boson decays that are not directly detectable or searched for. However, the 4.2 MeV width predicted by the SM is too small to be measured with a reasonable precision from the distributions of either the invariant mass of the Higgs boson decay products or the recoil mass of the system produced in association with the Higgs boson. Unique to lepton colliders, the width can be determined from the measurements of Higgs boson production cross sections and its decay branching ratios. This is because the inclusive $e^+e^- \to ZH$ cross section $\sigma(ZH)$ can be measured from the recoil mass distribution, independent of Higgs boson decays.

Measurements of $\sigma(ZH)$ and BR's have been discussed in Sections 4 and 5. Combining these measurements, the Higgs boson width can be calculated in a model-independent way:

$$\Gamma_H = \frac{\Gamma(H \to ZZ^*)}{\mathrm{BR}(H \to ZZ^*)} \propto \frac{\sigma(ZH)}{\mathrm{BR}(H \to ZZ^*)} \tag{6.3}$$

Here $\Gamma(H \to ZZ^*)$ is the partial width of the $H \to ZZ^*$ decay. Because of the small expected $\mathrm{BR}(H \to ZZ^*)$ value for a 125 GeV Higgs boson (2.64% in the SM), the precision of Γ_H is limited by the $H \to ZZ^*$ statistics. It can be improved using the decay final states with the expected large BR values, for example the $H \to b\bar{b}$ decay:

$$\Gamma_H = \frac{\Gamma(H \to b\bar{b})}{\mathrm{BR}(H \to b\bar{b})} \tag{6.4}$$

$\Gamma(H \to bb)$ can be independently extracted from the cross section of the W fusion process $e^+e^- \to \nu\bar{\nu}H \to \nu\bar{\nu}\, b\bar{b}$:

$$\sigma(\nu\bar{\nu}H \to \nu\bar{\nu}\, b\bar{b}) \propto \Gamma(H \to WW^*) \cdot \mathrm{BR}(H \to b\bar{b}) = \Gamma(H \to b\bar{b}) \cdot \mathrm{BR}(H \to WW^*) \tag{6.5}$$

Thus the Higgs boson total width

$$\Gamma_H = \frac{\Gamma(H \to WW^*)}{\mathrm{BR}(H \to WW^*)} \propto \frac{\sigma(\nu\bar{\nu}H \to \nu\bar{\nu}\, b\bar{b})}{\mathrm{BR}(H \to b\bar{b}) \cdot \mathrm{BR}(H \to WW^*)} \tag{6.6}$$

Here $\mathrm{BR}(H \to b\bar{b})$ and $\mathrm{BR}(H \to WW^*)$ are measured from the $e^+e^- \to ZH$ process. The limitation of this method is the precision of the $\sigma(e^+e^- \to \nu\bar{\nu}H \to \nu\bar{\nu}\, b\bar{b})$ measurement.

The precision from the method of 6.3 is 5.4%, dominated by the statistics of $e^+e^- \to ZH$ events with $H \to ZZ^*$, after ignoring the measurements correlation with other channels. Keeping only the correlations between the measured sub channels appearing in the expression of 6.4, the precision on Higgs width is is 3.7%, dominated by the statistics of $e^+e^- \to \nu\bar{\nu}H$ events with $H \to b\bar{b}$. This method uses the large $Br(H \to b\bar{b})$ value to compensate the smaller cross section of the W fusion process σ_{vvH}. The combined precision of the two measurements is 3.3%.

7 Coupling and EFT Analyses

Use H instead of h for the Higgs boson to be consistent with the rest of the text?

7.1 Coupling fits

In order to extract the implications of the predicted measurement precision shown in Table 11 on possible new physics models, constraints on additional contributions to Higgs boson couplings are derived. The Standard Model makes specific predictions for the Higgs boson couplings to the SM fermions, $g(hff;\mathrm{SM})$, and to the SM gauge bosons $g(hVV;\mathrm{SM})$. [3] The deviation from the Standard Model couplings will be parametrized using:

$$\kappa_f = \frac{g(hff)}{g(hff;\mathrm{SM})}, \quad \kappa_V = \frac{g(hVV)}{g(hVV;\mathrm{SM})} \tag{7.1}$$

In addition to couplings which are present at tree level, the Standard Model also predicts effective couplings $h\gamma\gamma$ and hgg, in terms of other SM parameters. Changes can be induced by the possible shifts in the Higgs boson couplings described above. In addition, they can also be altered by loop contributions from new physics states. Hence, they will be introduced as two independent couplings, with their ratios to the SM predictions denoted as κ_γ and κ_g.

Furthermore, it is possible that the Higgs boson can decay directly into new physics particles. In this case, two type of new decay channels will be distinguished:

1. Invisible decay. This is a specific channel in which Higgs boson decay into invisible particles. This can be searched for and, if detected, measured.

2. Exotic decay. This includes all the other new physics channels. Whether they can be observed, and, if so, to what precision, depends sensitively on the particular final states. In one extreme, they can be very distinct and can be measured very well. In another extreme, they can be in a form which is completely swamped by the background. Whether postulating a precision for the measurement of the exotic decay or treating it as an independent parameter (essentially assuming it can not be measured directly) is an assumption one has to make. Results in both cases will be presented. In the later case, it is common to use the total width Γ_h as an equivalent free parameter.

In general, possible deviations of all Standard Model Higgs boson couplings should be considered. However, in the absence of obvious light new physics states with large couplings to the Higgs boson and other SM particles, a very large deviation ($> \mathcal{O}(1)$) is unlikely. In the case of smaller deviations, the Higgs boson phenomenology will not be sensitive to the deviations κ_e, κ_u, κ_d and κ_s. (are they important ever?) Therefore, they will not be considered here.

The CEPC will not be able to directly measure the Higgs boson coupling to top quarks. A deviation of this coupling from its SM value does enter $h\gamma\gamma$ and hgg amplitudes. However, this can be viewed as parametrized by κ_γ and κ_g already. Therefore, there will be no attempt to include κ_t as an independent parameter. In summary of the above discussions, the following set of 10 independent parameters is considered:

$$\kappa_b,\ \kappa_c,\ \kappa_\tau,\ \kappa_\mu,\ \kappa_Z,\ \kappa_W,\ \kappa_\gamma,\ \kappa_g,\ \mathrm{BR}_{\mathrm{inv}},\ \Gamma_h. \tag{7.2}$$

[3] For the discussion of coupling fits and their implications, "h'' is used to denoted the 125 GeV Higgs boson.

In this 10 parameter list, the relation $\Sigma_i \Gamma_i = \Gamma_h$ is used to replace the exotic decay branching ratio with the total width.

Several assumptions can be made that can lead to a reduced number of parameters (see also [37, 42]). For instance a 9 parameter fit can be defined assuming lepton universality:

$$\kappa_b,\ \kappa_c,\ \kappa_\tau = \kappa_\mu,\ \kappa_Z,\ \kappa_W,\ \kappa_\gamma,\ \kappa_g,\ \mathrm{BR}_{\mathrm{inv}},\ \Gamma_h. \tag{7.3}$$

This can be further reduced to 7 parameters, by assuming the absence of exotic and invisible decays (excluding $h \to ZZ \to \nu\nu\nu\nu$) [42, 43]:

$$\kappa_b,\ \kappa_c,\ \kappa_\tau = \kappa_\mu,\ \kappa_Z,\ \kappa_W,\ \kappa_\gamma,\ \kappa_g. \tag{7.4}$$

In addition to the previously mentioned assumptions, which reduce the number of parameters, there are also several classes of parameter space constraining assumptions, which can be combined in various ways with the former. These assumptions could also lead to possible extraction of coupling strengths from the LHC and enhancement of coupling precision projections for lepton colliders in a more model dependent manner. One such example is to assume $\kappa_W,\ \kappa_Z \leq 1$ [44, 45]. This assumption on the κ_V ratios is valid on a large class of Higgs sector extensions, including MSSM, 2HDM, NMSSM, etc. [36].

We remark here on the rational of considering a variety of fits with different assumptions. Different fits achieve different goals. In practice, the relative usefulness of them depends on the scenario and the goal. For example, in a specific and complete model, the Higgs boson couplings can be determined by a smaller number of more fundamental parameters. This leads to relations among the Higgs boson couplings. One can set the strongest limit by taking full advantage of these relations. Deviations produced by such an underlying model can be detected most sensitively in a such constrained fit. On the other extreme, model independent fit gives a model independent limit on the broadest possible model space. It helps to capture deviations that can be missed by a constrained fit. At the same time, it produces the weakest limits. In practice, it is likely something in between these two extremes that will be the most useful. As it was previously mentioned, there are many ways of imposing constraints. Even stronger ones than discussed above can be considered. However, the purpose of this note is not to access the reach in all possible models, which is an impossible task. We are aiming at giving an overall picture of the capability of the CEPC. Similar problems have been encountered in all previous studies of Higgs factories. A relatively common set of assumptions have been used as benchmarks, such as the ones discussed above. Therefore, for comparison purpose, we will focus on a 10-parameter model independent fit, and 7-parameter constrained fit recommended by the LHC Higgs cross section group [42].

The LHC and especially the HL-LHC will provide valuable and complementary information about the Higgs boson properties. For example, the LHC is capable of directly measuring the top Yukawa coupling through the tth process [46, 47]. In addition, the LHC could use differential cross sections to differentiate top-loop contributions and other heavy particle-loop contributions to the Higgs boson to gluon coupling [48–51], and similarly to separate contributions from different operators to the Higgs boson to vector boson couplings [52]. For the purpose of the coupling fit in our framework, the LHC with its large statistics, helps improving precision on rare processes such as Higgs boson to diphoton couplings. Note that a large portion of the systematics intrinsic to a hadron collider would be canceled by taking ratios of measured cross sections. For example, combining the ratio of the rates $pp \to h \to \gamma\gamma$ and $pp \to h \to ZZ^*$ and the measurement of hZZ coupling at the CEPC can significantly improve the measurement of κ_γ. These are the most useful inputs from the LHC to combine with the CEPC. Similar studies with the ILC can be found in Refs. [53–55].

Table 12. Coupling measurement precision in percent from the 7-parameter fit and 10-parameter fit described in the text for several benchmark integrated luminosity of the CEPC, and corresponding results after combination with the HL-LHC. All the numbers refer to are relative precision except for $\mathrm{BR}_{\mathrm{inv}}$ of beyond standard model for which 95% CL upper limit are quoted respectively. To leave some entries vacant for the 7-parameter fit to stress them being dependent parameter under the fitting assumptions of the 7-parameter.

	10-parameter fit		7-parameter fit	
	CEPC	+HL-LHC	CEPC	+HL-LHC
Γ_h	3.3	2.5	–	–
κ_b	1.6	1.2	1.5	1.2
κ_c	2.3	2.0	2.3	2.0
κ_g	1.6	1.2	1.6	1.2
κ_W	1.4	1.1	1.4	1.1
κ_τ	1.6	1.2	1.5	1.1
κ_Z	0.25	0.25	0.17	0.16
κ_γ	4.4	1.7	4.4	1.7
κ_μ	8.1	4.9	–	–
$\mathrm{BR}_{\mathrm{inv}}^{\mathrm{BSM}}$	0.31	0.31	–	–

The 10-parameter fit and the 7-parameter fit for several integrated luminosities are shown in Table 12, respectively. In addition, the combinations with expectations (with theoretical uncertainties included) from the HL-LHC from Ref. [56] are shown in the same tables as well.[4] We assume the HL-LHC will operate at 14 TeV center-of-mass energy and accumulate an integrated luminosity of 3000 fb^{-1}.

The CEPC Higgs boson properties measurements mark a giant step beyond the HL-LHC. First of all, in contrast to the LHC, a lepton collider Higgs factory is capable of measuring the absolute width and coupling strengths of the Higgs boson. A comparison with the HL-LHC is only possible with model dependent assumptions. One of such comparison is within the framework of a 7-parameter fit, shown in Fig. 21. Even with this set of restrictive assumptions, the advantage of the CEPC is still significant. The measurement of κ_Z is more than a factor of 10 better. The CEPC can also improve significantly on a set of channels which suffers from large background at the LHC, such as κ_b, κ_c, and κ_g. We

[4] We note here that the LHC and the CEPC have different sources of theoretical uncertainties, for detailed discussion, see Refs. [37, 43, 57–59].

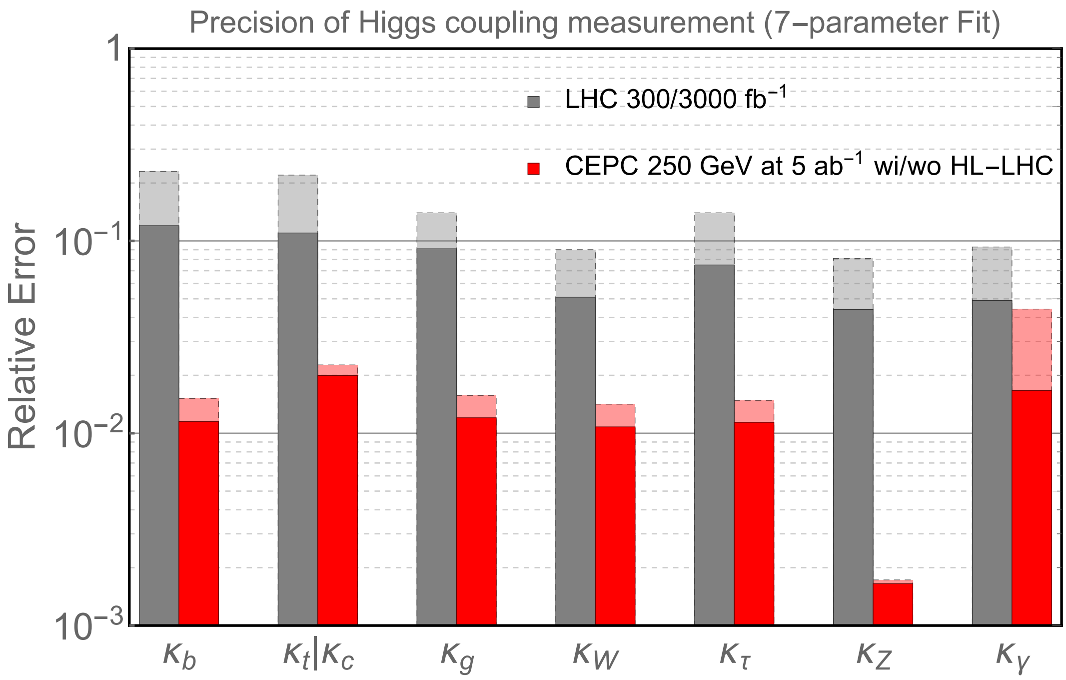

Figure 21. The 7 parameter fit result, and comparison with the HL-LHC [56]. The projections for the CEPC at 250 GeV with 5 ab^{-1} integrated luminosity are shown. The CEPC results without combination with the HL-LHC input are shown with dashed edges. The LHC projections for an integrated luminosity of 300 fb^{-1} are shown in dashed edges.

emphasize that this is comparing with the HL-LHC projection with aggressive assumptions about systematics. Such uncertainties are typically under much better control at lepton colliders. Within this 7 parameter set, the only coupling which the HL-LHC can give a competitive measurement is κ_γ, for which the CEPC's accuracy is limited by statistics. This is also the most valuable input that the HL-LHC can give to the Higgs boson coupling measurement at the CEPC, which underlines the importance of combining the results of these two facilities.

We also remark on the couplings which are left out in this fit. The most obvious omission is the $\mathrm{BR}_{\mathrm{inv}}$. The CEPC with 5 ab^{-1} can measure this to a high accuracy as 95% upper limit 0.24%, as shown in Table 12. At the same time, the HL-LHC can only manage a much lower accuracy $6-17\%$ [43].

As we have discussed above, one of the greatest advantages of lepton collider Higgs boson factory is the capability of determining the Higgs boson coupling *model independently*. The projection of such a determination at the CEPC is shown in Fig. 22. For comparison, we have also put in the projection from the combination the ILC 250 GeV and 500 GeV runs, based on the baseline designed luminosity. The advantage of the higher integrated luminosity at a circular lepton collider is apparent. The CEPC has a clear advantage in the measure of κ_Z. It is also much stronger in κ_μ and $\mathrm{BR}_{\mathrm{inv}}$ measurements.

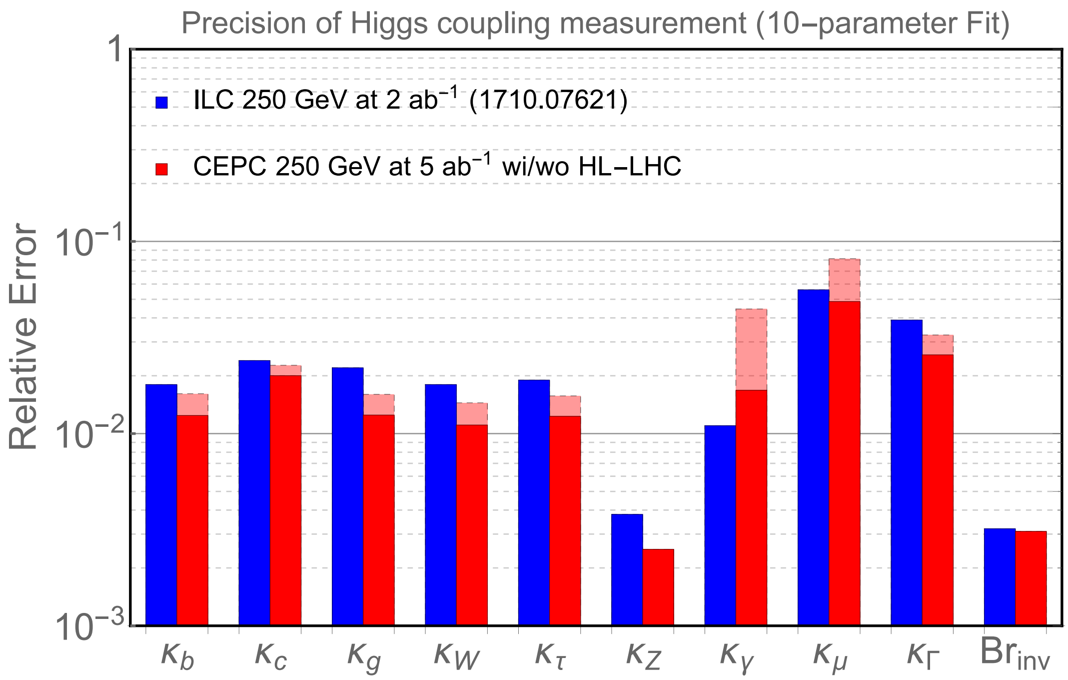

Figure 22. The 10 parameter fit result and comparison with the ILC [60]. The CEPC at 250 GeV with 5 ab^{-1} integrated luminosity and the ILC 250 with 2 fb^{-1} integrated luminosity are shown. The CEPC without combination with the HL-LHC input as shown in dashed edges. All the numbers refer to are relative precision except for $\mathrm{BR}_{\mathrm{inv}}$ for which 95% CL upper limit are quoted respectively.

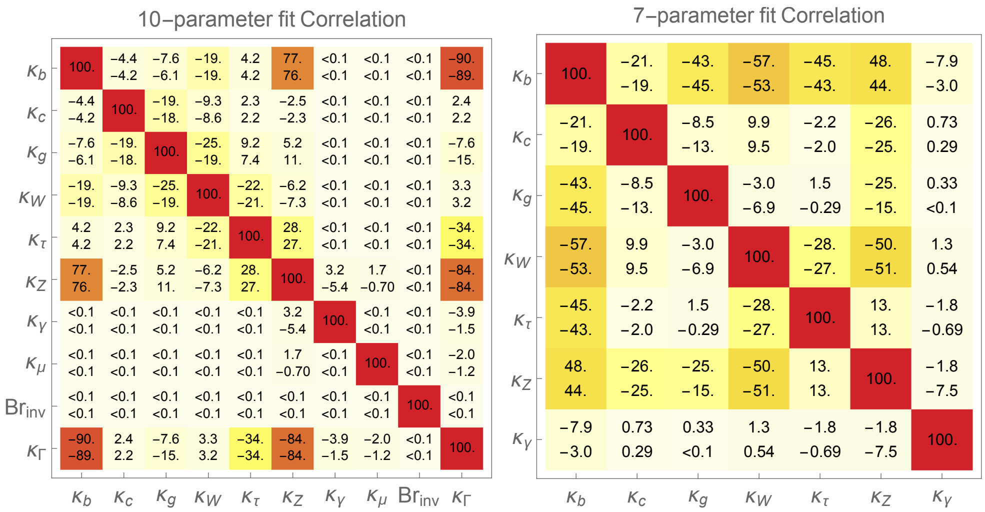

Figure 23. The correlation of the 10-parameter fit and 7-parameter fit shown the left and right panel, respectively. The upper (lower) number in each entry represent the CEPC (combined fit with HL-LHC) fit results. This is an orphan figure, no reference in the text.

7.2 Higgs boson self-coupling

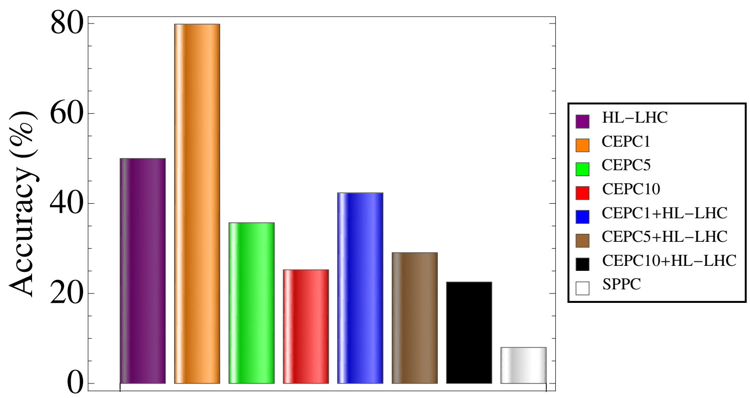

Figure 24. Higgs boson elf-coupling constraint inferred from the shift in hZZ coupling. The CEPC results refer to a luminosity of 1, 5 and 10 ab^{-1}. The combination with the HL-LHC assumes an integrated luminosity of 3 ab^{-1} and it is taken from Ref. [43].

Zhen: This section can be updated by Jiayin/Zhen and Lian-Tao group, as we all work on this topic for CEPC with quite a few updated results.

The Higgs boson self-coupling, $\lambda(hhh)$, is a critical parameter governing the dynamics of the electroweak symmetry breaking. It does not enter the CEPC phenomenology directly, but it affects the hZZ coupling at one-loop level. Therefore, a limit on κ_Z can be interpreted as a limit on $\kappa_{\lambda(hhh)}$ with some model assumptions [61]. Of course, other new physics can also alter κ_Z. Unless in the case of a cancellation, the limit on $\kappa_{\lambda(hhh)}$ should be regarded as a reasonable estimate. The result from such a constraint is summarized in Fig. 24.

7.3 Effective-field-theory analysis

It is also desirable to characterize the Higgs couplings in the effective-field-theory (EFT) framework, in which the Standard Model Lagrangian is supplemented by higher dimensional operators. Imposing baryon and lepton numbers conservations, all higher dimensional operators are of even dimension:

$$\mathcal{L}_{\rm EFT} = \mathcal{L}_{\rm SM} + \sum_i \frac{c_i^{(6)}}{\Lambda^2}\mathcal{O}_i^{(6)} + \sum_j \frac{c_j^{(8)}}{\Lambda^4}\mathcal{O}_j^{(8)} + \cdots \tag{7.5}$$

Assuming the scale of new physics Λ is sufficiently large, the leading effects of new physics at the electroweak scale can be well parameterized by the dimension-six operators. To obtain robust constraints on the Wilson coefficients c_i, a global analysis is required which includes the contributions from all possible dimension-six operators. While a large number of dimension-six operators can be written down, only a subset of them contribute to the Higgs processes at leading order. Among these operators, some are much better constrained by other measurements. It is thus reasonable to focus on the operators that primarily contributes to the Higgs processes and reduce the parameter space by making appropriate assumptions, as done in many recent studies of EFT global analysis at future lepton colliders [62–68]. Following these studies, we discard the CP-violating operators as well as the ones that induce fermion dipole interactions. At leading order, CP-violating operators do not have linear contributions to the rates of Higgs processes. While they do contribute to the angular observables at the leading order [69, 70], these operators are usually much better constrained by EDM experiments [71–73], though some rooms are still possible for the CP-violating couplings of Higgs to the heavy flavor quarks and leptons [74, 75]. The interference between the fermion dipole interactions with SM terms are suppressed by the fermion masses. The corresponding operators also generate dipole moments, which are stringently constrained especially for light fermions. For the operators that modify the Yukawa matrices, we focus on the five diagonal ones that correspond to the top, charm, bottom, tau, and muon Yukawa couplings, which are relevant for the Higgs measurements at CEPC.

The electroweak precision observables are already tightly constrained by the LEP Z-pole and W mass measurements. The CEPC Z-pole run can further improve the constraints set by LEP, thanks to the large mount of Z bosons that can be collected.The W mass can also be constrained within a few MeVs at CEPC even without a dedicated WW threshold run. Given that the expected precisions of the Z-pole observables and the W mass are much higher than the ones of Higgs observables, in the Higgs analysis we assume that the former ones are perfectly constrained, which greatly simplifies the analysis. In particular, in a convenient basis all the contact interaction terms of the form $hVf\bar{f}$ can be discarded since they also modify the fermion gauge couplings. Realistic Z-pole constraints have also been considered in recent studies [65, 66, 68], but certain assumptions (such as flavor-universality) and simplifications are made. Future studies with more general frameworks are desired to fully determine the impact of the Z-pole measurements on the Higgs analysis.

CEPC 250 GeV ($5\,\mathrm{ab}^{-1}$)				
	uncertainty	correlation matrix		
		$\delta g_{1,Z}$	$\delta\kappa_\gamma$	λ_Z
$\delta g_{1,Z}$	1.1×10^{-3}	1	0.03	-0.89
$\delta\kappa_\gamma$	0.8×10^{-3}		1	-0.40
λ_Z	1.2×10^{-3}			1

Table 13. The estimated constraints on aTGCs from the measurements of the diboson process ($e^+e^- \to WW$) in the semi-leptonic channel at CEPC 250 GeV with $5\,\mathrm{ab}^{-1}$ data and unpolarized beams. All angular distributions are used in the fit. We consider only the statistical uncertainties of the signal events assuming a selection efficiency of 80%.

The measurements of the triple gauge couplings (TGCs) from the diboson process ($e^+e^- \to WW$) play an important role in the Higgs coupling analysis under the EFT framework. Focusing on CP-even dimension-six operators, the modifications to the triple gauge vertices from new physics can be parameterized by three anomalous TGC parameters (aTGCs), conventionally denoted as $\delta g_{1,Z}$, $\delta\kappa_\gamma$ and λ_Z [76, 77]. Among them, $\delta g_{1,Z}$ and $\delta\kappa_\gamma$ are generated by operators that also contribute to the Higgs processes. At 250 GeV, the cross section of $e^+e^- \to WW$ is almost two orders of magnitude larger than the one of the Higgsstrahlung process. The measurements of the diboson process thus provide strong constraints on the operators that generate the aTGCs. A dedicated study on the TGC measurements at CEPC is not available at the current moment. We thus perform a simplified analysis to estimate the precision reaches on the aTGCs. Our results are shown in Table 13. The analysis roughly follows the methods in Refs. [64, 78]. We use only the WW events in the semi-leptonic (electron or muon) channel, which has good event reconstructions and also a sizable branching fraction ($\approx 29\%$). In particular, the production polar angle, as well as the two decay angles of the leptonic W, can be fully reconstructed, which contain important information on the aTGCs. The two decay angles of the hadronic W can only be reconstructed with a two-fold ambiguity. We perform a χ^2 fit of the 3 aTGC parameters to the binned distribution of all five angles and extract the one-sigma precision of the 3 aTGCs as well as the correlations among them. Without a detailed simulation study, we simply assume a signal selection efficiency of 80%, and do not consider the effects of systematics and backgrounds, assuming they are under control after the selection cuts. (Can remove the following if we don't want to direct compare with ILC.) Our results are comparable with the ones of ILC 250 GeV in Ref. [65], which agrees with our expectation since the lack of the longitudinal beam polarization at CEPC is compensated with a larger luminosity. We also note that in the TGC analysis at ILC 500 GeV [79], the selection efficiency of WW events in the semi-leptonic channel is around 70%, while the number of background events is much smaller than the signal one after all the selection cuts. While the center of mass energy and the beam polarizations are different, this nevertheless provides justifications to the assumptions we made in our analysis.

Under the assumptions specified above, the contributions to the Higgs and diboson processes from dimension-six operators consist of a total number of twelve degrees of free-

$\mathcal{O}_H = \frac{1}{2}(\partial_\mu \lvert H^2 \rvert)^2$	$\mathcal{O}_{GG} = g_s^2 \lvert H\rvert^2 G^A_{\mu\nu} G^{A,\mu\nu}$
$\mathcal{O}_{WW} = g^2 \lvert H\rvert^2 W^a_{\mu\nu} W^{a,\mu\nu}$	$\mathcal{O}_{y_u} = y_u \lvert H\rvert^2 \bar{Q}_L \tilde{H} u_R \quad (u \to t, c)$
$\mathcal{O}_{BB} = g'^2 \lvert H\rvert^2 B_{\mu\nu} B^{\mu\nu}$	$\mathcal{O}_{y_d} = y_d \lvert H\rvert^2 \bar{Q}_L H d_R \quad (d \to b)$
$\mathcal{O}_{HW} = ig(D^\mu H)^\dagger \sigma^a (D^\nu H) W^a_{\mu\nu}$	$\mathcal{O}_{y_e} = y_e \lvert H\rvert^2 \bar{L}_L H e_R \quad (e \to \tau, \mu)$
$\mathcal{O}_{HB} = ig'(D^\mu H)^\dagger (D^\nu H) B_{\mu\nu}$	$\mathcal{O}_{3W} = \frac{1}{3!} g \epsilon_{abc} W^{a\,\nu}_{\mu} W^b_{\nu\rho} W^{c\,\rho\mu}$

Table 14. A complete set of CP-even dimension-six operators that contribute to the Higgs and TGC measurements, assuming there is no correction to the Z-pole observables and the W mass, and also no fermion dipole interaction. For $\mathcal{O}_{y_u}$, $\mathcal{O}_{y_d}$ and $\mathcal{O}_{y_e}$, we only consider the contributions to the diagonal elements of the Yukawa matrices that corresponds to the top, charm, bottom, tau, and muon Yukawa couplings.

doms. While all non-redundant basis are equivalent, it is particularly convenient to choose a basis in which the twelve degrees of freedoms can be mapped to exactly twelve operators, while the rest are removed by the assumptions. We consider two such bases in our analysis, one is defined by the set of dimension-six operators in Table 14, the other is the so-called "Higgs basis," proposed in Ref. [80]. In the Higgs basis, the parameters are defined in the broken electroweak phase, and can be directly interpreted as the size of the Higgs couplings. Different from the original Higgs basis, we follow Ref. [64] and normalize the parameters associated with the hgg, $h\gamma\gamma$ and $hZ\gamma$ vertices to the SM one-loop contributions, and denote them as $\bar{c}_{gg}$, $\bar{c}_{\gamma\gamma}$ and $\bar{c}_{Z\gamma}$. We further define the parameter $\bar{c}^{\rm eff}_{gg}$ to absorb all contributions to the hgg vertex, as shown in Eq. 7.14. These redefined parameters can be more conveniently interpreted as the precisions of the Higgs couplings analogous to those in the κ framework. The exact definitions of the Higgs basis and the translation to the basis in Table 14 can be found in the end of the section.

The estimated precisions of all the Higgs rate measurements in Section 6 (Table 11), along with the correlations among them, are included as inputs for the EFT global analysis. In addition, we include the angular observables of the channel $e^+e^- \to hZ$, $Z \to \ell^+\ell^-$, $h \to b\bar{b}$, following the studies in Refs. [69, 70]. This channel is almost background free after the selection cuts, with a signal selection efficiency of about 40%. For the TGC measurements, we use the results in Table 13 as inputs. The global χ^2 is obtained by summing over the χ^2 of all the measurements. Due to the high precision of the measurements, it is shown that for all observables, keeping only the linear terms of all EFT parameters gives a very good approximation [64]. This greatly simplifies the fitting procedure, as the total χ^2 can be written as

$$\chi^2 = \sum_{ij} (c - c_0)_i \, \sigma^{-2}_{ij} \, (c - c_0)_j \, , \qquad \text{where} \quad \sigma^{-2}_{ij} \equiv (\delta c_i \, \rho_{ij} \, \delta c_j)^{-1} \, , \tag{7.6}$$

where c_i's are the EFT parameters, c_0's are the corresponding central values which are zero by construction, as we assume the measurements are SM-like. The one-sigma uncertainties δc_i and the correlation matrix ρ can be obtained from $\sigma^{-2}_{ij} = \partial^2 \chi^2 / \partial c_i \partial c_j$.

For comparison, we also consider the reaches of the LHC 14 TeV with a total luminosities of 300 fb^{-1} or 3000 fb^{-1}, which are combined with the diboson ($e^+e^- \to WW$)

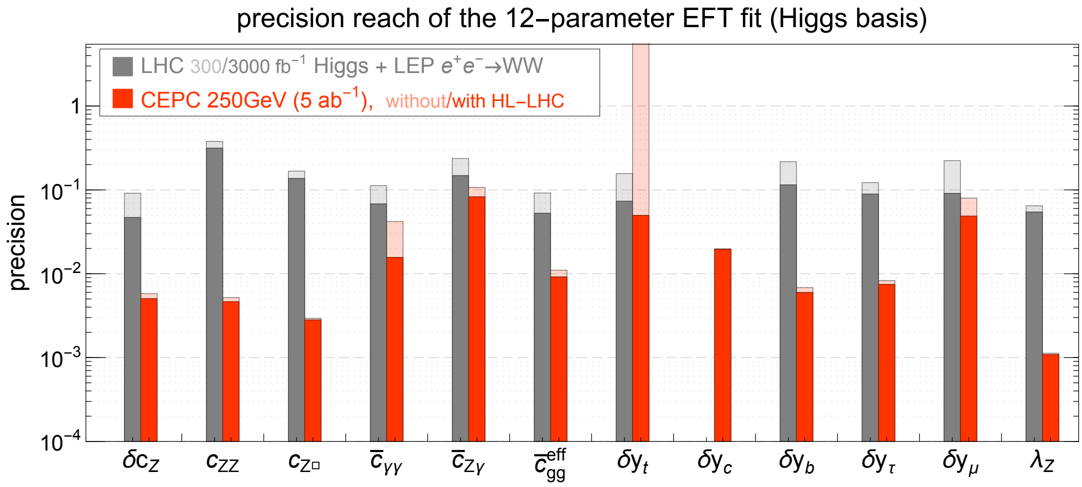

Figure 25. One-sigma precision reach of the twelve parameters in the Higgs basis. The first column shows the results from the LHC Higgs measurements with 300 fb^{-1} (light shade) and 3000 fb^{-1} (solid shade) combined with LEP diboson ($e^+e^- \to WW$) measurement. The second column shows the results from CEPC with 5 ab^{-1} data collected at 250 GeV with unpolarized beam. The results from CEPC alone are shown in light shades and the ones from a combination of CEPC and HL-LHC are shown in solid shades. The charm Yukawa is poorly constrained at the LHC and we simply fix δy_c to zero for the LHC fits.

measurements at LEP as well as the LHC 8 TeV Higgs measurements. For the LHC 14 TeV Higgs measurements, we use the projections by the ATLAS collaboration [56], while the composition of each channel are obtained from Refs. [81–85]. The constraints from the LHC 8 TeV Higgs measurements and the diboson measurements at LEP are obtained directly from Ref. [86]. While the LHC diboson measurements could potentially improve the constraints on aTGCs set by LEP [87], they are not included in our analysis due the potential issues related to the validity of the EFT [88, 89] and the TGC dominance assumption [90].

The results of the 12-parameter fit at CEPC are shown in Fig. 25 for the Higgs basis and Fig. 26 for the basis in Table 14. The results from LHC Higgs measurements (both 300 fb^{-1} and 3000 fb^{-1}) combined with LEP diboson measurements are shown in comparison. We also show the results of the combination of CEPC with HL-LHC (3000 fb^{-1}) in addition to the ones of CEPC alone. In Fig. 25, the results are shown in terms of the one-sigma precision of each parameter. The LHC results are shown with gray columns with 300 fb^{-1} (3000 fb^{-1}) in light (solid) shades, while the CEPC ones are shown with red column, with the CEPC-alone (combination with HL-LHC) results shown in light (solid) shades. In Fig. 26, the results are presented in terms of the reaches of $\Lambda/\sqrt{|c_i|}$ at 95% confidence level (CL), where Λ is the scale of new physics and c_i is the corresponding Wilson coefficient for each operator, defined in Eq. 7.5. Four columns are shown separately for LHC 300 fb^{-1}, LHC 3000 fb^{-1}, CEPC alone and CEPC combined with HL-LHC. The results of the global fits are shown with solid shades. The results from individual fits are shown with light shades, which are obtained by by switching on one operator at a time with the rest fixed to zero.

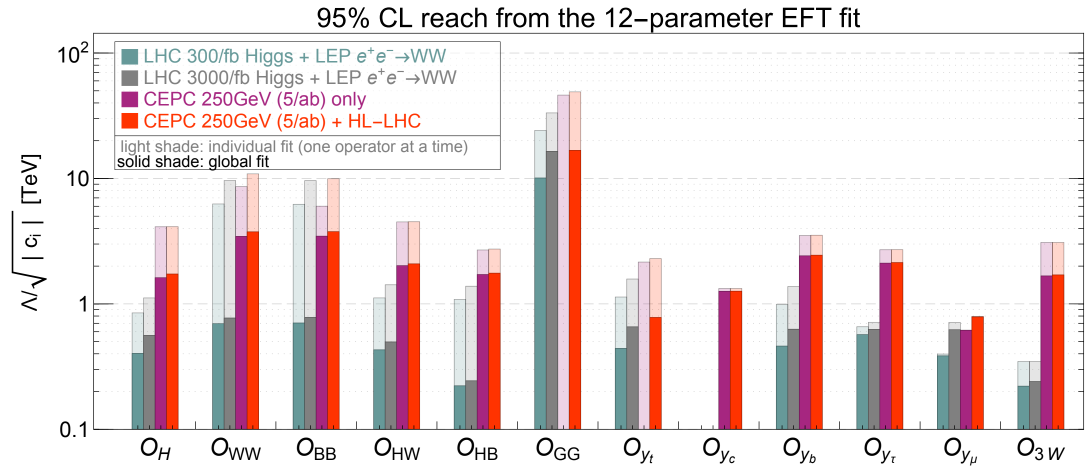

Figure 26. The 95% CL reach on $\Lambda/\sqrt{|c_i|}$ for the operators in the basis defined in Table 14. The first two columns show the results from LHC Higgs measurements with 300 fb^{-1} and 3000 fb^{-1} combined with LEP diboson ($e^+e^- \to WW$) measurement. The last two columns show the results from CEPC alone and the combination of CEPC and HL-LHC (3000 fb^{-1}). The results of the global fits are shown with solid shades. The results from individual fits (by switching on one operator at a time) are shown with light shades. The charm Yukawa is poorly constrained at the LHC and we simply fix δy_c to zero for the LHC fits.

It is transparent from Fig. 25 that CEPC provides very good reaches on the precisions of Higgs couplings, which are of one order of magnitude better than the ones at the LHC. For the parameters $\bar{c}_{\gamma\gamma}$, $\bar{c}_{Z\gamma}$ and δy_μ, the clean signal and small branching ratios of the corresponding channels ($h \to \gamma\gamma/Z\gamma/\mu\mu$) makes the HL-LHC precisions comparable with the CEPC ones. The combination with LHC measurements thus provides non-negligible improvements, especially for those parameters. It should be noted that, while δy_t modifies the hgg vertex via the top loop contribution, CEPC alone could not discriminate it from the hgg contact interaction ($\bar{c}_{gg}$ in Eq. 7.15) obtained from integrating out a heavy new particle in the loop. The parameter $\bar{c}^{\rm eff}_{gg}$ absorbs both contributions and reflects the overall precision of the hgg coupling. The combination with the LHC $t\bar{t}h$ measurements could resolve this flat direction. The CEPC measurements, in turn, could improve the constraint on δy_t set by the LHC by providing much better constraints on the other parameters that contribute to the $t\bar{t}h$ process. We also note that the measurement of the charm Yukawa coupling is not reported in Ref. [56], while the projection of its constraint has a large variation among different studies and can be much larger than one [91–96]. We therefore simply fix $\delta y_c = 0$ for the LHC-only fits, as treating δy_c as an unconstrained free parameter generates a flat direction in the fit which makes the overall reach much worse. The CEPC, on the other hand, provides very good measurements of the charm Yukawa and can constrain δy_c to a precision of $\sim 2\%$.

In terms of the reaches of $\Lambda/\sqrt{|c_i|}$ in Fig. 26, it is also clear that CEPC has a significantly better performance than the LHC. If the couplings are naïvely assumed to be of order one ($c_i \sim 1$), the Higgs measurements at CEPC would be sensitive to new physics

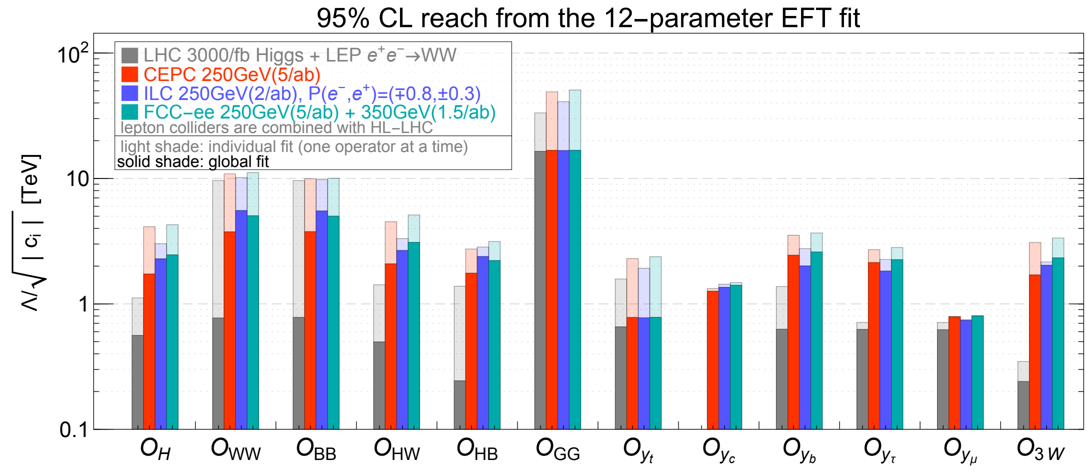

Figure 27. The 95% CL reach on $\Lambda/\sqrt{|c_i|}$ at the HL-LHC (combined with LEP diboson measurements), CEPC, ILC and FCC-ee for the operators in the basis defined in Table 14.

scales at multiple TeVs. While the individual reach for some of operators at the LHC can be comparable to the ones at CEPC (*e.g.*, O_{WW} and O_{BB} from the measurement of $h \to \gamma\gamma$), the reaches of CEPC are much more robust under a global framework thanks to its comprehensive measurements of both the inclusive hZ cross section and the exclusive rates of many Higgs decay channels. Operators O_{GG} and O_{y_t} both contribute to the hgg vertex. While the CEPC could provide strong constraints on either of them if the other is set to zero, they can only be constrained in a global fit if the $t\bar{t}h$ measurements at the LHC are also included. It is also important to note that the validity of EFT could be a potential issue for the LHC measurements [88]. Depending on the size of the couplings, the inferred bounds on the new physics scale Λ could be comparable with or even smaller than the energy scale probed by the LHC. The CEPC has a smaller center of mass energy and much better precisions, which ensures the validity of EFT for most new physics scenarios.

In Fig. 27, we compare the reach of the CEPC 250 GeV with the ones of ILC and FCC-ee. For ILC, we focus on the run at 250 GeV, the first stage of the staged plan proposed in recent documents [60]. We follow closely the scenario in Ref. [65], which assumes a total integrated luminosity of $2\,\text{ab}^{-1}$, equally shared by two configurations of longitudinal beam polarizations, $P(e^-, e^+) = (\mp 0.8, \pm 0.3)$. As pointed out in Refs. [64, 65], measuring the Higgsstrahlung process with different beam polarizations are particularly helpful in resolving the operators that modify the $hZ\gamma$ vertex, which contributes to the $e^+e^- \to hZ$ process via an s-channel photon. This is reflected in Fig. 27, as the sensitivities to individual operators at CEPC are generally better than the ones at ILC due to the larger luminosity, but ILC has better reaches for some of the operators under a global fit. For FCC-ee, we assume it can collect $5\,\text{ab}^{-1}$ data at 250 GeV and $1.5\,\text{ab}^{-1}$ at 350 GeV. [5] This scenario could also be considered as an upgraded CEPC with a 350 GeV run. While the primary

[5]Recent FCC-ee documents [97] suggest slightly different values of the energies (240 GeV and 365 GeV). We use 250 GeV and 350 GeV so that the measurement precision can be more easily extrapolated from other colliders.

physics goal of the 350 GeV run is to study the top quark, the Higgs measurements at 350 GeV could have a significant impact on the reach of the Higgs couplings in a global framework [64]. In addition to a better measurement of the WW fusion process of Higgs production, the 350 GeV also provides measurements of the Higgsstrahlung and diboson processes at a energy scale significantly larger than 250 GeV, which are very helpful in resolving the contributions of different operators. Indeed, as shown in Fig. 27, while the reach of individual operators are only marginally better at the FCC-ee compared with CEPC, the reaches in the global fit are significantly improved with the addition of the 350 GeV run. The enhancement to the Higgs program provided by the 350 GeV run should thus be taken into serious considerations for discussions of a potential upgrade of CEPC.

The "12-parameter" effective-field-theory framework

The Higgs basis is proposed in Ref. [80] and applied in EFT studies of the LHC Higgs measurements such as Refs. [86, 98]. While the SM and the dimension-six operators are included with gauge invariances imposed, the parameters in the Higgs basis are defined in the broken electroweak phase Lagrangian, which makes the connection to measurements more straightforward. We follow the framework in Ref. [64], which applies the Higgs basis to measurements at future lepton colliders. To simplify the analysis, the CP-violating operators and the ones that induce fermion dipole interactions are discarded, and the Z-pole observables and W mass are assumed to be SM-like.

The SM and dimension-6 operators relevant for our study are

$$\mathcal{L} \supset \mathcal{L}_{hVV} + \mathcal{L}_{hff} + \mathcal{L}_{\rm tgc} \,, \tag{7.7}$$

where the couplings of the Higgs to the SM gauge bosons are

$$\begin{aligned}\mathcal{L}_{hVV} = \frac{h}{v}\bigg[& (1+\delta c_W)\frac{g^2 v^2}{2} W^+_\mu W^{-\mu} + (1+\delta c_Z)\frac{(g^2+g'^2)v^2}{4} Z_\mu Z^\mu \\ & + c_{WW}\,\frac{g^2}{2} W^+_{\mu\nu}W^{-\mu\nu} + c_{W\Box}\, g^2 (W^-_\mu \partial_\nu W^{+\mu\nu} + \text{h.c.}) \\ & + c_{gg}\,\frac{g_s^2}{4} G^a_{\mu\nu} G^{a\,\mu\nu} + c_{\gamma\gamma}\,\frac{e^2}{4} A_{\mu\nu}A^{\mu\nu} + c_{Z\gamma}\,\frac{e\sqrt{g^2+g'^2}}{2} Z_{\mu\nu}A^{\mu\nu} \\ & + c_{ZZ}\,\frac{g^2+g'^2}{4} Z_{\mu\nu}Z^{\mu\nu} + c_{Z\Box}\, g^2 Z_\mu \partial_\nu Z^{\mu\nu} + c_{\gamma\Box}\, g g' Z_\mu \partial_\nu A^{\mu\nu} \bigg] \,.\end{aligned} \tag{7.8}$$

Not all the parameters in Eq. 7.8 are indepedent. Imposing gauge invariances, we choose to rewrite δc_W, c_{WW}, $c_{W\Box}$ and $c_{\gamma\Box}$ as[6]

$$\begin{aligned}\delta c_W &= \delta c_Z + 4\delta m \,, \\ c_{WW} &= c_{ZZ} + 2 s^2_{\theta_W} c_{Z\gamma} + s^4_{\theta_W} c_{\gamma\gamma} \,, \\ c_{W\Box} &= \frac{1}{g^2-g'^2}\left[g^2 c_{Z\Box} + g'^2 c_{ZZ} - e^2 s^2_{\theta_W} c_{\gamma\gamma} - (g^2-g'^2) s^2_{\theta_W} c_{Z\gamma}\right] \,, \\ c_{\gamma\Box} &= \frac{1}{g^2-g'^2}\left[2g^2 c_{Z\Box} + (g^2+g'^2) c_{ZZ} - e^2 c_{\gamma\gamma} - (g^2-g'^2) c_{Z\gamma}\right] \,,\end{aligned} \tag{7.9}$$

[6] In this subsection, s_{θ_W}, c_{θ_W} and t_{θ_W} are shorthands for $\sin\theta_W$, $\cos\theta_W$ and $\tan\theta_W$, where θ_W is the weak mixing angle.

where δm is induced by custodial symmetry breaking effects and is set to zero in our framework. While the modifications to the Yukawa couplings are in general 3×3 complex matrices in the family space, we focus on the diagonal ones of t, c, b, τ, μ which are relevant for the measurements,

$$\mathcal{L}_{hff} = -\frac{h}{v} \sum_{f=t,c,b,\tau,\mu} m_f(1+\delta y_f)\bar{f}_R f_L + \text{h.c.}\,. \tag{7.10}$$

The anomalous triple gauge couplings (aTGCs) are given by

$$\begin{aligned}
\mathcal{L}_{\text{tgc}} \;=\;\; & igs_{\theta_W} A^\mu(W^{-\nu}W^+_{\mu\nu} - W^{+\nu}W^-_{\mu\nu}) \\
& + ig(1+\delta g_1^Z)c_{\theta_W} Z^\mu(W^{-\nu}W^+_{\mu\nu} - W^{+\nu}W^-_{\mu\nu}) \\
& + ig\left[(1+\delta\kappa_Z)c_{\theta_W} Z^{\mu\nu} + (1+\delta\kappa_\gamma)s_{\theta_W} A^{\mu\nu}\right] W^-_\mu W^+_\nu \\
& + \frac{ig}{m_W^2}(\lambda_Z c_{\theta_W} Z^{\mu\nu} + \lambda_\gamma s_{\theta_W} A^{\mu\nu})W^{-\rho}_v W^+_{\rho\mu}\,,
\end{aligned} \tag{7.11}$$

where $V_{\mu\nu} \equiv \partial_\mu V_\nu - \partial_\nu V_\mu$ for $V = W^\pm, Z, A$. Gauge invariance further imposes $\delta\kappa_Z = \delta g_{1,Z} - t^2_{\theta_W}\delta\kappa_\gamma$ and $\lambda_Z = \lambda_\gamma$, thus leaving three independent aTGC parameters, which are chosen to be $\delta g_{1,Z}$, $\delta\kappa_\gamma$ and λ_Z. Two of them, $\delta g_{1,Z}$ and $\delta\kappa_\gamma$, are related to Higgs observables and can be written as

$$\begin{aligned}
\delta g_{1,Z} &= \frac{1}{2(g^2-g'^2)}\left[-g^2(g^2+g'^2)c_{Z\Box} - g'^2(g^2+g'^2)c_{ZZ} + e^2 g'^2 c_{\gamma\gamma} + g'^2(g^2-g'^2)c_{Z\gamma}\right]\,, \\
\delta\kappa_\gamma &= -\frac{g^2}{2}\left(c_{\gamma\gamma}\frac{e^2}{g^2+g'^2} + c_{Z\gamma}\frac{g^2-g'^2}{g^2+g'^2} - c_{ZZ}\right)\,.
\end{aligned} \tag{7.12}$$

In the Higgs basis, we therefore have the following 12 parameters:

$$\delta c_Z\,,\quad c_{ZZ}\,,\quad c_{Z\Box}\,,\quad c_{\gamma\gamma}\,,\quad c_{Z\gamma}\,,\quad c_{gg}\,,\quad \delta y_t\,,\quad \delta y_c\,,\quad \delta y_b\,,\quad \delta y_\tau\,,\quad \delta y_\mu\,,\quad \lambda_Z\,. \tag{7.13}$$

A full list of the relevant observables in terms of the 12 EFT parameters can be found in Ref. [64]. In particular, for the EFT parameters we consider only their tree level contributions, except for the hgg vertex for which we also include the contributions of δy_t and δy_b via the fermion loops. We also follow Ref. [64] and normalize $c_{\gamma\gamma}$, $c_{Z\gamma}$ and c_{gg} with respect to the SM 1-loop contributions to the $h\gamma\gamma$, $hZ\gamma$ and hgg vertices. The corresponding parameters are denoted by $\bar{c}_{\gamma\gamma}$, $\bar{c}_{Z\gamma}$ and $\bar{c}_{gg}$, defined as

$$\frac{\Gamma_{\gamma\gamma}}{\Gamma^{\text{SM}}_{\gamma\gamma}} \simeq 1 - 2\bar{c}_{\gamma\gamma}\,, \qquad \frac{\Gamma_{Z\gamma}}{\Gamma^{\text{SM}}_{Z\gamma}} \simeq 1 - 2\bar{c}_{Z\gamma}\,, \tag{7.14}$$

and

$$\frac{\Gamma_{gg}}{\Gamma^{\text{SM}}_{gg}} \;\simeq\; 1 + 2\,\bar{c}^{\,\text{eff}}_{gg} \;\simeq\; 1 + 2\,\bar{c}_{gg} + 2.10\,\delta y_t - 0.10\,\delta y_b\,. \tag{7.15}$$

They are related to the original parameters by

$$\bar{c}_{\gamma\gamma} \simeq \frac{c_{\gamma\gamma}}{8.3\times 10^{-2}}\,, \qquad \bar{c}_{Z\gamma} \simeq \frac{c_{Z\gamma}}{5.9\times 10^{-2}}\,, \qquad \bar{c}_{gg} \simeq \frac{c_{gg}}{8.3\times 10^{-3}}\,. \tag{7.16}$$

It should be noted that, without the inclusion of LHC $t\bar{t}h$ measurements, the CEPC measurements alone could only constrain a linear combination of c_{gg} and δy_t. In this case, the two parameters can be replaced by $\bar{c}_{gg}^{\rm eff}$ (defined in Eq. 7.15) which parametrize the total contribution to the hgg vertex.

To translate to the basis in Table 14, we first choose a different normalization of the Wilson coefficients, defined as

$$\begin{aligned}\mathcal{L}_{\rm D6} = & \frac{c_H}{v^2}\mathcal{O}_H + \frac{\kappa_{WW}}{m_W^2}\mathcal{O}_{WW} + \frac{\kappa_{BB}}{m_W^2}\mathcal{O}_{BB} + \frac{\kappa_{HW}}{m_W^2}\mathcal{O}_{HW} + \frac{\kappa_{HB}}{m_W^2}\mathcal{O}_{HB} \\ & + \frac{\kappa_{GG}}{m_W^2}\mathcal{O}_{GG} + \frac{\kappa_{3W}}{m_W^2}\mathcal{O}_{3W} + \sum_{f=t,c,b,\tau,\mu}\frac{c_{y_f}}{v^2}\mathcal{O}_{y_f}\,,\end{aligned} \tag{7.17}$$

in order to simplify the expressions. In this basis, the aTGCs are given by

$$\begin{aligned}\delta g_{1,Z} = & -\frac{\kappa_{HW}}{c_{\theta_W}^2}\,, \\ \delta\kappa_\gamma = & -\kappa_{HW} - \kappa_{HB}\,, \\ \lambda_Z = & -\kappa_{3W}\,,\end{aligned} \tag{7.18}$$

The translation between the two bases is straightforward, given by

$$\begin{aligned}\delta c_Z = & -\frac{1}{2}c_H\,, \\ c_{ZZ} = & \frac{4}{g^2+g'^2}(-\kappa_{HW} - t_{\theta_W}^2\kappa_{HB} + 4\,c_{\theta_W}^2\kappa_{WW} + 4\,t_{\theta_W}^2 s_{\theta_W}^2\kappa_{BB})\,, \\ c_{Z\Box} = & \frac{2}{g^2}(\kappa_{HW} + t_{\theta_W}^2\kappa_{HB})\,, \\ c_{\gamma\gamma} = & \frac{16}{g^2}(\kappa_{WW} + \kappa_{BB})\,, \\ c_{Z\gamma} = & \frac{2}{g^2}(\kappa_{HB} - \kappa_{HW} + 8\,c_{\theta_W}^2\kappa_{WW} - 8\,s_{\theta_W}^2\kappa_{BB})\,, \\ c_{gg} = & \frac{16}{g^2}\,\kappa_{GG}\,, \\ \delta y_f = & -\frac{1}{2}c_H - c_{y_f}\,.\end{aligned} \tag{7.19}$$

It should be noted that Eq. 7.18 and Eq. 7.19 are only valid under the assumptions made in our analysis, more specifically, that there is no correction to the Z-pole observables and the W mass. The general expressions for the aTGCs can be found in Ref. [99]. Basis translations from the Higgs basis to the SILH' basis (and others) are provided in Ref. [80]. To go from the SILH' basis to the one in Table 14, one simply trades $\mathcal{O}_W\,, \mathcal{O}_B$ for $\mathcal{O}_{WW}\,, \mathcal{O}_{WB}$, using

$$\begin{aligned}\mathcal{O}_B = & \mathcal{O}_{HB} + \frac{1}{4}\mathcal{O}_{BB} + \frac{1}{4}\mathcal{O}_{WB}\,, \\ \mathcal{O}_W = & \mathcal{O}_{HW} + \frac{1}{4}\mathcal{O}_{WW} + \frac{1}{4}\mathcal{O}_{WB}\,,\end{aligned} \tag{7.20}$$

where $\mathcal{O}_{WB}$ is directly related to the Z-pole measurements and is discarded in our analysis.

Numerical results of the global fit

In Table 15, we present for CEPC the numerical results of the global fit in terms of the one-sigma precisions of the 12 parameters and the correlations among them. The results assume an integrated luminosity of $5\,\mathrm{ab}^{-1}$ at 250 GeV with unpolarized beams, with the combination of HL-LHC ($3000\,\mathrm{fb}^{-1}$) Higgs measurements. With both the one-sigma bounds and the correlation matrix, the corresponding *chi-squared* can be reconstructed, which can be used to derive the constraints in any other EFT basis, or any particular model that can be matched to the EFT. This offers a convenient way to study the reaches on new physics models, as detailed knowledges of the experimental measurements are not required.

CEPC 250 GeV, $5\,\mathrm{ab}^{-1}$ + HL-LHC													
	one-sigma uncertainty	correlation matrix											
		δc_Z	c_{ZZ}	$c_{Z\Box}$	$c_{\gamma\gamma}$	$c_{Z\gamma}$	c_{gg}	δy_t	δy_c	δy_b	δy_τ	δy_μ	λ_Z
δc_Z	0.0080	1	-0.15	-0.62	-0.14	-0.08	0.021	0.071	0.36	0.76	0.67	0.068	-0.52
c_{ZZ}	0.0094		1	-0.68	0.083	0.25	-0.027	-0.0066	-0.12	-0.29	-0.24	-0.029	-0.73
$c_{Z\Box}$	0.0055			1	0.042	-0.12	0.0046	-0.05	-0.17	-0.36	-0.33	-0.029	0.97
$c_{\gamma\gamma}$	0.0013				1	0.029	-0.16	0.18	-0.10	-0.10	-0.083	-0.057	0.028
$c_{Z\gamma}$	0.0050					1	-0.012	-0.0098	-0.079	-0.17	-0.15	-0.015	-0.096
c_{gg}	0.00043						1	-0.98	0.0088	0.041	0.038	0.18	0.007
δy_t	0.050							1	0.051	0.11	0.099	-0.18	-0.042
δy_c	0.020								1	0.50	0.43	0.045	-0.13
δy_b	0.0075									1	0.88	0.064	-0.28
δy_τ	0.0089										1	0.056	-0.26
δy_μ	0.049											1	-0.022
λ_Z	0.0023												1

Table 15. The one-sigma uncertainties and the correlation matrix for the 12 parameters in the Higgs basis from CEPC (250 GeV, $5\,\mathrm{ab}^{-1}$), with the combination of HL-LHC ($3000\,\mathrm{fb}^{-1}$) Higgs measurements.

8 Constraining anomalous HVV interactions at the CEPC collider

8.1 Introduction to HVV anomalous couplings

In this section, we study the extent to which *CP* parity of a Higgs boson, and more generally its anomalous couplings to gauge bosons, can be measured at the CEPC collider based on the dominant Higgs production and decay process $e^+e^-(\to Z^*) \to ZH \to \mu^+\mu^-b\bar{b}$. Full description of this analysis can be found in Ref. [100]. In this process, one of the Z-boson is offshell where q^2 is equal to the collision energy. This feature, as detailed in Ref. [100], plays an important role in comparing the sensitivities with the LHC experiments.

Studies of spin, parity, and couplings of a Higgs boson employ generic parameterisations of scattering amplitudes. Such parameterisations contain all possible tensor structures consistent with assumed symmetries and Lorentz invariance. We follow the notation of Refs. [100–102] and write the general scattering amplitude that describes interactions of a spin-zero boson with the gauge bosons, such as ZZ,

$$A(X_{J=0} \to VV) = \frac{1}{v}\left(g_1 m_V^2 \epsilon_1^* \epsilon_2^* + g_2 f_{\mu\nu}^{*(1)} f^{*(2),\mu\nu} + g_4 f_{\mu\nu}^{*(1)} \tilde{f}^{*(2),\mu\nu}\right) . \tag{8.1}$$

In Eq. (8.1), $f^{(i),\mu\nu} = \epsilon_i^\mu q_i^\nu - \epsilon_i^\nu q_i^\mu$ is the field strength tensor of a gauge boson with momentum q_i and polarisation vector ϵ_i; $\tilde{f}^{(i),\mu\nu} = 1/2\epsilon^{\mu\nu\alpha\beta} f_{\alpha\beta}$ is the conjugate field strength tensor. Parity-conserving interactions of a scalar (pseudo-scalar) are parameterised by the couplings $g_{1,2}(g_4)$, respectively. In the Standard Model (SM), the only non-vanishing $H \to ZZ$ coupling is at tree-level is $g_1 = 2i$, while g_2 is generated through radiative corrections. In this study, we focus on the determination of anomalous couplings of the predominantly $J^{CP} = 0^{++}$ Higgs-like boson to SM gauge bosons since existing experimental data already disfavours other exotic spin-parity assignments [3, 4, 103, 103–107]. We therefore assume that the coupling constants satisfy a hierarchical relation $g_1 \gg g_{2,4}$ and that non-standard couplings *always* provide small modifications of the SM contributions.

It is convenient to express the results of the measurement of the anomalous couplings in terms of physical quantities. Five independent numbers are needed to parameterise the couplings since one overall complex phase is not measurable. We take one of these numbers to be the $H \to VV$ interaction rate; the remaining four real numbers parameterise ratios of couplings and their relative phases. We find it convenient to use effective fractions of events defined as

$$f_{gi} = \frac{|g_i|^2\sigma_i}{|g_1|^2\sigma_1 + |g_2|^2\sigma_2 + |g_4|^2\sigma_4}, \tag{8.2}$$

to parameterise coupling ratios. The phases are defined as $\phi_{gi} = \arg(g_i/g_1)$. The advantage of introducing fractions f_{gi} is that, for fixed tensorial structure of the HVV vertex, they are invariant under independent re-scalings of all couplings. The parameter f_{g4} is particularly of interest as it is the fraction of a *CP*-odd contribution to the total production cross section of a Higgs boson with the assumption $g_2 = 0$. For the ease of comparison with CMS studies, we will use f_{a2} and f_{a3} instead of f_{g2} and f_{g4}, respectively. To compare with the sensitivities in other experiments with different $m^2_{Z^*}$, such as the $H \to ZZ \to 4\ell$ decay in the LHC experiments where m_{Z^*} is significantly less than the value in the $Z^* \to ZH$ at the CEPC collider, we also define f_{a2}^{dec} and f_{a3}^{dec} values correspond to cross sections defined in decay $H \to VV$.

8.2 Kinematics in the $e^+e^- \to Z^* \to ZH$ process

At the e^+e^- collider, three types of observables can be used to measure tensor couplings of the Higgs bosons.

1. Cross sections, especially their dependences on virtualities of weak bosons [108–110], as shown in Figure 28 for the $e^+e^- \to Z^* \to ZH$ process. The threshold behaviour for $\sqrt{s} < 250$ GeV of the cross sections $e^+e^- \to Z^* \to XZ$ has been suggested as a useful observable to determine the spin of the new boson [111]. Similarly, in a mixed *CP*-case, the dependence of $e^+e^- \to ZH$ cross section on the energy of the collision will differ from a pure $J^{CP} = 0^{++}$ case as seen in Figure 28. Therefore, a measurement of the cross section at several different energies will give us useful information about anomalous HVV couplings. However this feature is not included in this study as we assume a single value of the collision energy for the Higgs boson productions at the CEPC collider.

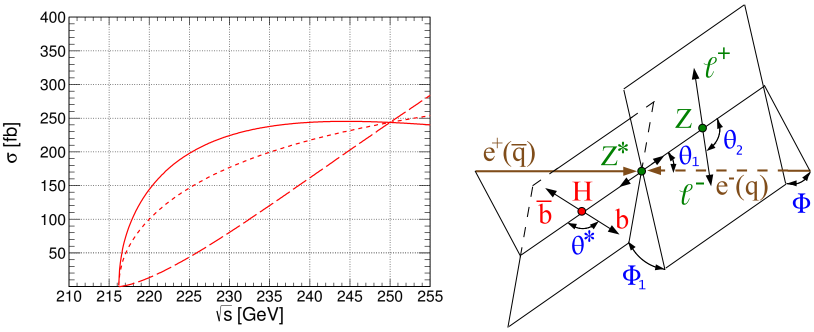

Figure 28. Left: Cross sections for $e^+e^- \to Z^* \to ZX$ process as a function of $\sqrt{s}$ for three models: SM Higgs boson (0^+, solid), scalar with higher-dimension operators (0_h^+, short-dashed), and pseudoscalar (0^-, long-dashed). All cross sections are normalised to SM value at $\sqrt{s} = 250$ GeV. Right: Higgs production and decay at the e^+e^- or pp collider with $e^+e^-(q\bar{q}) \to Z^* \to ZH \to \ell^+\ell^- b\bar{b}$ as shown in the parton collision frame. Right:

2. Angular distributions for the angles defined in Figure 28. Examples of such distributions with different $H \to VV$ couplings are shown in Figure 29, where numeric simulation is compared with analytical predictions as in Ref [100].

3. Angular distributions or other observables that are sensitive to interference between CP-even and CP-odd couplings. Examples include forward-backward asymmetry with respect to $\cos\theta_1$ or $\cos\theta_2$ and non-trivial phase in the Φ distributions shown in Figure 29. Such asymmetries require undefined CP to appear; as the result, CP violation would follow as an unambiguous interpretation e.g. once the forward-backward asymmetry is observed.

To get the most optimal sensitivity, it is important to employ all available observables described above and not limit oneself to CP-specific ones, such as inferences.

8.3 Expected signal and backgrounds

Productions and decays of the Higgs bosons at the CEPC collider are simulated with the JHU generator [101, 102], a dedicated Monte Carlo program, that incorporates all the anomalous couplings, spin correlations, interference of all contributing amplitudes.

The number of signal events are calculated using SM Higgs boson cross sections and branching fractions from Ref. [37]. We assume only small contributions of anomalous couplings which would not change this number significantly. The cross section ratios for the g_2 and g_4 terms where $g_1 = 0, g_{4(2)} = 1$ compared to the SM contribution where $g_1 = 0, g_2 = g_4 = 0$ are calculated with the JHU generator to be $\sigma_{4(2)}/sigma_1 = 8.07(34.1)$. We apply simple acceptance selections on the two muons $p_T(\mu) > 5$ GeV, $\eta(\mu) < 2.4$. As the angular variables do not rely on the Higgs boson decay products, there is no selection on the b jets. After acceptance selections, the number of signal events is estimated to be 8 events per fb^{-1}. The effective number of background events is estimated to be 10% of the number of signal events and is modelled with the $e^+e^- \to ZZ \to \ell^+\ell^- b\bar{b}$ process in Madgraph.

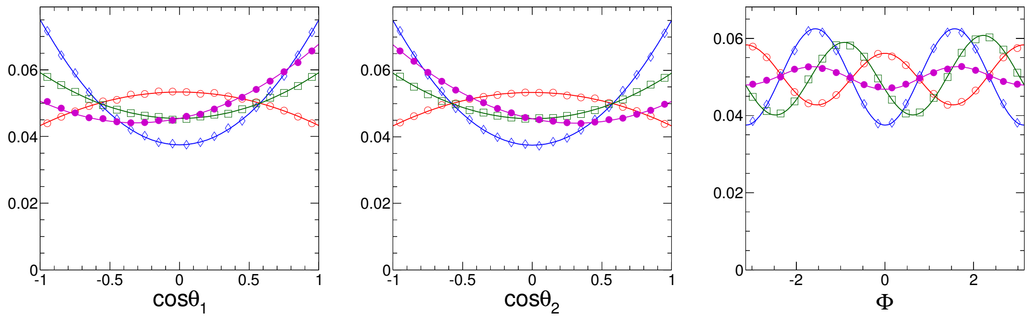

Figure 29. Distributions of the observables in the $e^+e^- \to ZH \to (\ell^+\ell^-)H$ analysis at $\sqrt{s} =$ 250 GeV, from left to right: $\cos\theta_1$, $\cos\theta_2$, and Φ. Points show simulated events and lines show projections of analytical distributions. Four scenarios are shown: SM scalar (0^+, red open circles), pseudoscalar (0^-, blue diamonds), and two mixed states corresponding to $f_{a3} = 0.5$ with $\phi_{a3} = 0$ (green squares) and $\pi/2$ (magenta points). In all cases we choose $f_{a2} = 0$.

8.4 Analysis methods

The $H \to ZZ$ anomalous couplings can be measured by performing a multi-dimensional fit to match observed kinematic distributions in various processes to theory predictions. Theoretical input to the fit involves real parameters such as for example $\vec{\zeta} = \{f_{a2}, \phi_{a2}, f_{a3}, \phi_{a3}, ...\}$ in Eq. (8.2) which, once known, can be used to derive the couplings. To set up a fit process, we follow Ref. [101] and introduce the likelihood function for N candidate events

$$\mathcal{L} = \exp\left(-n_{\text{sig}} - n_{\text{bkg}}\right) \prod_i^N \left(n_{\text{sig}} \times \mathcal{P}_{\text{sig}}(\vec{x}_i;\ \vec{\zeta}) + n_{\text{bkg}} \times \mathcal{P}_{\text{bkg}}(\vec{x}_i)\right) , \tag{8.3}$$

where n_{sig} is the number of signal events, n_{bkg} is the number of background events, and $\mathcal{P}(\vec{x}_i; \vec{\zeta})$ is the probability density function for signal or background. Each candidate event i is characterised by a set of kinematic observables such as $\vec{x}_i = \{\vec{\Omega}\}_i$ as defined in Fig. 28 or matrix element likelihood ratios D_{0^-} and D_{CP} as in Ref [100]. The number of observables and free parameters can be extended or reduced, depending on the desired fit. In this analysis we explore the full three-dimensional fit based on the analytical predictions that have been validated using simulation. The background probability density function is modelled from simulation.

The non-uniform reconstruction efficiency are modelled with the acceptance function $\mathcal{G}$ which enters the $\mathcal{P}_{\text{sig}}$ characterisation and is given by the step-function

$$\mathcal{G}(m_1, m_2, \vec{\Omega}) = \prod_\ell \theta(|\eta_{\max}| - |\eta_\ell(m_1, m_2, \vec{\Omega})|) ,$$

where $\eta_\ell = \ln\cot(\theta_\ell/2)$ is the pseudorapidity of a lepton and $|\eta_{\max}|$ is the maximal pseudorapidity in reconstruction. We also assume that the detection efficiency does not change within the detector acceptance, otherwise $\mathcal{G}$ is multiplied by the non-uniform function.

Several thousand statistically-independent experiments are generated and fitted to estimate the sensitivity to f_{a2} and f_{a3}, defined as the smallest values that can be measured

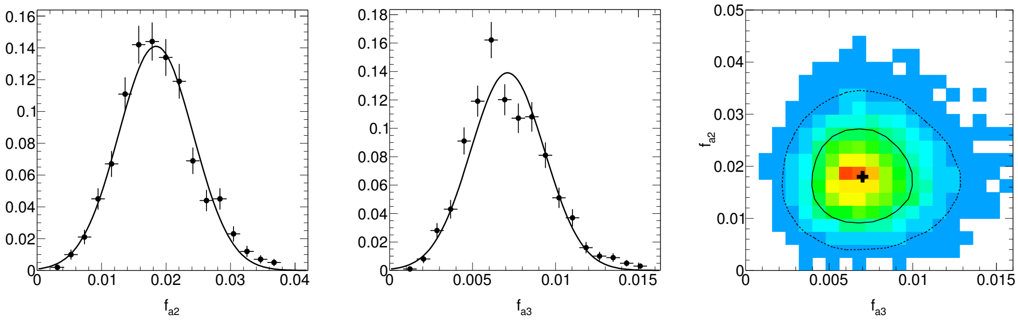

Figure 30. Distribution of fitted values of f_{a2} and f_{a3} in a large number of generated experiments. In the left and middle plots, only the parameter shown is floated. Other parameters are fixed to SM expectations. Right plot: simultaneous fit of non-zero f_{a2} and f_{a3}, with 68% and 95% confidence level contours shown.

with 3σ away from 0. We then convert these values in terms of the parameters $f^{\rm dec}_{a2,a3}$ to compare with the sensitivities from other experiments. Figure 30 shows precision on f_{a2} and f_{a3} obtained with generated experiments. As can be seen there, the expected sensitivity for f_{a3} is 0.007, which translates to very different constraints on $f^{\rm dec}_{a3}$ of 1.3×10^{-4}. This is because the $m^2_{Z^*}$ in the $Z^* \to ZH$ process at the CEPC collider is much higher than the value in $H \to ZZ^*$ decays, leading to much larger cross-section ratio σ_4/σ_1. And therefore measuring a similar fraction of events caused by the pseudoscalar anomalous couplings at higher $m^2_{Z^*}$ value means a sensitivity to a smaller value of g_4. Similarly the expected sensitivity for f_{a2} is 0.018, which translates to very different sensitivity for $f^{\rm dec}_{a2}$ of 2×10^{-4} for the same consideration as in the f_{a3}. We also confirm that precision on f_{a3} does not change significantly if ϕ_{a3} is either floated or kept fixed provided that the measured value of f_{a3} is at least 3σ away from zero. A simultaneous fit of f_{a2} and f_{a3} can also performed with the 68% and 95% confidence level contours shown in Figure 30.

8.5 Summary and Conclusions

The expected sensitivity to the anomalous couplings in the $Z^* \to ZH$ process has been estimated the CEPC collider, assuming $5{\rm ab}^{-1}$ at $\sqrt{s} = 250$ GeV. The $f^{\rm dec}_{a3}$ parameter, also refereed to as f_{CP}, is defined as the *CP*-odd cross section fraction in the $H \to ZZ$ decays is of particular interest. In the presence of new physics continuations from pseudoscalars, values as small as $f_{CP} \sim 1.3 \times 10^{-4}$ in can be discovered at 3σ level at the CEPC collider, a factor of 3 smaller compared to the ultimate sensitivity from HL-LHC experiments as shown in Ref [100]. Higher order corrections or in the presence of new physics contributions, values as small as $f^{\rm dec}_{a2} \sim 2 \times 10^{-4}$ can be measured at 3σ level, a factor of 300 better than the current best estimate using the $H \to ZZ \to 4\ell$ decays in the HL-LHC experiments.

Note that in this analysis, signal kinematics can be reconstructed inclusively by tagging $Z \to \ell^+\ell^-$ decay and using energy-momentum constraints. The $H \to b\bar{b}$ decays are only used to estimate the number of signal and background events. Further improvements can be achieved by exploring kinematics in the $H \to b\bar{b}$ decays, considering other Z decay final states, and combining with the overall cross-section dependence of the signal with a threshold scan in $\sqrt{s}$.

9 Implications

In this section, we briefly discuss the most important physics implications of the Higgs boson property measurements at the CEPC. In the past couple of decades, many models and scenarios of new physics beyond the Standard Model (BSM) have been proposed. A central theme of these studies is addressing the question of electroweak symmetry breaking. In those models, the Higgs boson couplings to the SM particles are typically modified, either by new particles propagating in the loop, or by mixture of the SM-like Higgs boson with other states. Therefore, the CEPC, with its significant improvement on the sensitivity to the deviations in the Higgs boson couplings from their SM predictions, will offer an excellent opportunity to probe a wide variety of BSM scenarios. Instead of giving an exhaustive account, we will highlight a couple of important cases. The choices of the topics here are guided by the crucial questions about EWSB we would like to address.

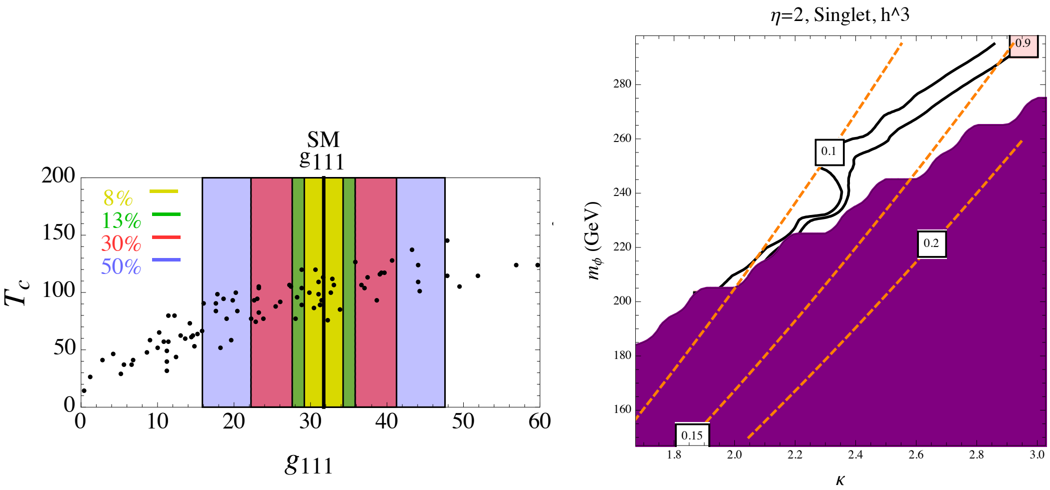

(a) (b)

Figure 31. Higgs boson self-coupling deviation and first order electroweak phase transition. (a) A generic singlet model. Black dots are points where the phase transition is of first order. g_{111} is the triple Higgs boson coupling [112]. (b) A singlet model with a Z_2 symmetry [113]. Orange dashed lines are contours of fractional deviation. The region within the thick black curves has first order electroweak phase transition. n the shaded region, phase transition into a wrong vacuum.

9.1 Electroweak phase transition

Since its discovery, the image of a SM-like Higgs boson has gradually emerged from the suite of LHC measurements. At the same time, the nature of the electroweak phase transition remains unknown. Uncovering this mystery is crucial since it has important consequences on the early universe cosmology and thus the understanding of our observable world. With the assumption of a minimal Higgs potential and the Higgs sector of the SM, it is well known that the phase transition is not of first order. However, this conclusion can be easily modified by new physics with sizable couplings to the Higgs boson. Many such examples have been proposed. All of them predict deviations in the Higgs boson couplings from the Standard Model prediction. The CEPC has the capability of probing these models and revealing the nature of the electroweak phase transition. Instead of a comprehensive survey, we will focus here on some of the simplest possibilities which are also difficult to probe. The minimal model that has been well studied in this class is to introduce an additional singlet which couples to the Higgs boson [112–117]. Generically, if the electroweak phase transition is of first order, we expect a significant deviation in the triple Higgs boson coupling. This is shown in the left panel of Fig. 31, where the deviation can vary as much as ∼100%. A more restricted scenario, in which a discrete Z_2 symmetry is imposed on the singlet, has also been considered [113, 117]. A first order electroweak phase transition is significantly harder in this scenario. It requires stronger couplings between the Higgs boson and the singlet, which is limited at least by perturbativity. In this case, the expected loop induced deviation in the triple Higgs boson coupling is generically smaller, about $10 - 15\%$, as shown in the right panel of Fig. 31. From the projections of the accuracy of Higgs boson self-coupling measurement shown in Fig. 24, the CEPC has excellent reach in the more general case. For the case with Z_2 symmetry, SPPC will be needed to make a more decisive determination based on the self coupling measurement and direct production of the additional singlet.

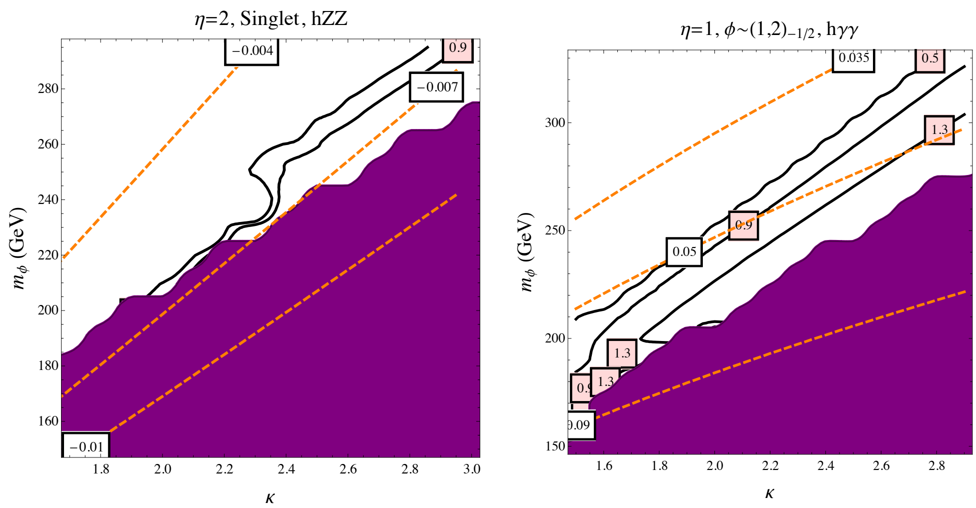

(a) (b)

Figure 32. (a) The fractional deviation of σ_{Zh} at the Higgs factory, in singlet model with Z_2 symmetry [113]. (b) Fractional deviation of the hgg coupling in singlet model with Z_2 symmetry [113]. The new physics particles is a color triplet with electric charge $-1/2$. In both figures, η is the coupling constant of interaction $H^\dagger H \phi^\dagger \phi$.

New physics affecting the nature of the electroweak phase transition will also modify the coupling between the SM-like Higgs boson and other SM states. It is here where the CEPC has the greatest strength. For example, in the general singlet model, the correction to the Higgs-Z coupling, parametrized by κ_Z, is on the order of v^2/M_S^2, for M_S being the typical new physics scale. The projection on the accuracy of measuring this coupling at the CEPC is about 0.25%. Therefore, generically, κ_Z measurement at the CEPC will allow us to probe the singlet as heavy as 5 TeV. At the same time, for first order phase transition, the singlet mass is typically hundreds of GeV. Therefore, the CEPC can completely cover the possible parameter space just by measuring κ_Z in this case. Even in the difficult case of the singlet model with a Z_2 symmetry, the expected deviation of the cross section σ_{Zh} (κ_Z) is about 0.6% (0.5%), as shown in the left panel of Fig. 32. Therefore, the CEPC will see the first evidence of new physics even in this very difficult case. In more general classes of models, the new physics which modifies the Higgs boson coupling can carry other SM gauge quantum numbers, such as electric charge and/or color. In such cases, there will be significant change in the $h \to gg$ and $h \to \gamma\gamma$ couplings. One such example is shown in the right panel of Fig. 32, with 6% deviation in $h\gamma\gamma$ coupling expected. From the projection shown in Fig. 22, we see that the CEPC can have sensitivity to such new physics.

9.2 Naturalness of the electroweak scale

Another important question associated with the electroweak symmetry breaking is naturalness. The discovery of a spin-0 Higgs boson only deepens this mystery. Naturalness arguments lead to the expectation that new physics should be around the TeV scale, and the level of fine-tuning grows $\propto m_{\mathrm{NP}}^2$. It has been a main motivation for postulating the existence of TeV new physics. Such new physics has been a main part of the on going LHC physics program. By definition, any new physics which helps address the naturalness problem must have sizable couplings to the Higgs boson. For example, if the Higgs boson is composite, it is typically implemented as a pseudo-Nambu-Goldstone boson with new dynamics at scale f. In this case, we expect that Higgs boson would not unitarize the WW scattering amplitude completely, and its coupling to W and Z will be shifted by

$$\kappa_W,\ \kappa_Z \simeq \sqrt{1-\frac{v^2}{f^2}}. \tag{9.1}$$

Therefore, the measurement of κ_Z at the CEPC can push f to about 4-5 TeV and gives an interesting test of the idea of naturalness in the composite Higgs models.

Due to the large Higgs boson coupling to the top quark, arguably the most important particle in addressing the naturalness problem is the top partner. For example, in SUSY, the most important new physics particle responsible for the naturalness of the electroweak scale is the scalar top, $\tilde{t}$. The presence of stop will shift both hgg and $h\gamma\gamma$ couplings. The dominant effect is

$$\kappa_g - 1 \simeq \frac{m_t^2}{4m_{\tilde{t}}^2}. \tag{9.2}$$

The measurement of κ_g at the CEPC, up to 1% accuracy, will allow us to probe stop mass up to 900 GeV [118]. This gives another interesting test of the idea of naturalness. We note that, in favorable cases, the search of stop at the LHC run 2 can set a stronger limit on the stop mass. However, this limit depends on the assumption of the mass spectrum of the other superpartners, and the relevant decay modes of the stop. As a result, similar to the result of the stop search at the LHC run 1, there will be significant gaps remaining after the upcoming runs of the LHC, even for light stops. On the other hand, the search of stop by measuring *hgg* coupling is complementary, and completely independent of the decay modes of the stop.

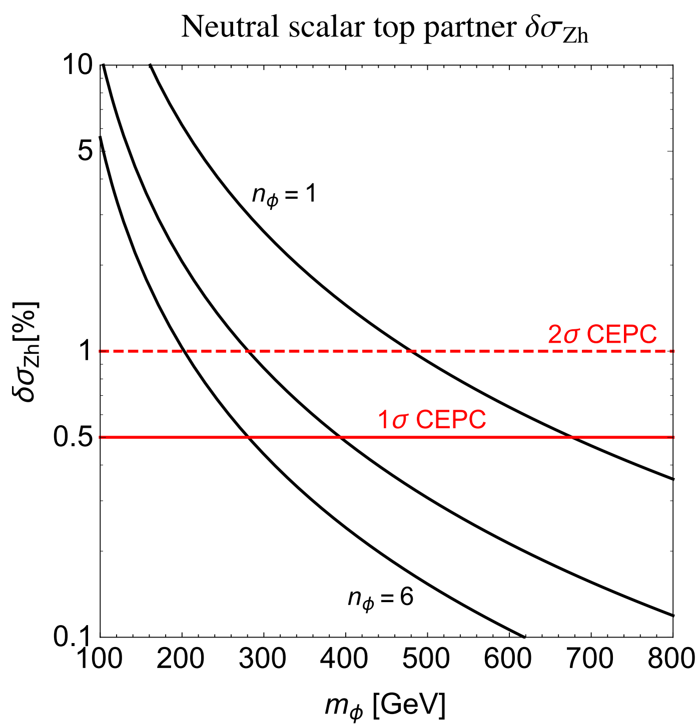

Figure 33. The fractional deviation of σ_{Zh} at the Higgs factory, in the model with scalar singlet top partner, coupling through $H^\dagger H \phi_t^\dagger \phi_t$ [119].

It is also possible that the top partner would not have the same SM gauge quantum numbers as the top quark. In particular, it could be a SM singlet! Such models are quite special. Nevertheless, they represent perhaps the most difficult case in the search of top partners. For example, the only coupling top partner has with the SM fields could be of the form $H^\dagger H \phi_t^\dagger \phi_t$, where ϕ_t is the scalar top partner [119, 120]. This coupling will induce a shift in the Higgs boson coupling to Z at one loop level, which in turn can be probed by the precision measurement of κ_Z at the CEPC. As we can see from Fig. 33, the CEPC will be able to probe the top partner mass up to 800 GeV, giving an non-trivial test of naturalness even in this very difficult scenario.

In general, the newly discovered Higgs particle can also be a new gateway to new physics. One generic form of the Higgs boson coupling to new physics is the so called Higgs portal, $H^\dagger H \mathcal{O}_{\mathrm{NP}}$, where $\mathcal{O}_{\mathrm{NP}}$ is an operator composed out of new physics fields. Since $H^\dagger H$ is the lowest dimensional operator that is consistent with all the symmetries in the Standard Model, it is easy to imagine scenarios in which such Higgs portal couplings are the most relevant ones for the low energy phenomenology of new physics. The singlet extended Higgs sector and the scalar top partner, discussed earlier, are special examples of this coupling.

In general, such couplings will shift the Higgs boson couplings, which can be tested at the CEPC. Moreover, if the new physics is lighter than $m_H/2$, the Higgs portal coupling will lead to new Higgs decay boson channels. The CEPC has excellent capability of probing such decays. For example, it can detect the invisible decay to the level of BR$\sim 0.14\%$. For comparison, HL-LHC can only measure invisible decay branching ratio down to about 6%.

10 Conclusion and Discussion

This is a draft of conclusion.

References

[1] ATLAS Collaboration, *Observation of a new particle in the search for the Standard Model Higgs boson with the ATLAS detector at the LHC*, *Phys. Lett.* **B716** (2012) 1 [arXiv:1207.7214].

[2] CMS Collaboration, *Observation of a new boson at a mass of 125 GeV with the CMS experiment at the LHC*, *Phys. Lett.* **B716** (2012) 30 [arXiv:1207.7235].

[3] ATLAS Collaboration, *Measurements of Higgs boson production and couplings in diboson final states with the ATLAS detector at the LHC*, *Phys. Lett.* **B726** (2013) 88 [arXiv:1307.1427].

[4] ATLAS Collaboration, *Evidence for the spin-0 nature of the Higgs boson using ATLAS data*, *Phys. Lett.* **B726** (2013) 120 [arXiv:1307.1432].

[5] CMS Collaboration, *Observation of a new boson with mass near 125 GeV in pp collisions at $\sqrt{s}$ = 7 and 8 TeV*, *JHEP* **1306** (2013) 081 [arXiv:1303.4571].

[6] CMS Collaboration, *Evidence for the direct decay of the 125 GeV Higgs boson to fermions*, *Nature Phys.* **10** (2014) [arXiv:1401.6527].

[7] CMS Collaboration, *Constraints on the spin-parity and anomalous HVV couplings of the Higgs boson in proton collisions at 7 and 8 TeV*, *Phys. Rev.* **D92** (2015) 012004 [arXiv:1411.3441].

[8] P. Glaysher, *ATLAS Higgs physics prospects at the high luminosity LHC*, vol. EPS-HEP2015, p. 160, Proceedings, 2015 European Physical Society Conference on High Energy Physics (EPS-HEP 2015): Vienna, Austria, July 22-29, 2015.

[9] ILD Concept Group - Linear Collider Collaboration, *The International Large Detector: Letter of Intent*, [arXiv:1006.3396].

[10] T. Behnke, J.E. Brau, P.N. Burrows, J. Fuster, M. Peskin et al., *The International Linear Collider Technical Design Report - Volume 4: Detectors*, [arXiv:1306.6329].

[11] CEPC-SPPC Study Group, *CEPC-SPPC Preliminary Conceptual Design Report. 1. Physics and Detector* (2015), http://cepc.ihep.ac.cn/preCDR/volume.html.

[12] P. Janot, *Particle Flow Event Reconstruction from LEP to LHC*, Presented at Excellence in Detectors and Instrumentation Technologies workshop, CERN (2011), https://indico.cern.ch/event/96989/contribution/15.

[13] M. Minard, *Jet energy measurement with the ALEPH detector at LEP2*, Presented at CALOR2002 Conference, Pasadena, California, USA (2002), http://inspirehep.net/record/608013.

[14] M. Thomson, *Particle Flow Calorimetry and the PandoraPFA Algorithm*, *Nucl. Instrum. Meth.* **A611** (2009) 25 [arXiv:0907.3577].

[15] M. Ruan and H. Videau, *Arbor, a new approach of the Particle Flow Algorithm*, [arXiv:1403.4784].

[16] CMS Collaboration, *Particle-Flow Event Reconstruction in CMS and Performance for Jets, Taus, and MET*, *CMS-PAS-PFT-09-001* (2009), http://cds.cern.ch/record/1194487.

[17] F. Beaudette, *The CMS Particle Flow Algorithm*, p. 295, Proceedings, International Conference on Calorimetry for the High Energy Frontier (CHEF 2013): Paris, France, April

22-25, 2013, arXiv:1401.8155, http://inspirehep.net/record/1279774/files/arXiv:1401.8155.pdf.

[18] P. Mora de Freitas and H. Videau, *Detector simulation with MOKKA / GEANT4: Present and future*, Presented at the International Workshop on physics and experiments with future electron-positron linear colliders, Jeju Island, Korea (2002), http://inspirehep.net/record/609687.

[19] S. Agostinelli et al., *GEANT4: A Simulation toolkit*, *Nucl. Instrum. Meth.* **A506** (2003) 250.

[20] M. Ruan et al., *Reconstruction of physics objects at the Circular Electron Positron Collider with Arbor*, *Eur. Phys. J.* **C78** (2018) 426.

[21] D. Yu, M. Ruan, V. Boudry and H. Videau, *Lepton identification at particle flow oriented detector for the future e^+e^- Higgs factories*, *Eur. Phys. J.* **C77** (2017) 591 [arXiv:1701.07542].

[22] S. Catani, Y.L. Dokshitzer, M. Olsson, G. Turnock and B. Webber, *New clustering algorithm for multi-jet cross-sections in e^+e^- annihilation*, *Phys. Lett.* **B269** (1991) 432.

[23] T. Tanabe and T. Suehara, *LCFIPlus*, Presented at ILD workshop at Kyushu University (2012), https://agenda.linearcollider.org/event/5496/session/1/contribution/16.

[24] LHC Higgs Cross Section Working Group, *Handbook of lhc higgs cross sections: 1. inclusive observables*, [arXiv:1101.0593].

[25] LHC Higgs Cross Section Working Group, *Handbook of lhc higgs cross sections: 2. differential distributions*, [arXiv:1201.3084].

[26] W. Kilian, T. Ohl and J. Reuter, *WHIZARD: Simulating Multi-Particle Processes at LHC and ILC*, *Eur. Phys. J.* **C71** (2011) 1742 [arXiv:0708.4233].

[27] M. Month and S. Turner, *Frontiers of particle beams: observation, diagnosis and correction*, Proceedings, Joint US-CERN School on Particle Accelerators, Capri, Italy (1988), http://link.springer.com/book/10.1007/BFb0018278.

[28] D. Schulte, *Beam-beam simulations with GUINEA-PIG*, Presented at the 5th International Computational Accelerator Physics Conference, Monterey, California, USA, 1998, http://cds.cern.ch/record/382453.

[29] J. Alwall, M. Herquet, F. Maltoni, O. Mattelaer and T. Stelzer, *MadGraph 5 : Going Beyond*, *JHEP* **1106** (2011) 128 [arXiv:1106.0522].

[30] T. Sjostrand, S. Mrenna and P.Z. Skands, *PYTHIA 6.4 Physics and Manual*, *JHEP* **0605** (2006) 026 [hep-ph/0603175].

[31] S. Aplin, J. Engels and F. Gaede, *A production system for massive data processing in ILCSoft*, preprint EUDET-MEMO-2009-12, 2009, http://inspirehep.net/record/889841.

[32] D. Asner, T. Barklow, C. Calancha, K. Fujii, N. Graf et al., *ILC Higgs White Paper*, [arXiv:1310.0763].

[33] H. Baer, T. Barklow, K. Fujii, Y. Gao, A. Hoang et al., *The International Linear Collider Technical Design Report - Volume 2: Physics*, [arXiv:1306.6352].

[34] TLEP Design Study Working Group, *First Look at the Physics Case of TLEP*, *JHEP* **1401** (2014) 164 [arXiv:1308.6176].

[35] Y. Haddad, *Feasibility of a minimum bias analysis of $e^+e^- \to ZH \to q\bar{q} + X$ at a 250 GeV ILC*, [arXiv:1404.3164].

[36] J.F. Gunion, H.E. Haber, G.L. Kane and S. Dawson, *The Higgs Hunter's Guide*, *Front. Phys.* **80** (2000) 1, http://cds.cern.ch/record/425736.

[37] LHC Higgs Cross Section Working Group, *Handbook of LHC Higgs Cross Sections: 3. Higgs Properties*, [arXiv:1307.1347].

[38] X. Chen and Y. Wu, *Search for CP violation effects in the $h \to \tau\tau$ decay with e^+e^- colliders*, *Eur. Phys. J.* **C77** (2017) 697 [arXiv:1703.04855].

[39] ATLAS Collaboration, *Search for the dimuon decay of the Higgs boson in pp collisions at $\sqrt{s}$ = 13 TeV with the ATLAS detector*, *Phys. Rev. Lett.* **119** (2017) 051802 [arXiv:1705.04582].

[40] CMS Collaboration, *Search for a standard model-like Higgs boson in the $^{+}$ and e^+e decay channels at the LHC*, *Phys. Lett.* **B744** (2015) 184 [arXiv:1410.6679].

[41] ALEPH, DELPHI, L3, OPAL, LEP Electroweak Collaboration, *Electroweak Measurements in Electron-Positron Collisions at W-Boson-Pair Energies at LEP*, *Phys. Rept.* **532** (2013) 119 [arXiv:1302.3415].

[42] LHC Higgs Cross Section Working Group, *LHC HXSWG interim recommendations to explore the coupling structure of a Higgs-like particle*, [arXiv:1209.0040].

[43] S. Dawson, A. Gritsan, H. Logan, J. Qian, C. Tully et al., *Working Group Report: Higgs Boson*, [arXiv:1310.8361].

[44] M. Duhrssen, S. Heinemeyer, H. Logan, D. Rainwater, G. Weiglein et al., *Extracting Higgs boson couplings from CERN LHC data*, *Phys. Rev.* **D70** (2004) 113009 [hep-ph/0406323].

[45] B.A. Dobrescu and J.D. Lykken, *Coupling spans of the Higgs-like boson*, *JHEP* **1302** (2013) 073 [arXiv:1210.3342].

[46] CMS Collaboration, *Search for the associated production of the Higgs boson with a top-quark pair*, *JHEP* **1409** (2014) 087 [arXiv:1408.1682].

[47] ATLAS Collaboration, *Search for $H \to \gamma\gamma$ produced in association with top quarks and constraints on the Yukawa coupling between the top quark and the Higgs boson using data taken at 7 TeV and 8 TeV with the ATLAS detector*, *Phys. Lett.* **B740** (2015) 222 [arXiv:1409.3122].

[48] A. Banfi, A. Martin and V. Sanz, *Probing top-partners in Higgs+jets*, *JHEP* **1408** (2014) 053 [arXiv:1308.4771].

[49] A. Azatov and A. Paul, *Probing Higgs couplings with high p_T Higgs production*, *JHEP* **1401** (2014) 014 [arXiv:1309.5273].

[50] C. Grojean, E. Salvioni, M. Schlaffer and A. Weiler, *Very boosted Higgs in gluon fusion*, *JHEP* **1405** (2014) 022 [arXiv:1312.3317].

[51] M. Buschmann, C. Englert, D. Goncalves, T. Plehn and M. Spannowsky, *Resolving the Higgs-Gluon Coupling with Jets*, *Phys. Rev.* **D90** (2014) 013010 [arXiv:1405.7651].

[52] J. Ellis, V. Sanz and T. You, *Complete Higgs Sector Constraints on Dimension-6 Operators*, *JHEP* **1407** (2014) 036 [arXiv:1404.3667].

[53] T. Han, Z. Liu and J. Sayre, *Potential Precision on Higgs Couplings and Total Width at the ILC*, *Phys. Rev.* **D89** (2014) 113006 [arXiv:1311.7155].

[54] M. Klute, R. Lafaye, T. Plehn, M. Rauch and D. Zerwas, *Measuring Higgs Couplings at a Linear Collider*, *Europhys. Lett.* **101** (2013) 51001 [arXiv:1301.1322].

[55] M.E. Peskin, *Estimation of LHC and ILC Capabilities for Precision Higgs Boson Coupling Measurements*, [arXiv:1312.4974].

[56] ATLAS Collaboration, *Projections for measurements of Higgs boson signal strengths and coupling parameters with the ATLAS detector at a HL-LHC, ATL-PHYS-PUB-2014-016* (2014), http://cds.cern.ch/record/1956710.

[57] A. Denner, S. Heinemeyer, I. Puljak, D. Rebuzzi and M. Spira, *Standard Model Higgs-Boson Branching Ratios with Uncertainties*, *Eur. Phys. J.* **C71** (2011) 1753 [arXiv:1107.5909].

[58] L.G. Almeida, S.J. Lee, S. Pokorski and J.D. Wells, *Study of the standard model Higgs boson partial widths and branching fractions*, *Phys. Rev.* **D89** (2014) 033006 [arXiv:1311.6721].

[59] G.P. Lepage, P.B. Mackenzie and M.E. Peskin, *Expected Precision of Higgs Boson Partial Widths within the Standard Model*, [arXiv:1404.0319].

[60] K. Fujii et al., *Physics Case for the 250 GeV Stage of the International Linear Collider*, [arXiv:1710.07621].

[61] M. McCullough, *An Indirect Model-Dependent Probe of the Higgs Self-Coupling*, *Phys. Rev.* **D90** (2014) 015001 [arXiv:1312.3322].

[62] J. Ellis and T. You, *Sensitivities of Prospective Future e+e- Colliders to Decoupled New Physics*, *JHEP* **03** (2016) 089 [arXiv:1510.04561].

[63] J. Ellis, P. Roloff, V. Sanz and T. You, *Dimension-6 Operator Analysis of the CLIC Sensitivity to New Physics*, [arXiv:1701.04804].

[64] G. Durieux, C. Grojean, J. Gu and K. Wang, *The leptonic future of the Higgs*, *JHEP* **09** (2017) 014 [arXiv:1704.02333].

[65] T. Barklow, K. Fujii, S. Jung, R. Karl, J. List, T. Ogawa et al., *Improved Formalism for Precision Higgs Coupling Fits*, [arXiv:1708.08912].

[66] T. Barklow, K. Fujii, S. Jung, M.E. Peskin and J. Tian, *Model-Independent Determination of the Triple Higgs Coupling at* e^+e^- *Colliders*, [arXiv:1708.09079].

[67] S. Di Vita, G. Durieux, C. Grojean, J. Gu, Z. Liu, G. Panico et al., *A global view on the Higgs self-coupling at lepton colliders*, [arXiv:1711.03978].

[68] W.H. Chiu, S.C. Leung, T. Liu, K.F. Lyu and L.T. Wang, *Probing 6D Operators at Future* e^-e^+ *Colliders*, [arXiv:1711.04046].

[69] M. Beneke, D. Boito and Y.M. Wang, *Anomalous Higgs couplings in angular asymmetries of* $H \to Z\ell^+\ell^-$ *and* $e^+e^- \to HZ$, *JHEP* **11** (2014) 028 [arXiv:1406.1361].

[70] N. Craig, J. Gu, Z. Liu and K. Wang, *Beyond Higgs Couplings: Probing the Higgs with Angular Observables at Future* e^+ e^- *Colliders*, *JHEP* **03** (2016) 050 [arXiv:1512.06877].

[71] S.M. Barr and A. Zee, *Electric Dipole Moment of the Electron and of the Neutron*, *Phys. Rev. Lett.* **65** (1990) 21.

[72] J. Fan and M. Reece, *Probing Charged Matter Through Higgs Diphoton Decay, Gamma Ray Lines, and EDMs*, *JHEP* **06** (2013) 004 [arXiv:1301.2597].

[73] ACME Collaboration, J. Baron et al., *Order of Magnitude Smaller Limit on the Electric Dipole Moment of the Electron*, *Science* **343** (2014) 269 [arXiv:1310.7534].

[74] Y.T. Chien, V. Cirigliano, W. Dekens, J. de Vries and E. Mereghetti, *Direct and indirect constraints on CP-violating Higgs-quark and Higgs-gluon interactions*, *JHEP* **02** (2016) 011 [arXiv:1510.00725].

[75] R. Harnik, A. Martin, T. Okui, R. Primulando and F. Yu, *Measuring CP violation in $h \to \tau^+\tau^-$ at colliders*, *Phys. Rev.* **D88** (2013) 076009 [arXiv:1308.1094].

[76] K. Hagiwara, S. Ishihara, R. Szalapski and D. Zeppenfeld, *Low-energy effects of new interactions in the electroweak boson sector*, *Phys. Rev.* **D48** (1993) 2182.

[77] G. Gounaris et al., *Triple gauge boson couplings*, [hep-ph/9601233], http://alice.cern.ch/format/showfull?sysnb=0215385.

[78] L. Bian, J. Shu and Y. Zhang, *Prospects for Triple Gauge Coupling Measurements at Future Lepton Colliders and the 14 TeV LHC*, *JHEP* **09** (2015) 206 [arXiv:1507.02238].

[79] I. Marchesini, *Triple gauge couplings and polarization at the ILC and leakage in a highly granular calorimeter*, *PhD thesis, Hamburg U.* (2011), http://www-library.desy.de/cgi-bin/showprep.pl?thesis11-044.

[80] A. Falkowski, *Higgs Basis: Proposal for an EFT basis choice for LHC HXSWG*, *LHCHXSWG-INT-2015-001* (March, 2015), https://cds.cern.ch/record/2001958.

[81] ATLAS Collaboration, *Projections for measurements of Higgs boson cross sections, branching ratios and coupling parameters with the ATLAS detector at a HL-LHC*, *ATL-PHYS-PUB-2013-014* (2013), https://cds.cern.ch/record/1611186.

[82] ATLAS Collaboration, *HL-LHC projections for signal and background yield measurements of the $H \to \gamma\gamma$ when the Higgs boson is produced in association with t quarks, W or Z bosons*, *ATL-PHYS-PUB-2014-012* (2014), https://cds.cern.ch/record/1741011.

[83] ATLAS Collaboration, *Update of the prospects for the $H \to Z\gamma$ search at the High-Luminosity LHC*, *ATL-PHYS-PUB-2014-006* (2014), https://cds.cern.ch/record/1703276.

[84] ATLAS Collaboration, *Prospects for the study of the Higgs boson in the VH(bb) channel at HL-LHC*, *ATL-PHYS-PUB-2014-011* (2014), https://cds.cern.ch/record/1740962.

[85] ATLAS Collaboration, *Studies of the VBF $H \to \tau_l\tau_{had}$ analysis at High Luminosity LHC conditions*, *ATL-PHYS-PUB-2014-018* (2014), https://cds.cern.ch/record/1956732.

[86] A. Falkowski, M. Gonzalez-Alonso, A. Greljo and D. Marzocca, *Global constraints on anomalous triple gauge couplings in effective field theory approach*, *Phys. Rev. Lett.* **116** (2016) 011801 [arXiv:1508.00581].

[87] A. Butter, O.J.P. Éboli, J. Gonzalez-Fraile, M.C. Gonzalez-Garcia, T. Plehn and M. Rauch, *The Gauge-Higgs Legacy of the LHC Run I*, *JHEP* **07** (2016) 152 [arXiv:1604.03105].

[88] R. Contino, A. Falkowski, F. Goertz, C. Grojean and F. Riva, *On the Validity of the Effective Field Theory Approach to SM Precision Tests*, *JHEP* **07** (2016) 144 [arXiv:1604.06444].

[89] A. Falkowski, M. Gonzalez-Alonso, A. Greljo, D. Marzocca and M. Son, *Anomalous Triple Gauge Couplings in the Effective Field Theory Approach at the LHC*, *JHEP* **02** (2017) 115 [arXiv:1609.06312].

[90] Z. Zhang, *Time to Go Beyond Triple-Gauge-Boson-Coupling Interpretation of W Pair Production*, *Phys. Rev. Lett.* **118** (2017) 011803 [arXiv:1610.01618].

[91] ATLAS Collaboration, *Search for the Standard Model Higgs and Z Boson decays to $J/\psi\,\gamma$: HL-LHC projections*, *ATL-PHYS-PUB-2015-043* (2015), http://cds.cern.ch/record/2054550.

[92] G.T. Bodwin, F. Petriello, S. Stoynev and M. Velasco, *Higgs boson decays to quarkonia and the $H\bar{c}c$ coupling*, *Phys. Rev.* **D88** (2013) 053003 [arXiv:1306.5770].

[93] G. Perez, Y. Soreq, E. Stamou and K. Tobioka, *Constraining the charm Yukawa and Higgs-quark coupling universality*, *Phys. Rev.* **D92** (2015) 033016 [arXiv:1503.00290].

[94] I. Brivio, F. Goertz and G. Isidori, *Probing the Charm Quark Yukawa Coupling in Higgs+Charm Production*, *Phys. Rev. Lett.* **115** (2015) 211801 [arXiv:1507.02916].

[95] F. Bishara, U. Haisch, P.F. Monni and E. Re, *Constraining Light-Quark Yukawa Couplings from Higgs Distributions*, [arXiv:1606.09253].

[96] L.M. Carpenter, T. Han, K. Hendricks, Z. Qian and N. Zhou, *Higgs Boson Decay to Light Jets at the LHC*, *Phys. Rev.* **D95** (2017) 053003 [arXiv:1611.05463].

[97] M. Benedikt, *Future Circular Collider Study Status Overview*, https://indico.cern.ch/event/618254.

[98] A. Falkowski, *Effective field theory approach to LHC Higgs data*, *Pramana* **87** (2016) 39 [arXiv:1505.00046].

[99] A. Falkowski and F. Riva, *Model-independent precision constraints on dimension-6 operators*, *JHEP* **02** (2015) 039 [arXiv:1411.0669].

[100] I. Anderson et al., *Constraining anomalous HVV interactions at proton and lepton colliders*, *Phys. Rev.* **D89** (2014) 035007 [arXiv:1309.4819].

[101] Y. Gao, A.V. Gritsan, Z. Guo, K. Melnikov, M. Schulze and N.V. Tran, *Spin determination of single-produced resonances at hadron colliders*, *Phys. Rev.* **D81** (2010) 075022 [arXiv:1001.3396].

[102] S. Bolognesi, Y. Gao, A.V. Gritsan, K. Melnikov, M. Schulze, N.V. Tran et al., *On the spin and parity of a single-produced resonance at the LHC*, *Phys. Rev.* **D86** (2012) 095031 [arXiv:1208.4018].

[103] CMS Collaboration, *Study of the Mass and Spin-Parity of the Higgs Boson Candidate Via Its Decays to Z Boson Pairs*, *Phys. Rev. Lett.* **110** (2013) 081803 [arXiv:1212.6639].

[104] CMS Collaboration, *Measurement of Higgs boson production and properties in the WW decay channel with leptonic final states*, *JHEP* **01** (2014) 096 [arXiv:1312.1129].

[105] CMS Collaboration, *Measurement of the properties of a Higgs boson in the four-lepton final state*, *Phys. Rev.* **D89** (2014) 092007 [arXiv:1312.5353].

[106] CMS Collaboration, *Combined search for anomalous pseudoscalar HVV couplings in $VH(H \to b\bar{b})$ production and $H \to VV$ decay*, *Phys. Lett.* **B759** (2016) 672 [arXiv:1602.04305].

[107] CMS Collaboration, *Constraints on anomalous Higgs boson couplings using production and decay information in the four-lepton final state*, *Phys. Lett.* **B775** (2017) 1 [arXiv:1707.00541].

[108] D. Stolarski and R. Vega-Morales, *Directly Measuring the Tensor Structure of the Scalar Coupling to Gauge Bosons*, *Phys. Rev.* **D86** (2012) 117504 [arXiv:1208.4840].

[109] J. Ellis, D.S. Hwang, V. Sanz and T. You, *A Fast Track towards the 'Higgs' Spin and Parity*, *JHEP* **11** (2012) 134 [arXiv:1208.6002].

[110] R. Boughezal, T.J. LeCompte and F. Petriello, *Single-variable asymmetries for measuring the 'Higgs' boson spin and CP properties*, [arXiv:1208.4311].

[111] S.Y. Choi, D.J. Miller, M.M. Muhlleitner and P.M. Zerwas, *Identifying the Higgs spin and parity in decays to Z pairs*, *Phys. Lett.* **B553** (2003) 61 [hep-ph/0210077].

[112] S. Profumo, M.J. Ramsey-Musolf, C.L. Wainwright and P. Winslow, *Singlet-catalyzed electroweak phase transitions and precision Higgs boson studies*, *Phys. Rev.* **D91** (2015) 035018 [arXiv:1407.5342].

[113] A. Katz and M. Perelstein, *Higgs Couplings and Electroweak Phase Transition*, *JHEP* **1407** (2014) 108 [arXiv:1401.1827].

[114] A. Noble and M. Perelstein, *Higgs self-coupling as a probe of electroweak phase transition*, *Phys. Rev.* **D78** (2008) 063518 [arXiv:0711.3018].

[115] B. Henning, X. Lu and H. Murayama, *What do precision Higgs measurements buy us?*, [arXiv:1404.1058].

[116] S. Profumo, M.J. Ramsey-Musolf and G. Shaughnessy, *Singlet Higgs phenomenology and the electroweak phase transition*, *JHEP* **0708** (2007) 010 [arXiv:0705.2425].

[117] D. Curtin, P. Meade and C.T. Yu, *Testing Electroweak Baryogenesis with Future Colliders*, *JHEP* **1411** (2014) 127 [arXiv:1409.0005].

[118] J. Fan, M. Reece and L.T. Wang, *Precision Natural SUSY at CEPC, FCC-ee, and ILC*, [arXiv:1412.3107].

[119] N. Craig, C. Englert and M. McCullough, *New Probe of Naturalness*, *Phys. Rev. Lett.* **111** (2013) 121803 [arXiv:1305.5251].

[120] N. Craig, M. Farina, M. McCullough and M. Perelstein, *Precision Higgsstrahlung as a Probe of New Physics*, *JHEP* **1503** (2015) 146 [arXiv:1411.0676].